Structural Analysis of Nickel Doped Cerium Oxide Catalysts for Fuel Reforming in Solid Oxide Fuel Cells

by

Rio Cavendish

A Thesis Presented in Partial Fulfillment
of the Requirements for the Degree
Master of Science

Approved October 2012 by the
Graduate Supervisory Committee:

Peter Crozier, Chair
James Adams
David Smith

ARIZONA STATE UNIVERSITY

December 2012

ABSTRACT

As world energy demands increase, research into more efficient energy production methods has become imperative. Heterogeneous catalysis and nanoscience are used to promote chemical transformations important for energy production. These concepts are important in solid oxide fuel cells (SOFCs) which have attracted attention because of their potential to provide an efficient and environmentally favorable power generation system. The SOFC is also fuel-flexible with the ability to run directly on many fuels other than hydrogen. Internal fuel reforming directly in the anode of the SOFC would greatly reduce the cost and complexity of the device. Methane is the simplest hydrocarbon and a main component in natural gas, making it useful when testing catalysts on the laboratory scale. Nickel (Ni) and gadolinium (Gd) doped ceria (CeO_2) catalysts for potential use in the SOFC anode were synthesized with a spray drying method and tested for catalytic performance using partial oxidation of methane and steam reforming. The relationships between catalytic performance and structure were then investigated using X-ray diffraction, transmission electron microscopy, and environmental transmission electron microscopy. The possibility of solid solutions, segregated phases, and surface layers of Ni were explored. Results for a 10 at.% Ni in CeO_2 catalyst reveal a poor catalytic behavior while a 20 at.% Ni in CeO_2 catalyst is shown to have superior activity. The inclusion of both 10 at.% Gd and 10 at.% Ni in CeO_2 enhances the catalytic performance. Analysis of the presence of Ni in all 3 samples reveals Ni heterogeneity and little evidence for extensive solid solution doping. Ni is found in small domains throughout CeO_2

particles. In the 20 at.% Ni sample a segregated, catalytically active NiO phase is observed. Overall, it is found that significant interaction between Ni and CeO_2 occurs that could affect the synthesis and functionality of the SOFC anode.

ACKNOWLEDGMENTS

I would like to thank my supervisor, Dr. Peter Crozier, for giving me the opportunity to join his research group and begin work in completion of this thesis. I am grateful for the invaluable intellectual guidance provided, the attention he has dedicated in support of this project, and for his assistance with transmission electron microscopy.

I would also like to thank the Crozier research group for their support. I am especially grateful to Liuxian Zhang for his assistance with X-Ray Diffraction. I also owe thanks to my committee members, Dr. James Adams and Dr. David Smith for their time and valuable suggestions.

Finally, I am thankful for the financial support from Arizona State University and to the John M. Cowley Center for High Resolution Microscopy at Arizona State University for use of the TEM facilities.

TABLE OF CONTENTS

Page

CHAPTER Page

LIST OF TABLES

LIST OF FIGURES

Figure Page

Figure Page

Figure Page

Chapter 1

INTRODUCTION

1.1 Background

1.1.1 Catalysis and Nanomaterials

World energy demand is increasing rapidly and current projections estimate that between 2007 and 2035 this demand will increase by 50% [1]. With a greater demand, problems faced include the decreasing supply of fossil fuels as well as pollution and global warming due to greenhouse gas emissions. With this forecast it is necessary to invest in alternate energy forms that are clean and more efficient, and to explore sustainable energy conversion processes. When utilizing or synthesizing fuels it is very important that processes are carried out with high efficiency to maximize their energy output. In the area of chemical transformations, catalysts are essential because they accelerate processes and allow them to be carried out at favorable temperatures and pressures. Approximately 85–90% of the products formed in the chemical industry utilize catalysis [2]. Catalysts are used in production of transportation fuels, chemicals, and in pollution abatement. A catalyst accelerates a chemical reaction by offering an alternative reaction path with lower activation energy. The catalyst forms bonds with the reactant molecules, where they react to form a product, and detach from the catalyst. The catalyst is left unaltered to facilitate more reactions. In heterogeneous catalysis, the catalyst phase is distinct from the phase of the reaction. Most often, solids catalyze reactions of molecules in gas or solution. For solid catalysts, reactions occur on the surface of the material and how the catalyst

interacts with gas molecules through adsorption, dissociation, and desorption determine how effective it is for a particular reaction. The catalyst must also have stability, low cost, and a high surface area to maximize contact with reactants. This is often achieved through the use of nanomaterials because they possess a very high surface area to volume ratio. Nanometer-sized particles are often dispersed on a support [2]. Physical and chemical properties of nanomaterials differ from those of molecular or bulk materials with the same composition [3]. Properties such as structure and shape, phase changes, electronic behavior, chemical reactivity, and catalytic properties can all be altered as size decreases to the nano level.

1.1.2 Solid Oxide Fuel Cells

The concepts of catalysis and nanotechnology can be applied to energy in the area of fuel cells. Fuel cells are electrochemical devices that convert the chemical energy in fuels into electrical energy through the reaction between oxygen and hydrogen. There are several types of fuel cells, designated by the working principle and materials in the electrolyte [4]. One of the most promising types of fuel cell is the solid oxide fuel cell (SOFC) which operates at high temperature. SOFC's have many important advantages and the potential to provide an efficient, environmentally favorable, fuel-flexible power generation system. The SOFC can utilize a variety of fuels including hydrogen and methane, as well as commonly used fuels such as gasoline or natural gas [5]. The SOFC consists of a dense ceramic electrolyte layer housed in between two porous

electrodes. Air flows along the cathode where oxygen molecules are split into oxygen ions. This process occurs at an area known as the triple-phase boundary (TPB), the boundary between the cathode, electrolyte, and air. The dense electrolyte is impervious to gas and separates gaseous redox reactions of the two electrodes. The oxygen ions formed at the TPB, however, are able to diffuse through the electrolyte to the anode. At the TPB of the anode, oxygen ions react catalytically with hydrogen, combining to create water and releasing electrons. The electrons are directed through the anode to an external circuit which provides electrical energy [6]. Multiple cells can be layered to achieve the desired power output through use of an interconnect which is the electrical connection between the cells. A diagram of the entire SOFC is shown in Figure 1.1. Currently, the SOFC component materials are yttria stabilized zirconia (YSZ) as the electrolyte, Sr-substituted $LaMnO_3$ (LSM) for the cathode, and nickel-YSZ ceramic metal composite (cermet) as the anode.

While the SOFC operating principle has proven to be effective, there are many materials issues hindering its mainstream production and commercialization. With current materials, SOFCs operate at high temperatures ranging from 800°C -1000°C. Operation at high temperature is necessary to promote ionic conductivity and the kinetics of oxygen ion transport. However, high temperature requirements introduce materials degradation issues and economic obstacles. Issues such as chemical reactions between the electrolyte and electrodes, cracking due to stresses created by mismatched thermal properties, and sintering of anode nickel particles are all issues limiting commercialization [5]. At

high operating temperatures, another problem is that metals and alloys cannot be used in interconnects and thus, the material of choice has traditionally been a more costly ceramic. Many longstanding issues could be solved if the SOFC was made to operate at an intermediate temperature of 500°C - 750°C [7]. Alternate electrolyte materials with higher ionic conductivity at lower temperatures are being explored for this reason.

1.1.3 Fuel Reforming and the SOFC anode

The main function of the SOFC anode is to provide reaction sites for the electrochemical oxidation of fuel. This reaction only occurs at the TPB, the interface between the electrolyte, the metal phase, and the gas, as shown in Figure 1.2. The anode needs to have a significant amount of porosity to allow fuel and products to be delivered and removed from the reaction sites. The anode must also have conducting pathways in order to transfer electrons resulting from the reaction into an external circuit. The necessity of these three phases interacting simultaneously places strict requirements on the material structure. Cermets are used in the anode to prevent sintering and increase compatibility with the electrolyte [5].

Fuel reforming is a method of producing hydrogen from fuels to run the fuel cell reaction. One of the most important advantages of the SOFC is its fuel flexibility which arises from the fact that O^{2-} ions are the mobile species in the electrolyte [8]. The fuel that will produce the quickest reaction within the anode is hydrogen, but the SOFC is unique in that other fuels can also react directly on the

anode. It is desirable to use fuels other than H_2 directly in the fuel cell because they are less expensive, more easily stored, and more readily available than hydrogen. Most hydrogen is currently produced by the reforming of hydrocarbons, and the electricity would be more efficiently produced from the hydrocarbons directly [9]. If hydrogen is produced externally and then fed into the SOFC the process is known as external fuel reforming. Alternatively, with internal fuel reforming, the fuel itself can be fed directly into the fuel cell stack. With internal fuel reforming, an indirect method can be used where a separate catalyst attached to the SOFC facilitates fuel reformation, or, the process can take place directly on the anode of the SOFC with no separate component [5]. External reforming of hydrocarbon fuel requires extra reforming equipment which impacts the cost and efficiency of the device and indirect internal reforming requires an extra component be added to the SOFC stack. Therefore, in order to maintain system efficiency and simplicity, and to reduce cost of the device itself, it is favorable to develop SOFC anodes capable of direct fuel utilization. In order to accomplish this, fuels must be rapidly dissociated from long hydrocarbon chains into hydrogen over the anode. The biggest problem with current Ni/YSZ anodes in the susceptibility of Ni to carbon build-up which eventually deactivates the device [9]. With direct reforming, the anode must be able to fill multiple roles. It must first act as a hydrocarbon reforming catalyst, converting hydrocarbons to hydrogen. It must also continue to perform within the SOFC, acting as an electrocatalyst for the oxidation of fuels in the anode and as an electronic and

ionic conductor [5]. This places considerable materials selection requirements on the anode.

1.1.4 Fuel Reforming Reactions

There are several reactions that can be used for internal fuel reforming. These include steam reforming, dry (CO_2) reforming, partial oxidation reforming, and autothermal reforming [5]. Because CH_4 is the simplest hydrocarbon, reforming reactions are often written in terms of CH_4 to express the enthalpy of reaction and products formed. Steam reforming (SR) is the reaction currently used for external reforming in the SOFC, and for the production of H_2. It efficiently produces synthesis gas (H_2+CO) with a very high ratio of H_2 to CO and easily reaches the thermodynamic limit. Steam reforming consists of several reactions. Reaction 1.1 is the steam reforming reaction generalized for all hydrocarbon fuels [10] and reaction 1.2 is the steam reforming of methane reaction including the ΔH value indicating the reaction is endothermic. Reaction 1.1 can be followed by the exothermic water gas-shift reaction (1.3) which produces extra H_2 along with CO_2. There is also a second steam reforming reaction (1.4) that can occur resulting in the production of CO_2 rather than CO [11].

$$C_nH_{2n+2} + nH_2O \rightarrow nCO + (2n+1)H_2 \quad (1.1)$$

$$CH_4 + H_2O \rightarrow CO + 3H_2 \qquad \Delta H = +206\ kJ/mol \quad (1.2)$$

$$CO + H_2O \rightarrow CO_2 + H_2 \qquad \Delta H = -41\ kJ/mol \quad (1.3)$$

$$CH_4 + 2H_2O \rightarrow CO_2 + 4H_2 \qquad \Delta H = +165\ kJ/mol \quad (1.4)$$

Steam reforming is endothermic and favors high temperatures and low gas pressures. The endothermic nature is beneficial for fuel reforming because there are lesser cooling requirements. This also means an external heat source is required for device start-up to promote the reaction. Once the reaction has started, waste heat from the fuel cell could be recirculated to promote the reaction [5].

Deactivation of anode materials from carbon deposition can occur through several reactions that are catalyzed by the same catalysts for steam reforming. The first is hydrocarbon pyrolysis, which is thermal cracking of hydrocarbons, shown in the general form in equation 1.5 and for methane in 1.6. The second reaction shown in equation (7) is the Boudouard reaction [12].

$$C_nH_{2n+2} \rightarrow nC + (n+1)H_2 \quad (1.5)$$

$$CH_4 \rightarrow C + 2H_2 \qquad \Delta H = 75\ kJ/mol \quad (1.6)$$

$$2CO \rightarrow C + CO_2 \qquad \Delta H = -172\ kJ/mol \quad (1.7)$$

For steam reforming this problem is remedied by using steam to carbon ratios of 3 to 1 to minimize carbon formation. The excess steam improves CH_4 conversion and promotes the water-gas shift reaction but it also costs more energy to produce steam [11].

Carbon dioxide or dry reforming is similar to steam reforming in thermodynamic characteristics but produces product with a lower H_2 to CO ratio than steam reforming. Carbon formation during CO_2 reforming is more severe because of this lower ratio [13]. The generalized reaction for all hydrocarbons is shown in equation 1.8 and the equation for methane is shown in 1.9. The reaction

is highly endothermic like SR and can be followed by the reverse water gas shift reaction (1.10).

$$C_nH_{2n+2} + nCO_2 \rightarrow 2nCO + (n+1)H_2 \quad (1.8)$$

$$CH_4 + CO_2 \rightarrow 2CO + 2H_2 \qquad \Delta H = +247\ kJ/mol \quad (1.9)$$

$$CO_2 + H_2 \rightarrow CO + H_2O \qquad \Delta H = +41 kJ/mol \quad (1.10)$$

One advantage of dry reforming over steam reforming is that CO_2 is easier to work with than steam. CO_2 reforming could also be useful for utilizing greenhouse gases and for processing CO_2 from natural gas deposits and biomass sources [13].

Partial oxidation (POX) reforming is an exothermic reaction that combines a hydrocarbon fuel with oxygen to partially oxidize the fuel into synthesis gas. Two reactions can occur, the partial oxidation reaction and the complete combustion reaction. The complete combustion reaction is highly exothermic while the partial oxidation reaction is mildly exothermic [14]. The general reaction [8] is shown in equation 1.11, the partial oxidation of methane (POM) reaction is shown in 1.12, and the complete combustion of methane is shown in 1.13.

$$C_nH_{2n+2} + n/2\ O_2 \rightarrow nCO + (n+1)H_2 \quad (1.11)$$

$$CH_4 + \tfrac{1}{2}\ O_2 \rightarrow CO + 2H_2 \qquad \Delta H = -36\ kJ/mol \quad (1.12)$$

$$CH_4 + 2O_2 \rightarrow CO_2 + 2H_2O \qquad \Delta H = -803\ kJ/mol \quad (1.13)$$

Benefits of partial oxidation are that it is cheaper than steam reforming because it does not require heated steam, and it has the possibility of using air as oxidant. The reaction is exothermic so in a fuel cell this means a quicker start-up is

possible, but some fuel energy is lost to heat so the conversion is less efficient [15]. Unlike SR and CO_2 reforming, it also has selectivity issues where the competition is between complete and partial oxidation which form different products. When utilizing the POX reaction within the SOFC anode, maintaining power output is important and the anode must be selective for partial oxidation rather than complete oxidation.

Carbon deposition is also an issue for partial oxidation through reactions 1.8, 1.9, and 1.10 as for steam reforming. Excess O_2 can be used to prevent C deposition but this also leads to complete combustion [16]. Partial oxidation is mostly considered as being suitable for small scale applications that require system efficiency and quick startup.

Autothermal reforming is a combination of steam reforming and partial oxidation. There are two methods of combining the reactions. POX can be used at startup and then steam reforming can be used afterwards when the operating temperature is reached. This is beneficial because POX is exothermic so less external heat is needed for startup. Once POX causes the fuel cell reaction to produce steam, it can be recirculated through the fuel cell to begin steam reforming [5]. Autothermal reforming can also be carried out by combining fuel with air and steam. Benefits of this are the same as the first case where no external heat and no external steam are needed after startup. The addition of oxygen also lowers the needed reaction temperature which prevents carbon deposition and increases selectivity to H_2 through the WGS reaction [16]. For autothermal reforming the maximum theoretical hydrogen yield will occur when

all of the C in fuels is converted to CO_2 rather than CO [17]. One group's version of the general, idealized reaction is shown in equation 1.14 where results are dependent on the ratios of steam to oxygen used [18]. In this equation, x is derived from the molar ratio of O_2 to fuel ($O_2/C = x/n$), y is from the molar ratio of H_2O to fuel ($H_2O/C = y/n$), and (y-2x-2n) is the excess water. The heat of reaction ΔH can be endothermic or exothermic depending on the contributions from POX and SR. Theoretically, the maximum efficiency for fuel reforming will occur when $\Delta H=0$ [18]

$$C_nH_m + xO_2 + yH_2O \rightarrow nCO_2 + (2n-2x+m/2)H_2 + (y+2x-2n)H_2O \qquad (1.14)$$

Autothermal reforming provides a simpler design than steam reforming and a higher efficiency than POX since less fuel energy will be lost to heat. Autothermal reforming describes a thermally self regulating process where we do not need to supply energy and thus provides a greater efficiency. Disadvantages are that hot spots due to differences in reaction rates can occur in a fuel cell. Another issue is that the idealized chemistry will not necessarily be attained due to the coexistence of other chemical reactions including the reverse water-gas shift reaction, methanation (reverse of steam reforming), and incomplete conversions [18]. Several studies have shown an optimum O_2 to C ratio exists where maximum conversions are reached. This is because oxygen assists in reforming hydrocarbons, but at too high concentrations it will begin to oxidize hydrogen [19].

1.1.5 Fuel Choice

The choice of fuel is also an important parameter that will impact the effectiveness of fuel reforming. Fuel choice is dictated by the application (stationary vs. mobile), operating temperature, availability, cost, catalyst, and reaction [5]. Methane (CH_4) is the simplest hydrocarbon and the main component of natural gas. CH_4 has a higher stability and generates less heat so it is thus less reactive than higher hydrocarbons and is reformed poorly at lower temperatures [20]. Ethane (C_2H_6) is the second simplest hydrocarbon and the second largest component of natural gas so it is also of interest when testing fuel cell catalysts. Natural gas is a promising fuel because it is abundant, has a low cost, and has existing infrastructure in place. It is composed of methane plus higher hydrocarbons, the amount of which decrease logarithmically with increasing carbon content [5]. Natural gas as a fuel is most suitable for stationary applications. The main issues are deactivation from carbon deposition and odorant sulfur.

Another potential gas for use in the SOFC is biogas which is waste gas from farm, municipal, industrial, and landfill sources. The composition is highly variable but is most often methane (40–65%), and carbon dioxide (30–40%). The source is currently too small and varied to be the main fuel for SOFC, but could be used on smaller scales to reform waste gases. Dry-reforming (CO_2) or autothermal reforming with the addition of steam or air could be used for conversion [21]. Liquefied petroleum gas such as propane (C_3H_8) and butane (C_4H_{10}) which are byproducts of refining petroleum can also be considered. These

fuels contain more carbon and will thus provide more C deposition than natural gas. They are however being considered for small-scale applications such as portable generators and for locations where there is no existing natural gas supply. The advantage is they are readily available, inexpensive, have a high H to C ratio, and are the lowest molecular weight hydrocarbons that can be used in liquid form [9].

Liquid fuels are of interest for use in fuel cells, especially for portable small-scale applications. The main issue with liquid fuels is their propensity for carbon formation due to the higher amount of carbon present in longer chains hydrocarbons. Alcohols have not been highly explored for direct utilization but are gaining much interest because they have the potential for low temperature operation and can be reformed at 300-600°C [15]. They also contain more oxygen which leads to less carbon deposition and are a more alternative, renewable, and environmental-friendly fuel than hydrocarbons. Methanol (CH_3OH) is the simplest alcohol and is produced from natural gas and biomass. Since it is a liquid fuel it has a high energy density and is easily stored and transported. It has fewer impurities as compared to hydrocarbons that will poison the anode but it is toxic and there are concerns of groundwater contamination in case of spills. Ethanol (C_2H_5OH) is produced from ethylene hydration or fermentation and offers similar advantages to the use of methanol. A promising area of interest is in ethanol biofuels derived from corn or sugarcane. Ethanol is harder to oxidize than hydrogen and methanol and reforming can be more problematic than for natural gas or methanol because of issues with carbon deposition [15].

Other liquid fuels of interest are gasoline, diesel, kerosene, and jet fuel (JP-8). These options are mostly considered for portable fuel cells because they are easily transportable, widely available, and have a high energy density. They contain many different hydrocarbons, various aromatics and alkanes, and have a low H to C ratio which means that carbon formation will be more thermodynamically favorable [15]. Larger hydrocarbons are still beneficial in that they have lower C-C bond energies and are broken apart more easily so they can be reformed at lower temperatures. The stability of the hydrocarbons is what affects reforming potential the most with alkane chains being the most reactive and poly-aromatics being the least reactive [22]. Many difficulties arise when using conventional fuels for SOFC in that they have additives such as surfactants and lubricants and can contain up to 100 different molecules [5]. Often for research in fuel cells, "surrogate" fuels of the most prominent components are used to represent the fuel. For example, gasoline is often represented by n-octane (C_8H_{18}) and diesel is simulated as dodecane ($C_{12}H_{26}$) and hexadecane ($C_{16}H_{34}$) [22]. The difficulties associated with hydrocarbon fuels allow for pioneering research into fuels that could support both engines and fuel cells, and into carbon resistant anodes.

1.1.6 Carbon Formation on Nickel

The reactions for carbon formation were described earlier in section 1.1.4. As the number of carbon atoms in a fuel increase, deactivation from carbon formation increases drastically with deactivation being the worst for fuels with

four or more C atoms [10]. Currently methane can be reformed internally with Ni/YSZ but excess amounts of steam are needed to prevent coking with higher hydrocarbons. Carbon formation on Ni is initiated by reactions (1.6) and (1.7) where carbon forms and adsorbs on the Ni metal. There are 3 types of carbon that have been identified that form on the surface: pyrolytic carbon, encapsulating carbon, and whisker carbon [23]. One method of deactivation is when encapsulating carbon completely covers the surface of Ni, preventing it from reacting. The other deactivation process involves interaction between Ni and C. Carbon that deposits on the surface but is not removed through gas phase reaction can be dissolved into the bulk Ni metal. When it precipitates back onto the surface it causes stress in the anode from volume changes which can lead to failure and fracture [9]. Carbon must be removed quickly from the surface before it is dissolved to prevent this. Higher hydrocarbons often form C more quickly than it can be removed. Carbon formation rate and deactivation are far worse on Ni than for noble metals. This is because noble metals do not dissolve carbon to the degree Ni does [12].

For heterogeneous catalysts small amounts of nano-sized metal particles are dispersed over a high surface area support [24]. The major difference between heterogeneous catalysis and SOFC anodes is the requirement that in the SOFC anode the gas phase, the electronic conductor phase, and the ionic conductor phase, must all come together at the site where reactions occur. This requirement adds an additional level of complexity not found in normal catalysts and much larger amounts of metal are used because a metal pathway is needed for

conduction of electrons through the anode [5]. The higher amount of metal needed means that use of Ni can be a problem as it leads to more C deposition and sintering of particles. Different anode structures and compositions are being explored to solve these issues.

1.2 Motivation

1.2.1 Materials Choices

Though nickel has issues with carbon formation there are still many properties that have made it a prominent catalyst for steam reforming, partial oxidation, and for use in fuel cell anodes. While noble metals like platinum have excellent catalytic properties, they are too expensive to be feasible for large scale applications [25]. Nickel is inexpensive and exhibits high catalytic activity which means internal reforming and direct operation with fuels could be possible. Much of SOFC research is currently focused on modifying and optimizing Ni-based anodes to prevent C deposition during direct hydrocarbon operation [5]. Another area of considerable interest is in cerium oxide (ceria, CeO_2) based materials for use in intermediate temperature solid oxide fuel cells. Cerium oxide based materials exhibit higher ionic conductivity at lower temperatures than YSZ and are of interest for use in the SOFC electrolyte [26]. Pure CeO_2 alone is not a good oxygen ion conductor, but the conductivity can be increased through doping which introduces oxygen vacancies. Two of the most common choices of dopants in ceria are gadolinium (Gd) and samarium (Sm). Gd^{3+} is a promising dopant cation for ceria because it has low ion mismatch with the host Ce^{4+} cations. The

closer the radii of the host and dopant cations, the fewer stresses caused by lattice mismatch that inhibit diffusion [27].

Ceria has a fluorite structure composed of Ce cations occupying the face-centered cubic unit cell positions, and oxygen anions in the tetrahedral holes of the structure, shown in Figure 1.3. CeO_2 is a reducible oxide that behaves according to oxygen partial pressure in the environment. At room temperature ceria will take the form CeO_2. Under reducing conditions and elevated temperatures, however, as prevalent on the anode side of a SOFC, it has been observed that Ce^{4+} ions are reduced to Ce^{3+} ions [28]. This reduction creates oxygen vacancies and n-type defects according to the equation:

$$O_O^x \rightarrow V_O^{\cdot\cdot} + \frac{1}{2}\, O_2\,(g) + 2e' \qquad (1.15)$$

where O_O^x is oxygen in the CeO_2 lattice, $V_O^{\cdot\cdot}$ is an oxygen vacancy with a charge of 2+, and e' is an electron. Electrons created on reduction can hop between adjacent Ce^{4+} and Ce^{3+} ions which causes electronic conductivity. This gives rise to what is known as mixed ionic electronic conductivity (MIEC) [29]. An anode composed of a MIEC would be beneficial for the SOFC because it would extend reaction sites over the entire anode rather than just the TPB. In order for a MIEC anode to be effective it must have a high ionic conductivity, high electronic conductivity and compatibility with the electrolyte, as well as high catalytic activity. Ceria based materials meet many of these requirements but the properties are highly dependent on whether the material is doped with lower valent cations, what the dopant is, and the dopant amount. Dopants will increase ionic conductivity but decrease electronic conductivity due to the formation of

oxygen vacancies. Thus, doped CeO_2 materials do not exhibit high enough activity to function as an anode without an extra electronically conducting phase [30]. However, MIEC can still enhance the anode performance by promoting charge-transfer reactions at the TPB. Doping CeO_2 is also known to decrease the expansion and contraction during reduction and oxidation significantly and prevent anode deactivation from stress.

In addition to the electronic properties of CeO_2, it may also contribute catalytically. Ceria has been shown to work as an oxidation catalyst with methane, propane, and butane [19]. With no oxidant present, lattice oxygen and adsorbed C from fuels are used to create CO and H_2 based on the equation

$$CH_4 + O_O^x \rightarrow 2H_2 + CO + V_O^{\cdot\cdot} + 2e' \quad (1.15)$$

The reaction is thermodynamically favored at temperatures greater than 600 °C. With no oxidant present, in CH_4, ceria reduction reaches 21% where complete reduction to the structure of Ce_2O_3 corresponds to a reduction of 25% [31]. The lattice oxygen can be regenerated by including steam or air with the reaction. It was found that gadolinium doped ceria (GDC) in CH_4 was resistant to carbon deposition but showed low activity for methane oxidation. Thus, for use in an anode, ceria alone would need an additional catalyst for breaking C-H bonds of higher hydrocarbons [32].

When combining Ni and CeO_2, Ni is needed as the cracking catalyst and main electron conductor. Ceria acts as the ionic conductor and oxidation catalyst for CO and adsorbed carbon. It has been shown that the properties of ceria can affect the structural and electronic properties of metal catalysts. Possible benefits

include reduction of carbon deposition on Ni as well as inhibition of Ni particle sintering [33]. Ni and ceria exhibit what is known as a strong metal support interaction (SMSI). One manifestation of this is "decoration" by ceria, witnessed during reduction at 600°C –700°C, where the metal catalyst is covered with a layer of ceria [34]. It has also been observed that the Ni metal can spread over the surface of ceria during reduction at 750°C [35]. The effects of this interaction may enhance the properties of the Ni catalyst and prevent deactivation. One study showed that a Ni – GDC catalyst displayed self-decoking during reaction with methane and no oxidant present. Carbon deposited from CH_4 reacted with lattice oxygen to form CO and CO_2, and the amount of product formed was dependant on the amount of lattice oxygen provided [36].

1.2.2 Doping ceria with Ni

Ceria acts as a support for active metals, exhibiting considerable SMSI, but metals can also dope in the fluorite lattice and form solid solutions. The distinction between ceria supported metal or metal doped into the lattice is often unclear because solid solutions, phase segregation, and surface enrichment are possible which can lead to similar structures and complicate characterization [34].

There are several reports of doping ceria with Ni in literature [37, 38, 39, 40]. Several groups have reported that the solubility of Ni into CeO_2 is 10 at.% [37, 38]. The first group [37, 41] reported 10 at.% solubility and found that at 20 at.% Ni, a distinct NiO phase was formed. They described how the addition of Ni in the lattice induces strain, creating oxygen vacancies which increase catalyst

activity. The 20 at.% Ni catalyst was found to be highly active for steam reforming of ethanol and for the water gas shift reaction.

The second group [38] reporting 10% solubility tested several Ni doped catalysts for propane autothermal reforming. It was similarly found that a NiO phase appeared at 20 at.% Ni and it was concluded that Ni solubility in CeO_2 is 10 at.%. A 5 at.% Ni sample was tested and found to be stable for 100 hours at 650°C in propane.

Several studies by another group [39,42,43] found synthesis method to be most important in whether a solid solution was formed. Ni was added to CeO_2 with Ni/Ce ratios between 0.2 and 1. They found that Ni doping into CeO_2 was highest when the Ni/Ce ratio was 0.5. The solid solution then decreased with increasing Ni content in favor of a separate NiO phase.

A fourth group tested Ni doped CeO_2 concentrations from 5-60 at.% Ni [40]. They found the presence of 3 types of Ni: highly dispersed NiO, aggregated NiO, and solid solutions. The formation of these different types of Ni was also highly dependent on synthesis. Similar to other results, the NiO phase appeared in XRD at 20 at.% Ni. Catalysts were tested with POM and it was found that 40 at.% Ni was the best catalyst and that 20 at.% Ni was stable at 650°C for 160 hours.

There have also been reports in literature of no solubility of Ni in CeO_2. One of the earliest reports [44] of 10 at.% Ni solubility in CeO_2 and was refuted [45] with the argument that it is not possible to dope Ni into CeO_2 because Ni is unstable in 8-fold coordination. The small size of the Ni ion as compared to Ce will give a larger elastic energy due to ion mismatch size meaning a lower

solubility, and the calculations for Ni find that doping is improbable. The response to this criticism was that the calculations assumed a linear relationship between doping and solubility which had not been proven for metals like Ni, and that oxygen partial pressure could affect valence of both Ni and Ce and thus coordination [46].

Following this, another group calculated a possible phase diagram for Ce-Ni-O assuming no solid solubility of Ni into CeO_2 and compared it to experimental work [47]. It was reported that no interaction occurred after CeO_2 and NiO were mixed together and calcined at both 1200°C and 1600°C. Other work [48] also tried to bridge the gap in literature by investigating solubility of Ni into GDC. They added GDC and NiO together and calcined at 1200°C and 1300°C. Samples were also reduced in H_2 at 800°C and 1000°C and analyzed. No doping of Ni into GDC was found.

The main difference between those studies reporting solubility and those reporting none is the synthesis method. Those reporting no solubility of Ni into CeO_2 mixed NiO and cerium oxides together and heat treated at high temperatures. Those reporting doping used other methods like combustion and microemulsion that mix together precursors and process them simultaneously. The equilibrium method of mixing the two oxides together and heat treating at high temperatures has shown no solid solution, so it is possible the discrepancies are due to processing methods. The reported Ni doping could be from metastable solid solutions, not true, equilibrium solutions that would not decay to their separate phases with time [49].

1.2.3 Project Goals

Because doping of Ni into CeO_2 seems to rely so heavily on synthesis technique, we chose to use a spray drying method where nitrate precursors are processed together. The system synthesizes nanopowders and has been used to create homogeneous mixtures of doped ceria such as GDC [50]. The issue we want to investigate most is catalytic performance of a Ni doped CeO_2 catalyst for fuel reforming in the SOFC anode. Because it is the lowest hydrocarbon and main component of natural gas we chose to run tests with methane. We have only explored CH_4, but it is desirable to use higher hydrocarbons to explore deactivation from carbon.

We chose to investigate catalytic properties of the starting nanopowders that would be used to make a SOFC anode. The goal was to prepare Ni doped CeO_2 catalysts and characterize the catalytic properties as related to the structure of nickel and ceria, which will each contribute their own individual properties. Understanding the material at the nanoscale can give new insight into the mechanism of catalysis and how the material can be manipulated to more effectively process fuels. Transmission electron microscopy (TEM) was used to investigate structural properties in attempt to understand the potential doping of Ni into CeO_2.

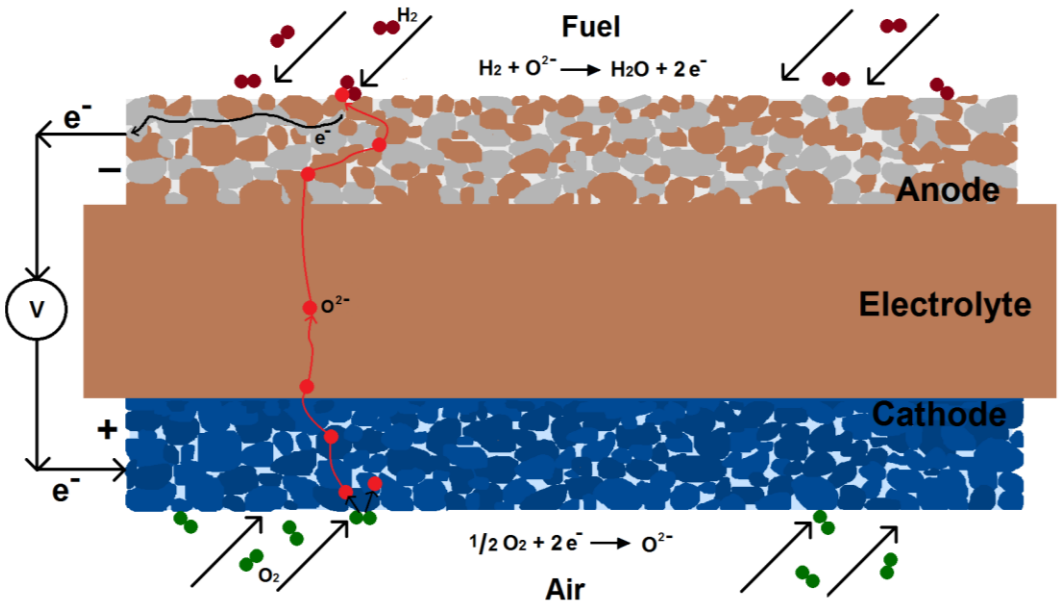

Figure 1.1: SOFC schematic showing reactions taking place in one cell.

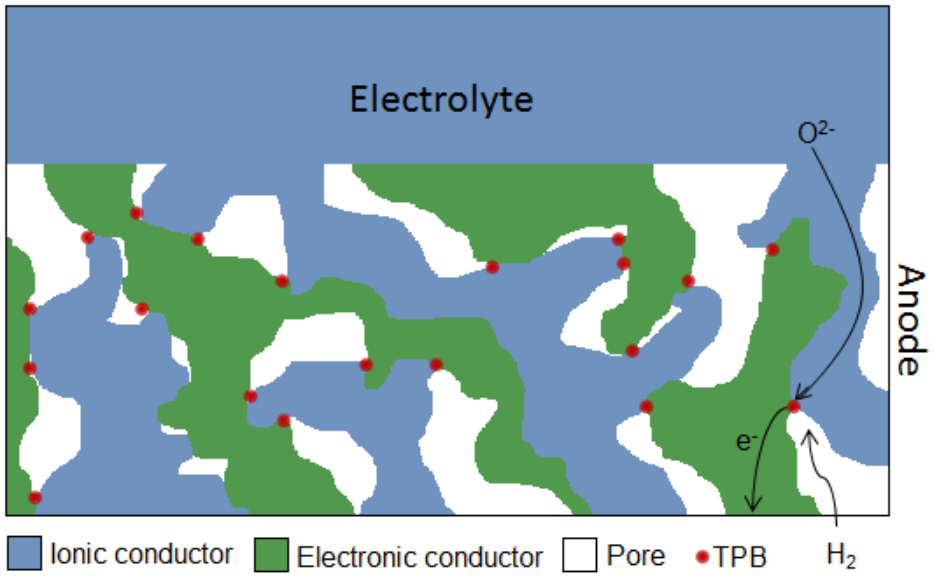

Figure 1.2: Illustration of triple phase boundary (TPB) of the SOFC anode.

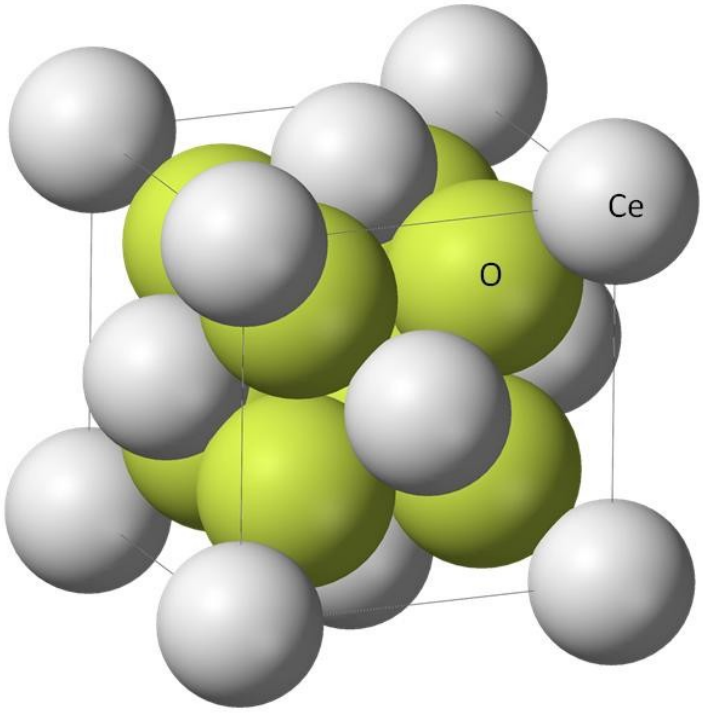

Figure 1.3: Fluorite structure of cerium oxide with Ce ions occupying FCC positions and O ions occupying tetrahedral holes [51].

Chapter 2

INSTRUMENTATION AND METHODS

2.1 Catalytic Experiments

2.1.1 Reactor Setup and Principles

Measurements of catalytic properties were performed in an In-Situ Research Instruments (ISRI) RIG 150 reactor (Figure 2.1a). This is a micro reactor system with computer controlled gas flow and temperature program capabilities. The reactor contains four gas input lines connected to mass flow controllers, allowing flow rates to be calibrated depending on the gases used. The system is also equipped with a high temperature furnace that operates up to 900°C and a quartz reactor tube containing a thermocouple well for temperature measurements in the proximity of the catalyst. With this setup, gas flows from compressed gas cylinders into the reactor tube where it interacts with the sample at elevated temperatures. After interaction with the sample, the gases are directed to a gas chromatograph for analysis. A diagram of the system is shown in Figure 2.1b.

2.1.2 Gas Chromatography

Gas samples during catalytic reactions are periodically analyzed using gas chromatography. Gas chromatography is a method of separation and analysis of the components of a gas sample. Samples are injected into columns containing a material coating the walls on which gases will strongly adsorb. An inert carrier

gas is used to carry the sample through the column at a controlled flow rate. The gas mixture interacts with the column walls through adsorption and each gas will elute, or exit the column, at a different time [52]. The gases exit the columns into a detector and retention time is used to identify them. The detector used is a thermal conductivity detector (TCD) that detects gases based on their thermal conductivity as compared to that of the carrier gas, helium. Thermal conductivity is a measure of a materials ability to conduct heat. The TCD detector is composed of a Wheatstone bridge circuit that measures resistance changes in a filament as the gas samples pass over it. Within the detector there are two heated filaments, one which the effluent gas from the column passes over and one which the carrier gas passes over as a reference. A constant current is supplied to the circuit and differences are monitored between the two sides, with temperature differences leading to a change in the TCD signal [53].

The results gained are chromatograms of intensity vs. time, containing peaks from which the gas composition can be determined (Figure 2.2b). The specific system used is the Varian 450- GC (Figure 2.2a). The machine contains a Varian Select Permanent Gases/CO_2 column. The column is composed of 2 parallel columns, one which is a Molsieve 5Å and the other a PoraBOND Q. The Molsieve separates permanent gases (oxygen, nitrogen, methane, carbon monoxide) and the PoraBOND can resolve carbon dioxide and water. The PoraBOND also elutes a composite peak of permanent gases. The gas chromatograph is capable of detecting CO, CO_2, CH_4, O_2, H_2O, but not H_2 because it has a thermal conductivity similar to the carrier gas used, He.

2.1.3 Partial Oxidation of Methane

Catalyst activation experiments with POM were performed in a gas mixture with 50cc/min He as a carrier gas, 8cc/min CH_4 and 4cc/min O_2 while ramping the temperature up to 900°C at 4°C per minute. The O_2/CH_4 ratio of ½ was chosen based on the optimum ratio for the POM reaction. Initially, CH_4 and O_2 are flowed and measured by the GC at room temperature to identify conditions when no reaction is occurring. From the initial chromatograms, a correction factor based on differences in thermal conductivity between O_2 and CH_4 is determined and applied so that $CH_4 = 2O_2$. Areas under the gas peaks can then be used to determine the gas conversions over time with temperature as well as the selectivities for a particular product during POM. The conversion is the amount of reactant that is converted to product. The GC measures output gas from the reactor which is the amount of unconverted gas. Selectivity is the tendency of the reaction to favor one product among several competing ones. In our case, as described, the competition in an environment of O_2 and CH_4 is between the POM and complete oxidation reactions, with produces gases of either H_2 and CO or H_2O and CO_2 respectively. Because we cannot detect H_2 in the GC due to the use of He as a carrier gas and because H_2O is detected at a much later time dependent on its elution, CO formation is analogous to H_2 production, based on the POM reaction, and CO_2 formation is equivalent to H_2O formation, based on the complete oxidation equation described earlier. The equation for conversion of CH_4 is then:

$$CH_4 \text{ percent conversion} = \frac{CH_{4\,in} - CH_{4\,out}}{CH_{4\,in}} * 100 \qquad (2.1)$$

where $CH_{4\ in}$ is the original, unaltered value of CH_4 determined before reaction proceeds, and $CH_{4\ out}$ is the CH_4 value measured by the GC as the reaction proceeds over time. Oxygen conversion is calculated in the same manner. Selectivity for a particular product is determined based on the amount of CH_4 consumed. For every CH_4 used, either 1 CO or 1 CO_2 is formed. CO_2 values are calibrated with a correction factor determined during the time when the complete combustion reaction is occurring and CO_2 is the only product. In this case the amount of CH_4 consumed should be equal to the CO_2 produced. To calculate CO_2 selectivity, the following process is followed:

$$CO_2 \text{ percent selectivity} = \frac{CO_{2\ out}}{CH_{4\ consumed}} * 100 \quad (2.2)$$

where $CH_{4\ consumed} = CH_{4\ in} - CH_{4\ out}$, and $CO_{2\ out}$ is the measured GC value because CO_2 is a product gas. CO selectivity is then 1- CO_2 percent selectivity.

2.1.4 Steam Reforming

Catalytic performance was also tested with the steam reforming reaction, with several modifications made to the reactor system for POM. In order to add steam to the gas mixture in the appropriate amount, the vapor pressure of water was used; as temperature is increased, the equilibrium concentration of water vapor will increase. This is described by the steam saturation curve and the Antoine equation [54]. For steam, this equation is

$$P = 133.332 * \exp\left(18.3036 - \frac{3816.44}{T - 46.13}\right) \quad (2.3)$$

where P is pressure in Pascal and T is temperature in Kelvin. In this case, the experiments are performed at atmospheric pressure and the adjustable parameter is the temperature. To maintain conditions similar to partial oxidation experiments, 8cc/min of methane and 50 cc/min of helium were used. The water temperature required to have a 1 to 1 steam to methane ratio was then calculated using partial pressures and the Antoine equation.

To produce steam, a saturator was used that bubbles the reactor gas mixture though water to mix in steam. The bubbler is contained within a heating jacket containing a thermocouple to be heated to the appropriate temperature. Gas lines leading from the bubbler to the reactor tube were heated to 100°C to avoid condensation of steam in the lines. To collect the steam after it had reacted with the catalyst, a condenser system was used. The reactor tube outlet is connected to a condenser immersed in a cold bath that condenses and collects the steam. The remaining gas products in the mixture are directed into the GC for analysis of conversions and selectivities. A diagram of the entire system is shown in Figure 2.3.

2.2 Characterization techniques

2.2.1 X-ray Diffraction

X-ray diffraction (XRD) is a characterization technique used to gain phase and structure information about a material. X-ray radiation is produced when high velocity electrons are accelerated and collide with a metal anode, most commonly copper. These X-rays interact with a crystalline material to produce a diffraction

pattern. Bragg's Law describes the relationship (Figure 2.4) between incident wavelength, angle, and interplanar spacing which can then be related to the plane indices (hkl). From the diffraction technique we can obtain a pattern in the form of a plot of intensity versus 2θ which can be indexed with the (hkl) values of the planes responsible for diffraction. With powder samples, crystal orientation is random and we will produce a plot with all possible plane reflections of the material [55].

The instrument used was a Siemens D5000 diffractometer equipped with a monochromator. The incident radiation was Cu Kα with a characteristic wavelength of 1.54Å. A quartz slide and petroleum gel were used to disperse the sample. Data was collected at a scan speed of 2°/min with a step size of 0.04°. Analysis of results was performed with Materials Data, Inc. (MDI) JADE 9.0 software to subtract background and identify peaks with X-ray powder diffraction files.

2.2.2 Transmission Electron Microscopy

Transmission electron microscopy (TEM) is a characterization technique that can be used to examine the microstructure and composition of materials with high resolution. The TEM uses a parallel, high energy electron beam to illuminate samples. The ionizing beam interacts with the specimen giving rise to secondary signals that can be used to gain information about the material. Interaction phenomena include elastic scattering, inelastic scattering, x-ray production, and

generation of secondary electrons [56]. Figure 2.5 shows some of the signals produced from electron solid interactions.

The TEM system magnifies and focuses the image created after specimen beam interaction, where the main source of image contrast is elastically scattered electrons. To achieve this, several sets of magnetic lenses are used that provide a magnetic field to direct electrons. The magnetic lenses are composed of coils of copper wires, and focus, intensity, and magnification are changed depending on the lens current applied. Apertures are also used in conjunction with lenses to adjust the divergence of electrons through the lenses [56]. The entire system first requires an electron source to produce the beam. This usually is a thermionic gun of LaB_6 or a field emission source composed of a fine tungsten needle. A series of condenser lenses is next used to focus the illumination onto the sample. The sample is contained within a sample port and goniometer to hold, move, and tilt the specimen. An objective lens system is next used to form an image or diffraction pattern of the sample. Electrons emerging from the specimen are focused by the objective lens into a diffraction pattern on the back focal plane and form an image on the image plane (Figure 2.6). Intermediate lenses then magnify the image formed by the objective lens system and the image is projected onto a phosphor screen where it can be viewed or fed into an image recording charge-coupled device (CCD) detector [56]. A diagram of the entire microscope is shown in Figure 2.7.

2.2.3 STEM

In scanning transmission electron microscopy (STEM) the beam of electrons is focused into a small probe which is scanned over the sample. The beam must scan parallel to the optic axis to maintain a constant angle [56]. Image formation in STEM is not dependent on lenses but rather on the probe. The beam interacts with the sample by producing a convergent beam electron diffraction (CBED) pattern. Several signals can be collected from this interaction. A bright field detector can be used to collect the transmitted beam or an annular dark field (ADF) detector can be used to collect scattered electrons. Using a high angle annular dark field detector (HAADF) that collects electrons scattered through a high angle, a Z-contrast image can be obtained in which contrast is dependent on atomic number of the elements present. A schematic of the different detector geometries is shown in Figure 2.8. The small probe size makes the STEM technique well suited for high spatial resolution chemical analysis of a sample. Rastering the probe over the sample also allows for mapping of an area where chemical information is gained at every pixel in the STEM image, giving the distribution of elements in a sample.

2.2.4 EDX

Chemical information can be gained through analytical transmission electron microscopy, making use of the signals gained from electron sample interactions. In energy dispersive X-ray spectroscopy (EDX), characteristic X-rays produced during beam-specimen interactions are utilized. Characteristic X-

rays are produced when the electron beam interacts with the inner shell electrons of the atoms in a sample. The electrons in the beam cause inner shell electrons to be ejected from the atom in a process called ionization. When an outer shell electron moves to the low energy state to fill the vacancy, its excess energy is released in the form of a photon that has energy equal to that of the difference between the two shells [57]. Only certain shell transitions can occur and energy levels of electron shells have certain unique values that are dependent on atomic number. Thus, energy levels of different electron shells are different for different elements and the photons emitted from atoms are characteristic and can be used to identify the elements present. EDX provides data of intensity versus energy where characteristic peaks will appear at their corresponding energies. Each element will emit a family of X-rays for different transitions between different shells. If the peaks result from ionization of the innermost shells, they are K family X-rays, if the ionization occurs within the second shell they are L X-rays, and vacancies from the third shell result in M X-rays. Within a family, electrons from different shells can fill a vacancy with the most probable transitions leading to the brightest peaks. The most common transition is α, followed by β. A Kα X-ray is produced when an electron transitions from the L to K shell while a Kβ arises when an electron transitions from the M to K shell. A hole in the L shell that is filled by the M shell produces an Lα X-ray [57]. A diagram showing several of these transitions is shown in Figure 2.9.

An EDX spectrometer will deliver quantitative information about how many X-rays of a given energy are produced. The detector, often called a Si(Li)

detector, is composed of single crystal silicon with lithium added to compensate for impurities in the Si lattice. Electrons from the Si atoms can be moved from the valence to conduction band when an X-ray hits the semiconductor, creating electron hole pairs. The number of electron hole pairs generated by one X-ray is proportional to the energy of the X-ray [57]. The detector is cooled to prevent the formation of thermally generated electron hole pairs. The formation of electron hole pairs causes voltage pulses that are translated to X-ray counts. An EDX plot is then created with X-ray counts versus X-ray energy. Electrons in the beam that penetrate the electron shells can interact inelastically with the Coulomb field of the nucleus. This causes them to change momentum and emit an X-ray known as bremsstrahlung which can have any energy up to the beam energy [56]. The bremsstrahlung appears on an EDX plot with a continuous energy spectrum on which the characteristic peaks are superimposed. It is treated as a background and is fitted and subtracted when looking at peak intensities for characteristic lines.

Quantification of EDX data can be achieved using the Cliff-Lorimer ratio method [58]. Cliff and Lorimer demonstrated that the ratio of intensity for two different elements in the EDX spectrum can be related to the concentration ratio of the two elements. The equation for 2 elements A and B is:

$$\frac{C_A}{C_B} = K_{AB}\frac{I_A}{I_B} \tag{2.4}$$

where K_{AB} is called the Cliff-Lorimer K factor that can be calculated or determined experimentally using a standard sample of known composition. To determine the absolute values of C_A and C_B the second equation

$$C_A + C_B = 1 \tag{2.5}$$

is used. To examine systems of more than 2 components, another equation relating the third element to one of the first two is used.

2.2.5 EELS

Electron energy loss spectroscopy (EELS) is another technique used to determine chemical information from a sample. As compared to EDX, EELS has a better sensitivity to light elements with Z less than 10 and offers better spatial resolution [59]. It is very useful in STEM mode to obtain localized elemental and electronic information about a sample. As described earlier, several signals can be collected after electrons interact with a sample. In the case of EELS, the signal collected is the energy distribution from electrons that have undergone inelastic collisions with a sample and lost energy. A magnetic prism spectrometer bends the transmitted electrons and creates a distribution of electron counts based on energy loss [60]. Inelastic scattering occurs when incident electrons are scattered by atomic electrons. Plasmon excitations occur when the beam interacts with outer shell valence electrons and are one important kind of inelastic scattering that results in energy loss. Energy loss also occurs when core shell electrons are excited to a higher atomic orbital. When core electrons are excited by the electron beam, ionization edges are created which are representations of the transfer of energy from the incident electron to the inner-shell electron [59]. An idealized EELS spectrum showing these details is shown in Figure 2.10.

EELS provides energy loss spectra with a low-loss region containing peaks from plasmon excitation. The low-loss region also contains the zero-loss

peak at 0eV which is formed from the electrons that were either transmitted or that underwent elastic scattering. The high-loss portion of an EELS spectrum is where ionization edges occur [59]. Ionization edges are superimposed on plasmon peaks which make up the background of the spectrum. To determine elemental composition of a sample, ionization edges are used. Because a certain ionization edge occurs at a certain energy loss based on the material, EELS can be used to identify the elements present within the region selected by the electron beam. Ionization edges are examined in terms of atomic number and atomic shell. For example, excitation of the $2p^{1/2}$ and $2p^{3/2}$ electrons give rise to the L_2 and L_3 edges, and transitions from $3d^{3/2}$ and $3d^{5/2}$ states create the M_4 and M_5 edges [60]. To quantify an EELS spectrum, the background of an ionization edge is subtracted using a power law relationship and the remaining intensity describes the concentration of the corresponding element.

2.2.6 *Ex-situ* Instruments

Nanocharacterization using TEM, STEM, EELS, and EDX was performed using a JEOL 2010F 200 kV microscope at the John M. Cowley center for high resolution electron microscopy at Arizona State University, shown in Figure 2.11. The 2010F is equipped with an EDAX X-ray detector and a Gatan ENFINA energy-loss spectrometer for high spatial resolution microanalysis. The microscope can be operated in STEM mode and has an information limit of 0.14 nm.

STEM EELS elemental mapping of catalysts was performed using the JEOL ARM 200F (Figure 2.12). The microscope contains a CEOS CESCOR aberration corrector. Spherical aberration is a property of cylindrical electron lenses that causes electrons scattered at different angles with respect to the optic axis to be focused at different points, causing image blurring [61]. The corrector incorporates hexapole lenses and a computer assisted procedure that assesses aberrations using diffractograms from amorphous sample regions. This allows for greatly improved, sub-Ångstrom resolution. The ARM 200F can be operated at 200kV, 120kV and 80kV and has a resolution of 0.8 Ångstrom. It has a JEOL X-ray detector and a Gatan Enfinium EELS spectrometer as well as the ability to correct drift when doing high spatial resolution mapping.

TEM samples were prepared by crushing the powders under glass microscope slides to break agglomerates. The powders were then dispersed onto holey carbon grids. Samples are placed under a heat lamp for several hours to remove any organic compounds and prevent carbon deposition in STEM mode.

2.2.7 *In-situ* TEM

In-situ electron microscopy allows for observation of experiments conducted in real time within the microscope. In the field of catalysis, *in-situ* environmental TEM (ETEM) allows us to monitor interactions between gases and solid catalysts and observe changes [62]. Normally the TEM column is held under high vacuum to minimize gas scattering of the electron beam. The column can be modified to accommodate a differential pumping system which allows for

observation of samples under low pressure of gas. The system works by restricting the amount of gas that can enter the specimen chamber with apertures and by then pumping gas out using several pumps [62]. The advantage of using this type of system is that different types of TEM holders such as a heating holder can be used along with the gas system.

The system used for *in-situ* environmental TEM was the 200 kV FEI Tecnai F-20 ETEM (Figure 2.13). The microscope has a three level differential pumping system with two sets of apertures that restrict the leak rate of gas into the microscope column, shown in Figure 2.14. The gas leaked through the apertures is pumped out by a turbo molecular pump. The area between the condenser aperture and the viewing chamber is pumped using a molecular drag pump, and the region between the condenser aperture and gun chamber is pumped with an ion pump [63]. The aperture size, distance between apertures, and pumping speed all affect the resolution and the gas pressure in the cell. In this microscope, the information limit is 0.14 nm and the maximum gas pressure is 8 Torr. It is equipped with a Gatan imaging filter that allows for EELS to be performed in-situ. Experiments on catalysts are performed in the gas environment using a heating holder. The holder used is a Gatan double tilt heating holder containing an inconel furnace and a water cooling system to cool O-ring components of the holder. The holder can be heated to 900°C in vacuum and in different gas environments the maximum temperature available will depend on the thermal conductivity of the gas.

In-situ TEM samples were prepared by dispersing powder samples on platinum (Pt) grids. Pt grids were made by punching out 3mm disks from a Pt mesh by Alfa Aesar. Pt was chosen because an inert support that will not react with the sample or holder at high temperatures is needed during ETEM experiments.

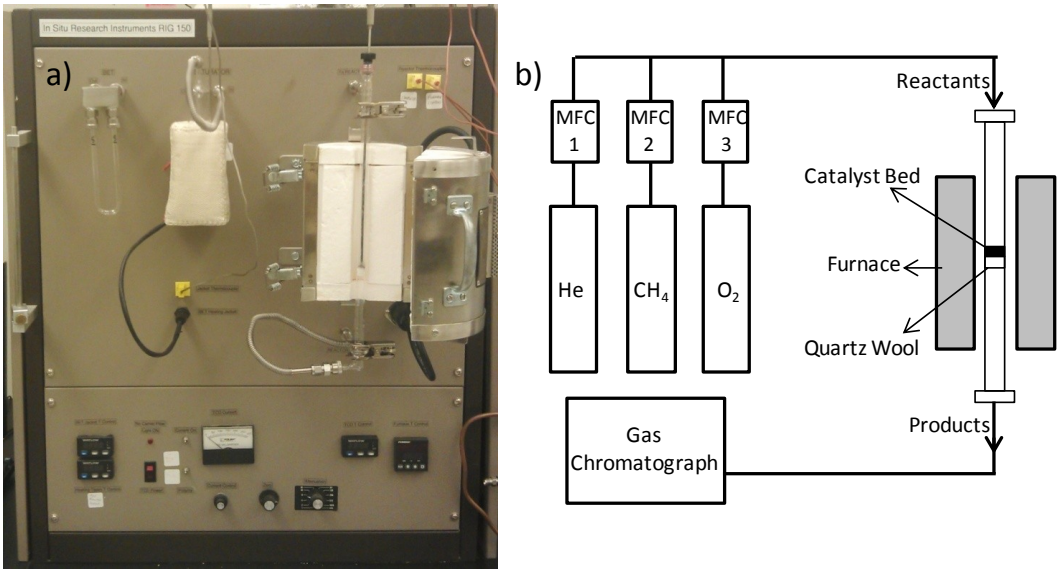

Figure 2.1: Reactor system used for catalytic experiments showing a) ISRI micro reactor b) schematic of reactor system and tube.

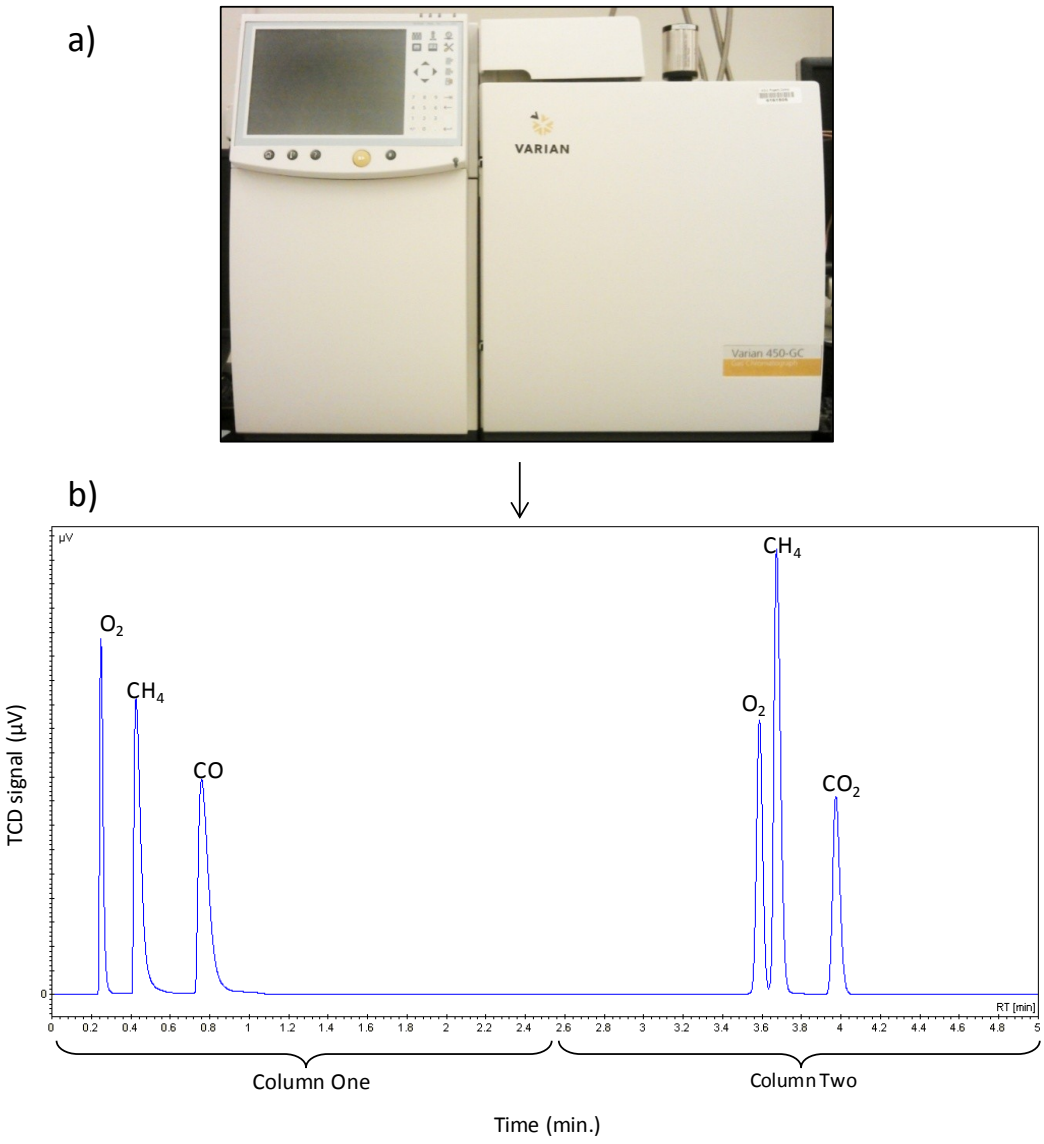

Figure 2.2: a) Varian 450 Gas Chromatograph and b) typical output chromatogram for POM reaction.

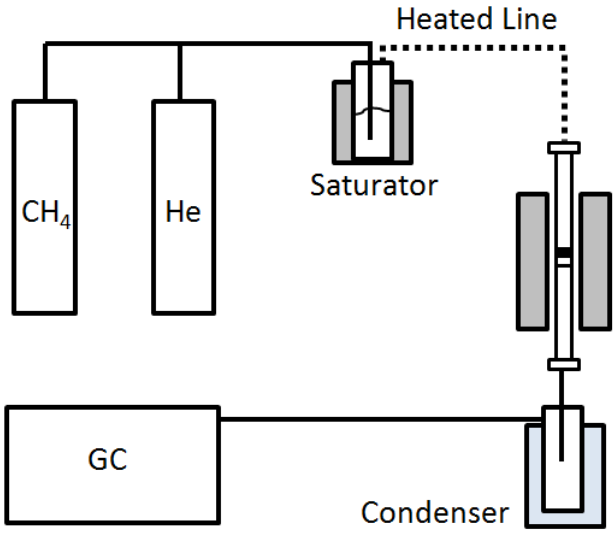

Figure 2.3: Diagram of steam reforming setup including heated regions in grey and cooling in blue.

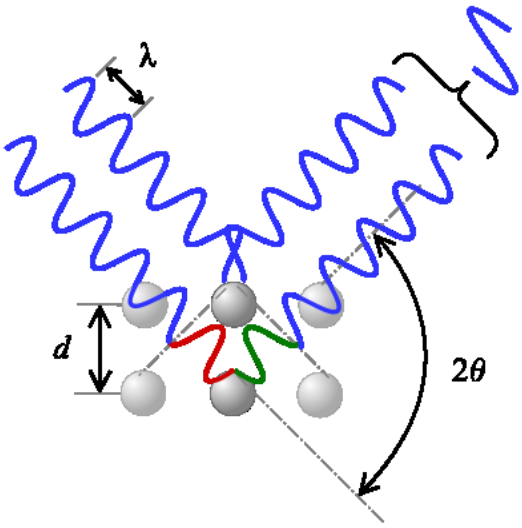

Figure 2.4: Illustration of Bragg's law for X-ray of incident wavelength λ [64].

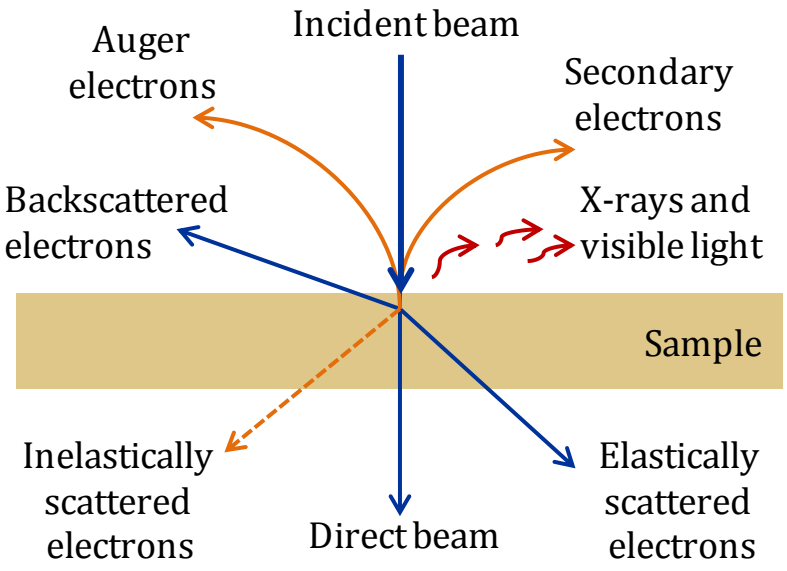

Figure 2.5: Diagram showing the different signals produced during electron beam interaction.

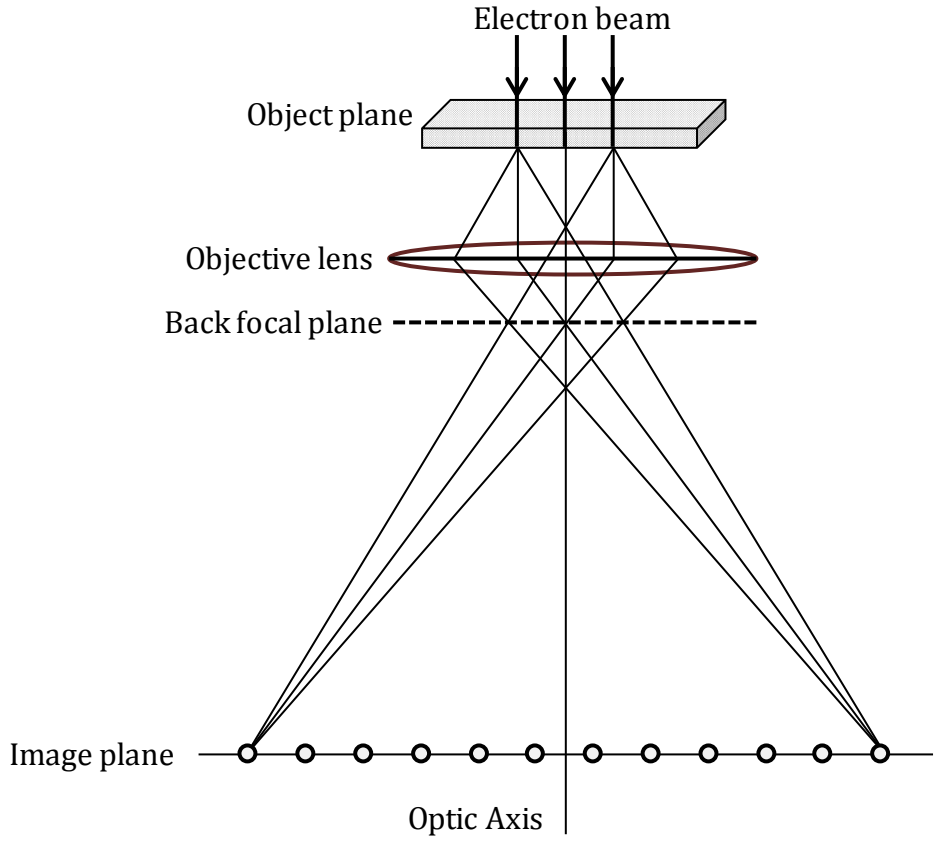

Figure 2.6: Schematic showing image formation principle of the objective lens in the TEM.

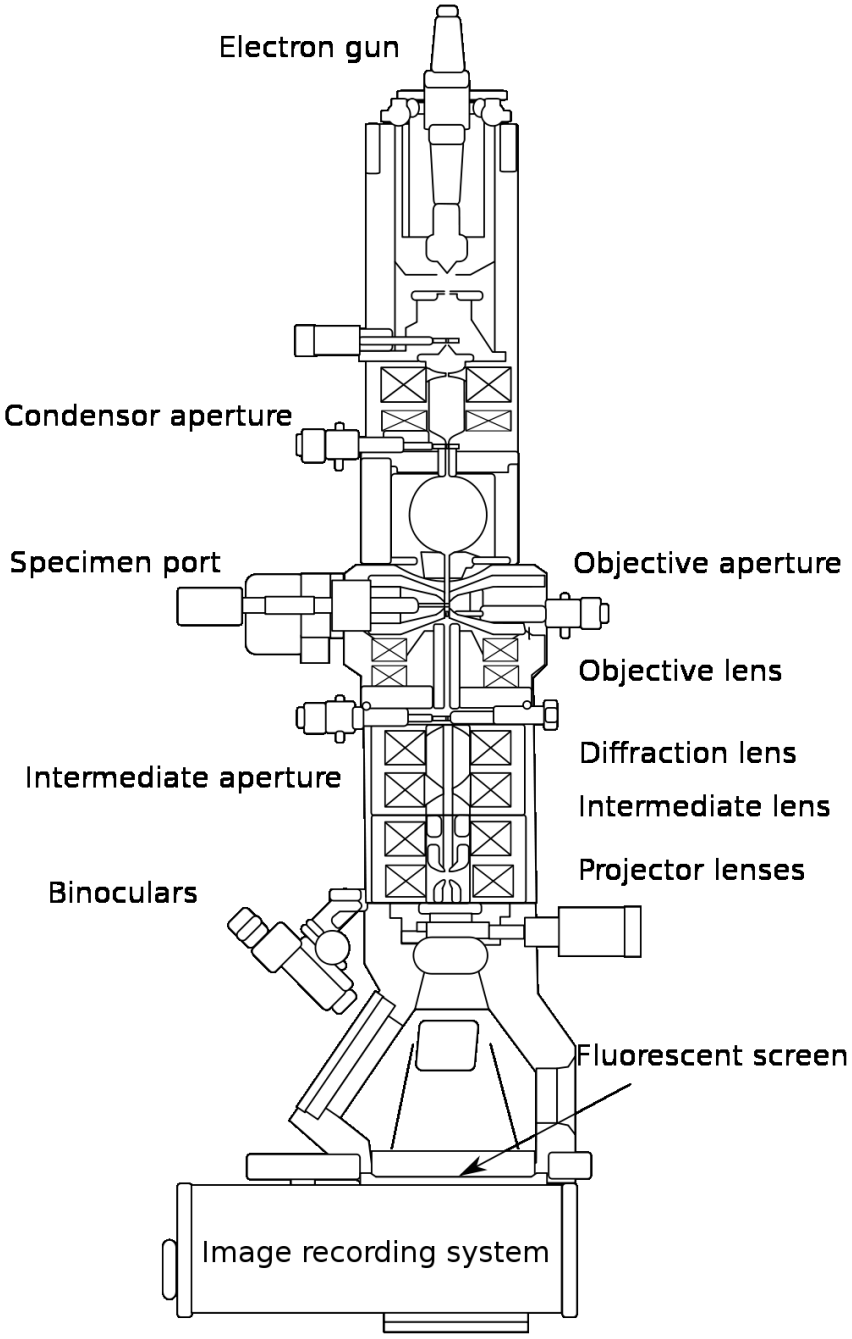

Figure 2.7: Diagram of the transmission electron microscope and its important components [65].

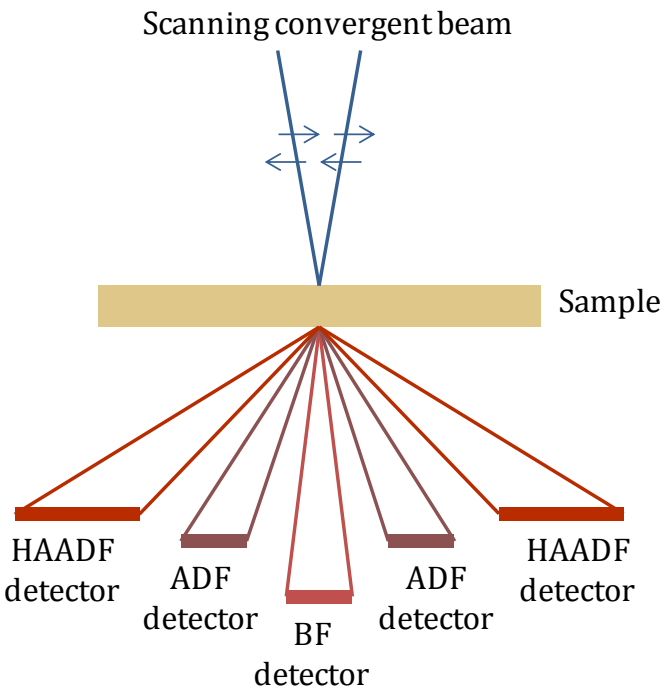

Figure 2.8: Diagram showing the scattered beams formed after a convergent STEM probe interacts with a sample, and the possible detector geometries.

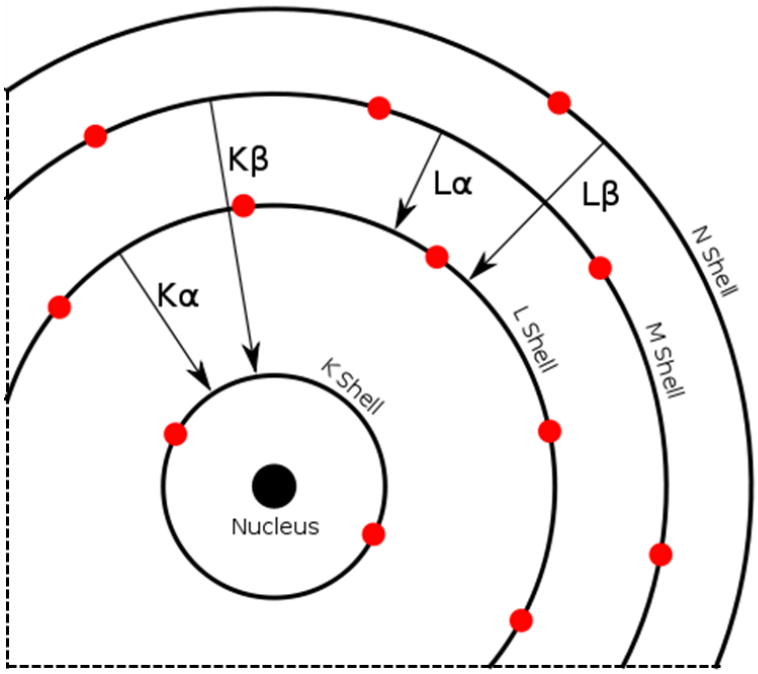

Figure 2.9: Atomic shells and transitions that lead to characteristic X-ray emissions [66].

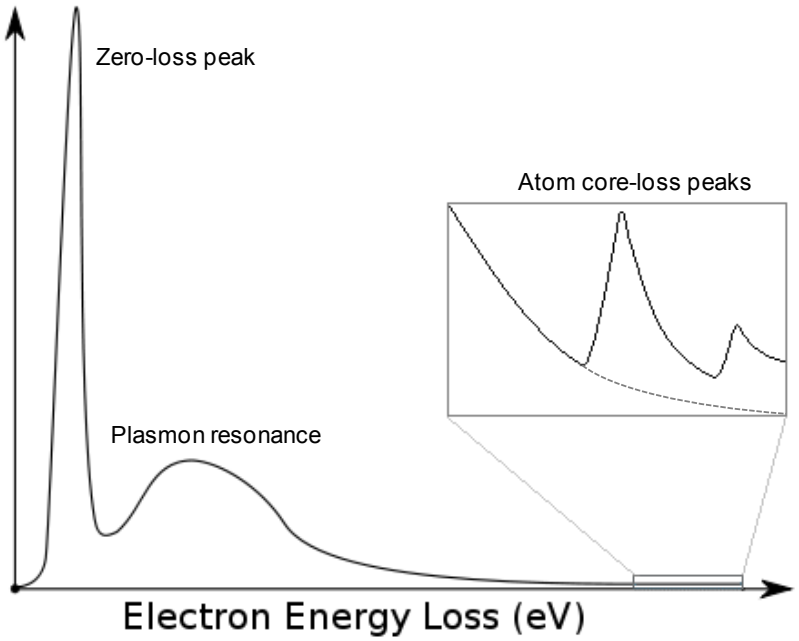

Figure 2.10: Idealized EELS spectrum, showing the zero-loss peaks, plasmon resonance, and core-loss peak. Adapted from [67].

Figure 2.11: JEOL 2010F transmission electron microscope at Arizona State University.

Figure 2.12: JEOL ARM 200F transmission electron microscope at Arizona State University.

Figure 2.13: FEI Tecnai F-20 environmental transmission electron microscope at Arizona State University.

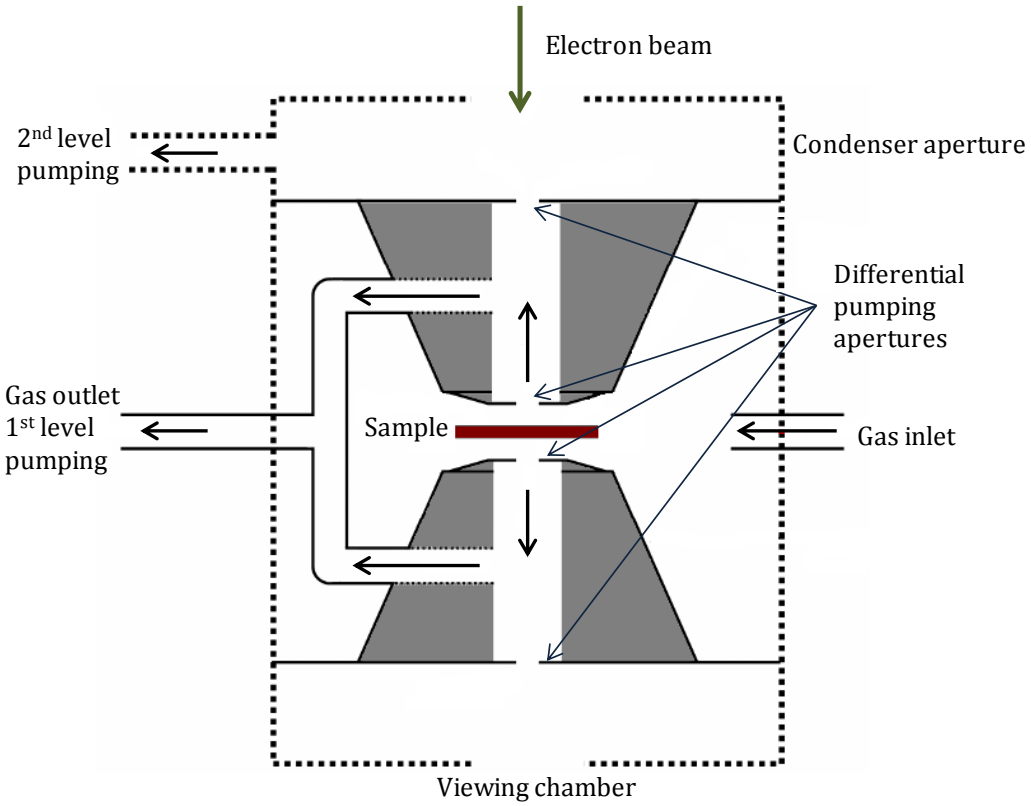

Figure 2.14: Diagram showing the differential pumping system contained in the FEI Tecnai F-20 ETEM.

Chapter 3

CATALYST SYNTHESIS AND X-RAY DIFFRACTION

3.1 Spray Drying

Spray drying is a materials synthesis method that creates solid particles from a liquid solution. The technique is simple, has a quick drying time, and produces a high volume of uniform, ultrafine particles [68]. Our laboratory scale system has been used to successfully synthesize nanopowders of pure and rare earth doped CeO_2 [50]. To incorporate Ni into CeO_2 intimately, we used the spray drying system to synthesize several Ni doped CeO_2 compositions.

3.1.1 Principles and Equipment

With this method, precursors are dissolved in nanopure water to create an aqueous solution. The mixture is fed into an air brush that sprays a mist of fine droplets into hot air to dry them rapidly, forming nanoparticle aggregates. The airbrush used, shown in Figure 3.1, is attached to an air compressor and the settings of the air flow and nozzle position are adjusted to provide the finest spray. The nozzle diameter of the airbrush is 0.2 mm and the flow rate of the liquid feed in the air brush was found to be optimum at 0.7 cm^3/min.

Air brush spray is directed into a spherical glass drying chamber where hot air for drying is provided by a heat gun, shown in Figure 3.2. Compressed air flows through the heat gun with a flow rate of between 1 and 1.5 standard cubic feet per minute (SCFM). The heat gun temperature is set to 800°C, providing a temperature of 350°C inside the chamber. This temperature is ideal because it is

below the melting temperature of the glass globe, it is high enough to evaporate water, and it is close to the decomposition temperatures of nitrates used. Attached to the drying chamber is a cyclone particle collector (Figure 3.3) which separates the solid nanopowder from air. The cyclone is attached to the exhaust where the air exits the system. The entire spray drying system is pictured in Figure 3.4.

3.1.2 Synthesis

To make the spray drying solution, the amount of precursor used is calculated based on the chosen solution concentration and the desired composition of the final material. The concentration of precursors in solution for the spray dryer is 0.05M. This concentration was chose so fewer precursor molecules were present in each droplet, allowing for the formation of smaller nanoparticles. Nitrate precursors were chosen for the spray drying system based on their favorable solubility and decomposition temperatures. In this work precursors used were cerium nitrate hexahydrate ($Ce(NO_3)_3.6H_2O$), gadolinium nitrate hexahydrate ($Gd(NO_3)_3.6H_2O$), and nickel nitrate hexahydrate ($Ni(NO_3)_2.6H_2O$), all from Sigma Aldrich with purities of 99.999%. The decomposition temperatures of the nitrates into metal oxides, NO_x, and O_2 are 295°C, 365°C, 305°C for cerium nitrate, gadolinium nitrate, and nickel nitrate respectively [69]. Nitrates were weighed, added to nanopure water in the desired ratios, and stirred for at least 30 minutes to ensure a uniform solution.

Powder samples were collected from the cyclone separator using ethanol. They were then calcined to form nanoparticles of uniform size. An initial heat

treatment of 500°C for 4 hours was used to decompose residual nitrates and remove any moisture from the powder. A second heat treatment of 700°C for 4 hours was used to give a larger particle size, promote crystallinity in the samples, and ensure complete oxidation to the desired product.

Catalyst materials synthesized were pure CeO_2, $Gd_{0.1}Ce_{0.9}O_{2-y,}$ $Ni_{0.1}Ce_{0.9}O_{2-y}$, $Ni_{0.2}Ce_{0.8}O_{2-y}$, and $Ni_{0.1}Gd_{0.1}Ce_{0.8}O_{2-y}$. Table 3.1 summarizes sample names which are abbreviated as CeO_2, 10Gd, 10Ni, 20Ni, and 10NiGd respectively. Nitrates were added to solution with the correct molar ratios for doping. The first doped sample, 10Ni, with 10 at.% Ni doped into CeO_2 was chosen because this is the reported solubility limit of Ni in CeO_2 [37,38]. The second sample (20Ni), with 20 at.% Ni was chosen to add excess Ni beyond the 10% solubility limit and have an extra 10% in the form of a separate Ni phase that will contribute to catalyst performance. For the third sample, 10NiGd, 10 at.% Ni was chosen along with 10 at.% Gd to explore whether the addition of Gd would affect the interaction between Ni and CeO_2. Plain CeO_2 and 10Gd were synthesized as reference materials. These two reference materials were subjected to higher heat treatment of 900°C for 6 hours.

3.2 X-ray Diffraction Results

Crystal structure of the samples was determined using XRD as described in section 2.2.1. An analysis procedure with JADE 9.0 was used to first fit and subtract the background. Then the structure was identified using the powder diffraction file database. Figure 3.5 shows the XRD pattern obtained for 10Ni.

This pattern shows peaks at positions corresponding to the structure of CeO_2 (JCPDS 00-004-0593). No substantial peaks of segregated Ni or NiO phases are observed which could indicate that Ni is amorphous, very finely dispersed, or is incorporated into the CeO_2 lattice. If Ni doping into CeO_2 has occurred we would expect the fluorite lattice to contract and to observe peak shifts of CeO_2 structure to higher angles. This was explored further using Vegard's law, which can be used to estimate the lattice parameter for solid solutions of one metal oxide into another. The relationship describes how a linear relationship exists between the lattice parameter and the concentration of the solute. Using Vegard's law, a set of relationships between concentration, ionic radii of metals and dopants, and lattice parameter can be derived [70]. The relationship for CeO_2 can be expressed by:

$$a = 5.411\text{Å} + \sum m_k(0.022\Delta r_k + 0.0015\Delta z_k)\ \text{Å} \quad (3.1)$$

where *a* is the lattice parameter of the ceria solid solution, Δr_k is the difference in ionic radii between the kth dopant and the Ce^{4+} radius in eight-fold coordination (0.97Å), Δz_k is the valence difference $(z_k - 4)$, and m_k is the mole percent of the dopant. In this case the lattice parameter of CeO_2 is 5.411Å based on JCPDS file 00-004-0593. The value of atomic radius for Ni^{2+} in eight-fold coordination is estimated to be 0.83 Å [71]. Using equation 3.1 and assuming all 10% of Ni dopes into the lattice, the expected lattice parameter for 10Ni is 5.350 Å. Using JADE and the XRD pattern of Figure 3.5 we calculated our actual lattice parameter. The software uses shifts in 2θ values of reflections to calculate *a* using equation 3.2 and averaging over the first 6 reflections.

$$a = \lambda\sqrt{h^2 + k^2 + l^2}/(2\sin\theta) \quad (3.2)$$

For the 10Ni sample the calculated lattice parameter is 5.399 ± 0.003 Å. This value is smaller than the expected lattice parameter of 5.411Å for CeO_2. To explore whether the 10Ni sample exhibits this lattice parameter contraction because of Ni doping, plain spray dried CeO_2 was tested with XRD. Results for pure CeO_2 are shown in Figure 3.6. The lattice parameter calculation reveals that the lattice parameter of our ceria is 5.398 ± 0.001 Å . The lattice parameter is smaller than expected for ceria. This result means that the 10Ni doped sample does not display a peak shift relative to pure, spray dried CeO_2. Assuming the material obeys Vegard's law and equation 3.1, this would mean that our sample does not have substitutional doping of Ni into CeO_2.

XRD results for the 20Ni sample are shown in Figure 3.7. We witness peaks corresponding to CeO_2 as well as those corresponding to NiO (JCPDS 00-047-1049). The lattice parameter based on peak shifts was calculated using the same procedure as for the 10Ni sample. For the 20Ni doped sample the lattice parameter is 5.398 ± 0.003 Å. This value is close to CeO_2 and 10Ni, indicating that no doping has occurred based on equation 3.1. One group's work on samples doped with 10 and 20 at.% Ni also reveals no change in lattice parameter between CeO_2 and doped samples [37]. This was explained as Ni doping causing a lattice contraction, but the formation oxygen vacancies causing an expansion, leading to no net change. Other groups have seen a slight change in lattice parameter and attributed it to Ni doping [38,39]

For the 10NiGd sample, results are shown in Figure 3.8. This sample contains a very slight peak shift which gives a lattice parameter of 5.408 ±

0.003 Å. The ionic radius of Gd^{3+} in 8-fold coordination is 1.053 Å [71]. If only 10% Gd is doped into CeO_2, the expected radius is 5.414 Å, from equation 3.1. If both 10% Gd and 10% Ni dope into the sample, the expected radius is 5.353 Å, very similar to the expected radius for 10% Ni doping only. To examine the effect of Gd alone, XRD was performed on the 10Gd sample. These results are shown in Figure 3.9. Peak shifts to lower angles are witnessed and the lattice parameter for the material is 5.415 ± 0.001 Å, similar to what is expected based on calculations. It does appear that for 10NiGd both Ni and Gd are having an impact on the CeO_2 lattice, as the lattice parameter for 10NiGd is larger than CeO_2, 10Ni, and 20Ni, but smaller than 10Gd.

Broadening of X-ray diffraction peaks occurs from instrumental effects based on diffractometer conditions and through deviations from ideal crystallinity in samples. A small crystallite size causes peak broadening because of deviation from perfect Bragg scattering due to the crystal being finite [72]. Uniform strain in samples such as that caused by perfect substitutional doping causes the unit cell to expand or contract isotropically, which causes peak shifts, but does not cause broadening of x-ray lines. Non-uniform strain, on the other hand, through lattice distortions like point defects or dislocations can contribute to peak broadening. These distortions give rise to strain fields that cause variation in interplanar spacing and thus in 2θ. Analysis of peak broadening can give information about the microstructure of a material. To explore whether Ni incorporation into CeO_2 has caused lattice distortion rather than substitutional doping, we calculated the strain in the lattice using Williamson-Hall analysis [73]. This method examines

XRD peak broadening based on effects of both crystal size and strain. The Williamson-Hall equation is:

$$(\beta_t - \beta_0)cos\theta = \frac{0.9\lambda}{D} + 4\varepsilon\, sin\theta \quad (3.3)$$

where β_t is the total peak broadening, β_0 is the peak broadening due to instrumentation effects, D is the crystallite size, and ε is the strain. $(\beta_t - \beta_0)cos\theta$ can be plotted versus $4sin\theta$ and D is then calculated from the y-intercept while ε is calculated from the slope. From the XRD results of Figures 3.5 through 3.9, the strain and crystallite sizes were calculated using JADE. For pure CeO_2, the strain was found to be 0.057 ± 0.006%. For 10Gd, the strain was a higher value of 0.125 ± 0.024%. For the Ni doped samples of 10Ni, 20Ni, and 10NiGd, the strain values were 0.329 ± 0.040%, 0.345 ± 0.045%, and 0.309 ± 0.046% respectively. The Ni doped samples have a higher amount of strain than undoped ceria and 10Gd which could mean that Ni has interacted with the CeO_2 lattice, causing defects. Crystallite size was also gained from Williamson-Hall analysis. CeO_2 had the largest size of 98.0 ± 5.7 nm followed by 10Gd with 58.4 ± 8.9nm. 10Ni, 20Ni, and 10NiGd had crystallite sizes of 26.7 ± 2.9 nm, 35.4 ± 5.6 nm, and 22.4 ± 2.4 nm respectively. The large difference in size between 10Gd, CeO_2, and the Ni doped samples could be caused by differences in heat treatments. It is possible that the size difference between CeO_2 and 10Gd is because Gd can inhibit sintering of CeO_2 [49]. Table 3.2 summarizes XRD calculations for all 5 samples.

Overall, XRD has not given conclusive evidence for or against Ni doping in our samples. The absence of any lattice contraction most likely means that little to no substitutional doping has occurred. The XRD results show that the lattice

parameter is the same for pure ceria, 10Ni, and the 20Ni sample. The 20Ni sample displays peaks associated with crystalline NiO, indicating that there is a separate NiO phase present. 10Gd has a larger lattice parameter indicative of Gd doping in the sample. 10NiGd also exhibits a larger lattice parameter, but to a lesser degree. The three Ni containing samples have higher strain present which could mean Ni has interacted with CeO_2 in some manner. An overlay of XRD plots for the 5 samples is shown in Figure 3.10 where slight peak shifts can be observed and compared. It can also be seen that peaks for Ni doped samples are noisier and more broadened than for CeO_2 and 10Gd.

Table 3.1: Samples prepared by spray drying, their short form names, and the heat treatments performed.

Material	Abbreviation	Heat treatment
Pure CeO_2	CeO_2	900°C/6hr
$Gd_{0.1}Ce_{0.9}O_{2-y}$	10Gd	900°C/6hr
$Ni_{0.1}Ce_{0.9}O_{2-y}$	10Ni	500°C/4hr,700°C/4hr
$Ni_{0.2}Ce_{0.8}O_{2-y}$	20Ni	500°C/4hr,700°C/4hr
$Ni_{0.1}Gd_{0.1}Ce_{0.8}O_{2-y}$	10NiGd	500°C/4hr,700°C/4hr

Table 3.2: Summary of all XRD analysis on spray dried ceria-based samples including lattice parameter measurements, crystallite size, and strain.

Material	Lattice parameter (Å)	Crystallite size (nm)	Strain (%)
CeO_2	5.398 (0.001)	98.0 (5.7)	0.057 (0.006)
10Gd	5.415 (0.001)	58.4 (8.9)	0.125 (0.024)
10Ni	5.399 (0.003)	26.7 (2.9)	0.329 (0.040)
20Ni	5.398 (0.003)	35.4 (5.6)	0.345 (0.045)
10NiGd	5.408 (0.003)	22.4 (2.4)	0.309 (0.046)

Figure 3.1: Air brush used in spray drying system to atomize precursor solution.

Figure 3.2: Heat gun providing hot air for drying, attached to the drying chamber of the spray dryer.

Figure 3.3: Cyclone used for powder collection in the spray dryer, containing CeO_2.

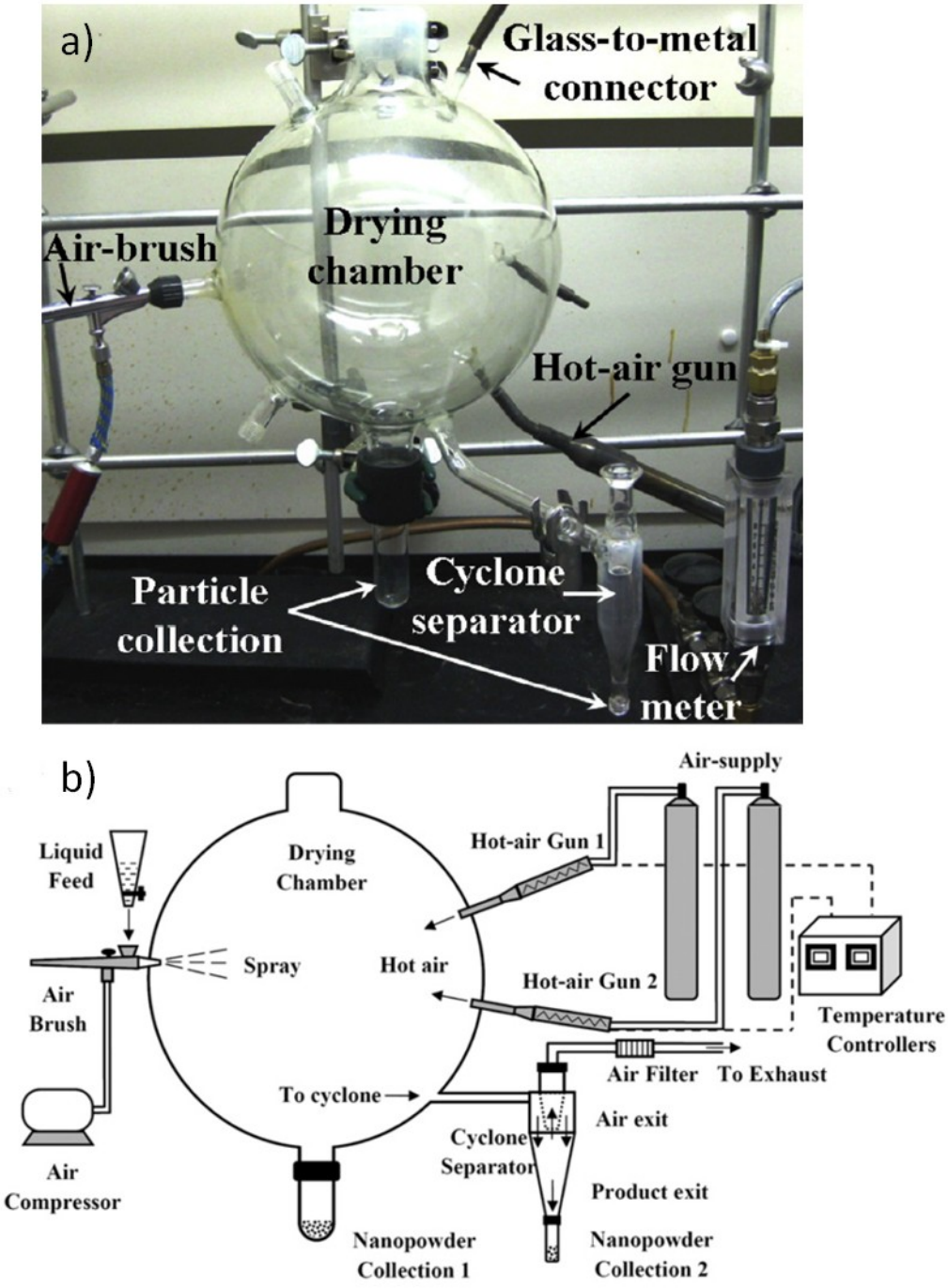

Figure 3.4: Complete spray drying system used to synthesize nanopowder catalysts with a) picture of the system, and b) schematic diagram of the system [2].

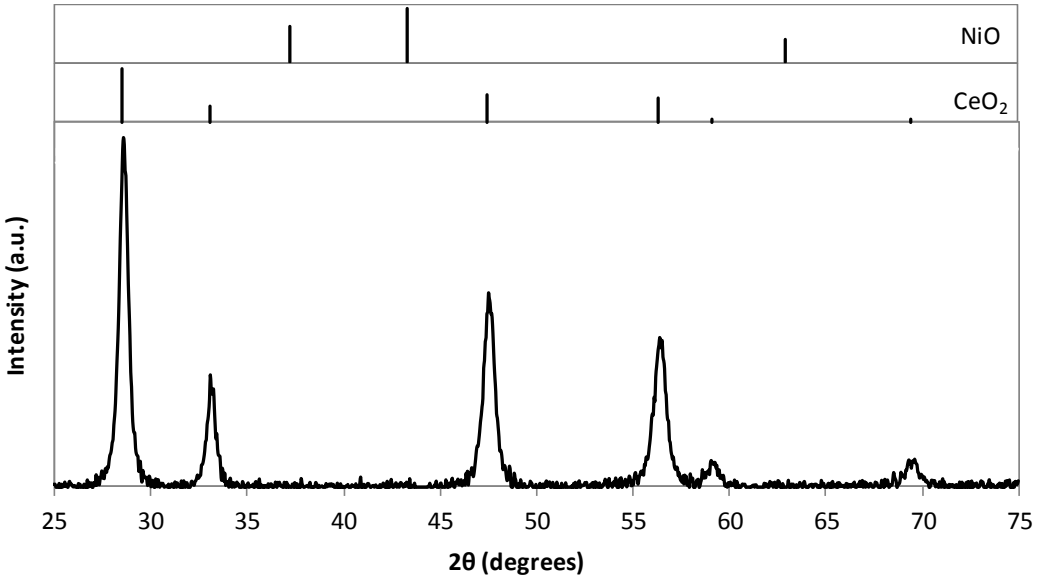

Figure 3.5: X-ray diffraction pattern for 10Ni with inset showing CeO_2 (JCPDS 00-004-0593) and NiO (JCPDS 00-047-1049) reflections.

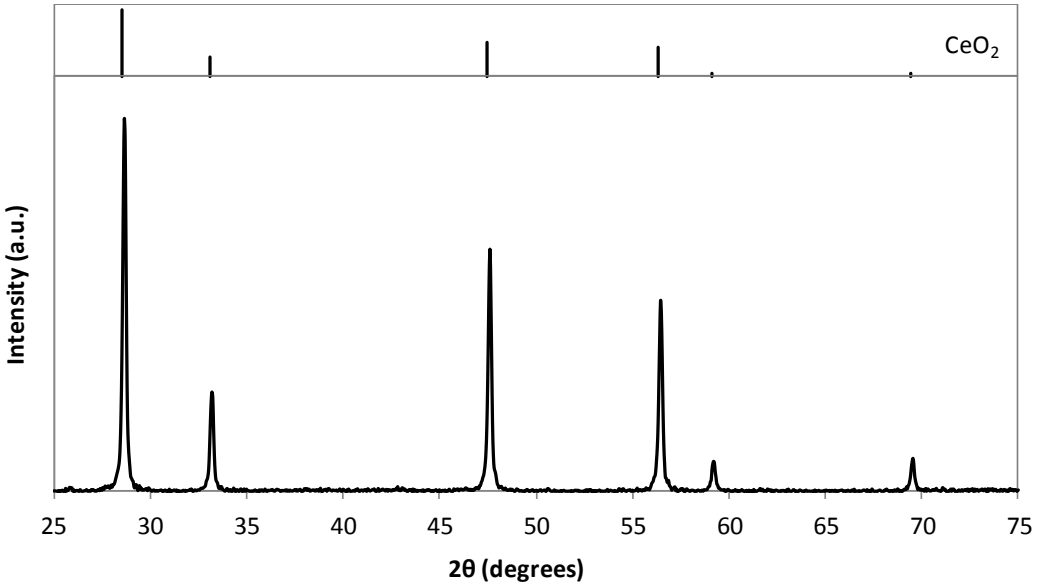

Figure 3.6: X-ray diffraction pattern for CeO_2 with inset showing CeO_2 reflection.

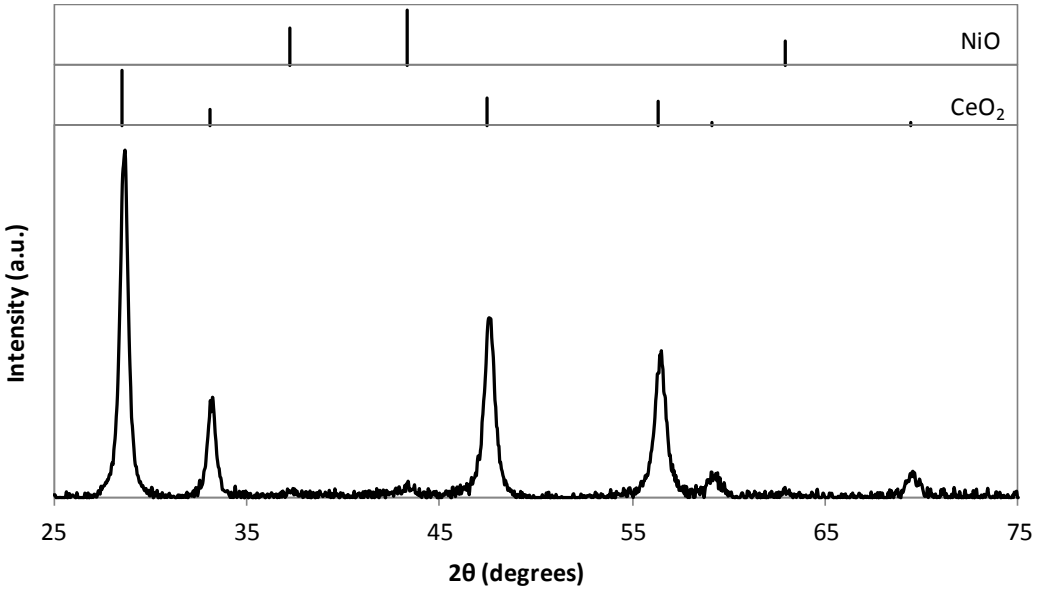

Figure 3.7: X-ray diffraction pattern for 20Ni with inset showing CeO_2 and NiO reflections.

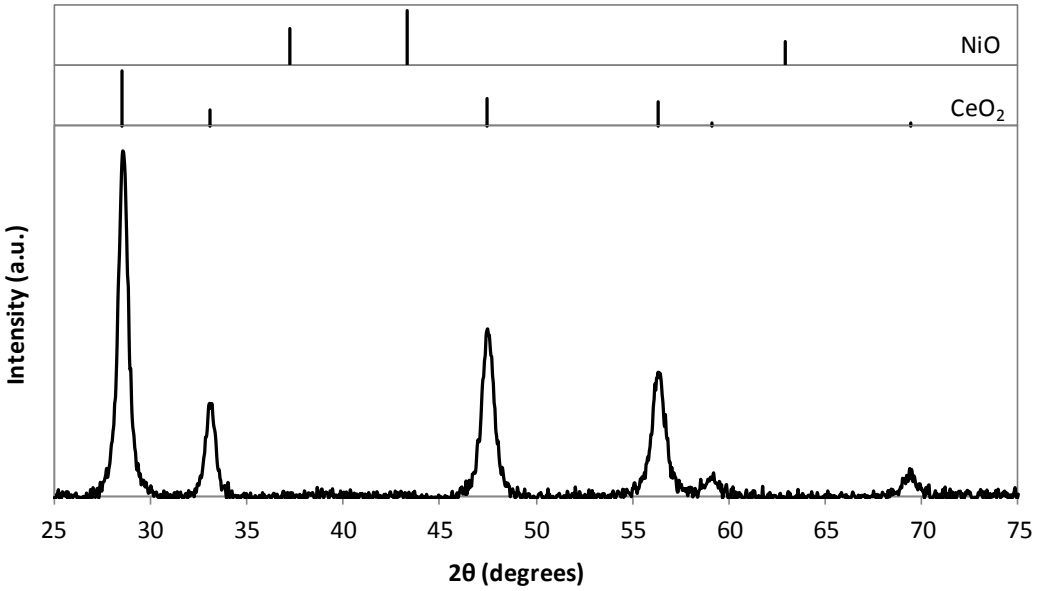

Figure 3.8: X-ray diffraction pattern for 10NiGd with inset showing CeO_2 and NiO reflections.

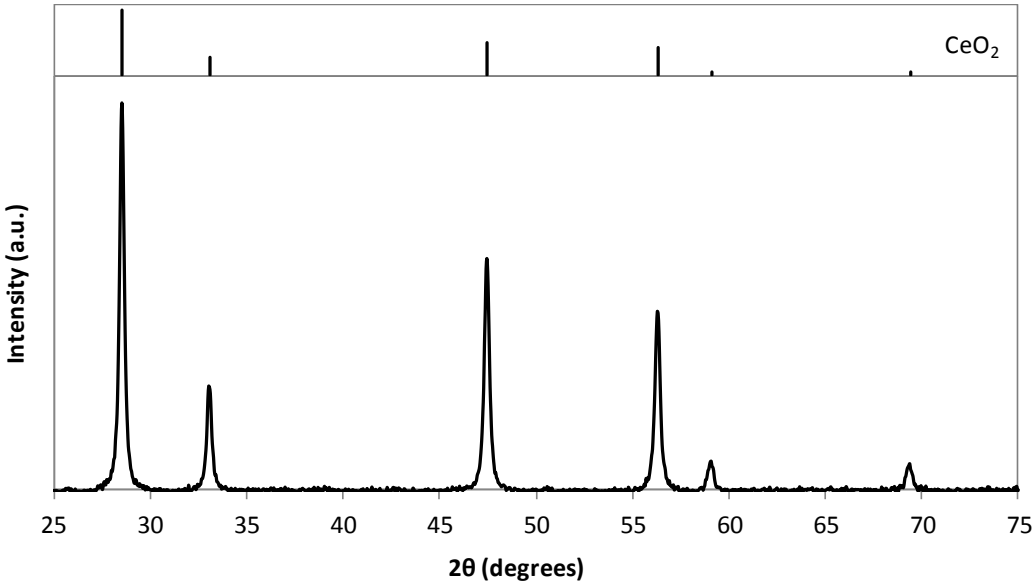

Figure 3.9: X-ray diffraction pattern for 10Gd with inset showing CeO_2 reflection.

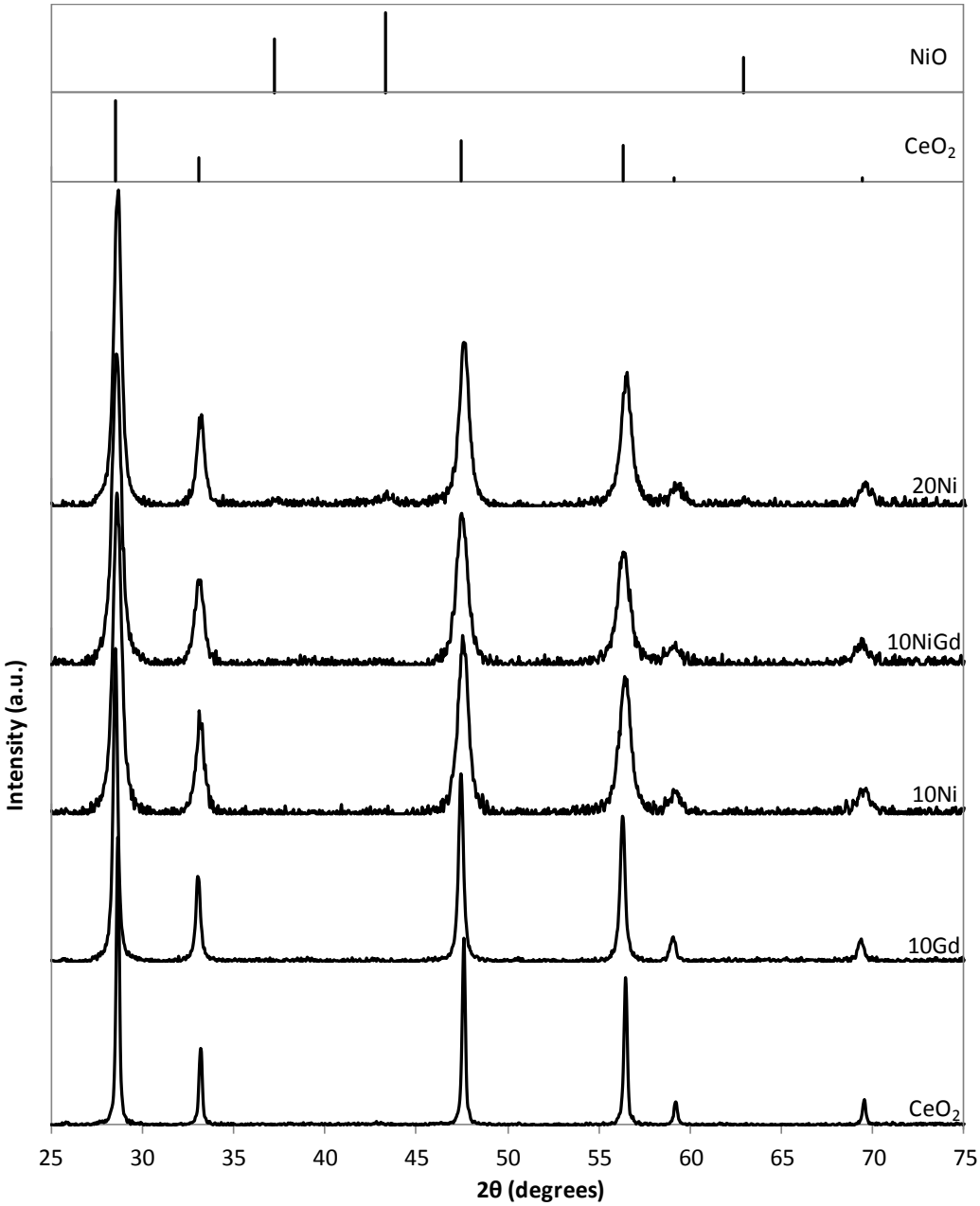

Figure 3.10: Overlay of all X-ray diffraction patterns for spray dried materials with inset showing CeO_2 (JCPDS 00-004-0593) and NiO (JCPDS 00-047-1049) reflections.

Chapter 4

CATALYTIC PERFORMANCE

4.1 Thermodynamic Equilibrium of Reactions

In section 1.1.4, several potential fuel reforming reactions were discussed including steam reforming, partial oxidation reforming, CO_2 reforming, and autothermal reforming. Because we have experience with partial oxidation of methane [74,75] and have optimized the conditions for the reaction, we chose to first test catalysts with POM and compare their performance to prior work. Because steam reforming is currently the most important reforming reaction for SOFCs, steam reforming of methane was also explored and the reactor setup was optimized as described in section 2.1.4 to accommodate steam.

The performance of a reforming reaction can be enhanced by catalysts, but is limited by equilibrium thermodynamics of the reaction, which describe the maximum attainable limits of parameters such as conversion and selectivity. Thermodynamic analysis of a reaction involves the calculation of equilibrium conditions for all reactant and product gas molecules present, at certain reactor conditions such as temperature and pressure. The most commonly used method involves minimization of the Gibbs free energy since thermodynamic equilibrium is achieved at this minimum [76]. From these calculations it can be determined which reactions are thermodynamically favorable at certain temperatures and pressures. The result also gives an understanding of the maximum attainable performance expected for a catalyst, and can be used as a reference.

4.2 Partial Oxidation of Methane

When synthesizing reforming catalysts for the SOFC, catalytic testing is important to determine activity for H_2 production. Testing catalytic behavior is also a type of characterization technique that can give insight into the properties of catalyst materials. The partial oxidation of methane reaction (equation 1.12) combines one mole of CH_4 with 0.5 moles of O_2 to form H_2 and CO. The complete combustion reaction (equation 1.13) can also occur when combining CH_4 and O_2 which results in the formation of CO_2 and H_2O. Catalysts were synthesized with spray drying and then tested for catalytic behavior in the ISRI RIG 150 reactor. 100 mg of catalyst powder was used for testing in a gas atmosphere of CH_4:O_2:He = 8:4:50 while ramping the temperature to 900 °C for the POM reaction. Conversions and selectivities were calculated from the output of the gas chromatograph as described in section 2.1.3. For a POM catalyst the most important parameters are the CH_4 conversion and CO selectivity which indicate activation of the POM reaction and production of the desired products of H_2 and CO. The O_2 conversion is also important because it determines whether the gas atmosphere in the reactor is oxidizing or reducing.

4.2.1 Initial Experiments

The thermodynamic equilibrium data for the POM reaction can be calculated using FactSage software by Thermfact Inc. and GTT Technologies, and is presented in Figure 4.1, and shown in reference [14]. The graph in Figure 4.1 reveals the theoretical reforming potential with POM in terms of CH_4 and O_2

conversion, and in terms of selectivity to the products of the POM reaction, H_2 and CO, and the complete combustion products of CO_2 and H_2O. From this calculation we see that at 550°C the CH_4 conversion, CO selectivity, and CO_2 selectivity are all approximately 50% which can be compared to catalysts as a measure of performance.

POM experiments were first run on the reactor tube with no catalyst, and on plain CeO_2 to establish a reference. Figure 4.2 shows a plot of percent conversion of CH_4 and O_2, and selectivity towards CO_2 and CO, versus temperature for the gas phase reaction occurring in the empty reactor tube. No catalytic conversion of CH_4 occurs until 630°C. At this point, CO_2 is produced which indicates that the complete combustion reaction has begun. At 730°C, CO formation begins, indicating that the POM reaction has activated. The presence of both CO_2 and CO reveals that both reactions occur simultaneously. CO production then increases slowly with increasing temperature. O_2 conversion reaches a maximum value of 40% at 900°C. CH_4 conversion reaches a max value of 24% at 900°C with a selectivity of 95% towards CO.

POM results for plain CeO_2 are shown in Figure 4.3. The conversions of CH_4 and O_2 begin at 465°C with the production of CO_2. O_2 is consumed more readily than CH_4 and reaches 99% conversion at 800°C. CO is not formed until 780°C where the amount produced increases slowly with temperature. The max CH_4 conversion is 32%, achieved at 900°C where the max CO selectivity is only 33%. CeO_2 promotes the reaction as compared to the reactor tube with no catalyst present, but it favors the complete oxidation reaction with a CO_2 selectivity of

67% at the maximum temperature of 900°C. The catalytic performance was also measured on the CeO_2 catalyst while the temperature was ramped back down from 900°C to 600°C to monitor its behavior after activation. In this case, the ramp down follows a pathway nearly identical to the ramp up as indicated by Figure 4.3 where both the ramp up and down are shown simultaneously on the plot.

4.2.2 Doped Materials

Figure 4.4 shows catalytic data for the first spray dried sample, 10Ni. The sample shows relatively poor catalytic performance. CH_4 conversion begins at 390°C with the production of CO_2. CO is not produced until after O_2 conversion reaches 100%, at 810°C. The CO selectivity slowly increases until its maximum value of 80% at 900°C. CH_4 conversion reaches a maximum value of 68%. A temperature ramp down to 600°C of the catalyst is also shown in Figure 4.4. The ramp down behavior is poor, similar to that of pure CeO_2 where it follows its original activation pathway. However, the catalytic activity is slightly worse on the ramp down than the ramp up. Overall, the material follows a pattern of activation similar to pure CeO_2 with a slow initiation of CO production. It does however reach higher values of CH_4 conversion and CO selectivity than pure CeO_2 indicating that some Ni metal must be present and active. The catalytic data is a clue into the properties of the doped material, revealing that it behaves differently than a supported metal catalyst of similar composition. Appendix A shows the data for a Ni/CeO_2 supported metal catalyst containing 7 at.% Ni. It

contains slightly less Ni than the doped catalyst but performs better, indicating that interaction between Ni and ceria has had a negative impact on the reforming in the 10Ni catalyst.

The 20Ni sample results are shown in Figure 4.5. This material, in contrast to the 10Ni catalyst, exhibits very good performance. CH_4 conversion and CO_2 production begin at 375°C. At 780°C after O_2 conversion has reached 100%, a sudden increase in CH_4 conversion up to 97% along with CO formation with a selectivity of 95% is witnessed, indicating that the catalyst has become activated for POM. At 900°C, CH_4 conversion reaches 99% while CO selectivity reaches 97%. A ramp down to 600°C was also performed on this catalyst with results shown in Figure 4.5. The graph reveals that after the catalyst has been activated at 900°C, it remains active during the ramp down and follows the thermodynamic limit of the POM reaction (Figure 4.1). For catalysts of Ni metal supported on inert silica (SiO_2), this type of behavior has been explained based on structure and phase transformations. As the reaction proceeds, Ni metal is initially oxidized to NiO by O_2 in the gas mixture. Once O_2 is depleted and the environment becomes reducing, Ni metal forms. O_2 entering the reactor is rapidly converted so the environment remains reducing, and as temperature is decreased, the Ni metal remains active [74]. Details for a Ni/SiO_2 catalyst are shown in Appendix A. The catalytic behavior of this catalyst is very similar to that of our 20Ni sample. This indicates that the 20Ni sample must contain enough active Ni on the surface to overcome effects of the CeO_2 support and behave as pure Ni would.

The good performance of the 20Ni sample and similarity to Ni/SiO_2 indicates that there is a significant amount of Ni on the surface to participate in the reaction. To explore interaction between Ni and CeO_2 in regards to catalyst deactivation, the catalyst was thermally aged with the POM reaction. It is optimum to test catalysts is for long periods of time at their operating temperature to determine their lifetime, but time and resources constrain how long tests can be run. To overcome this we wanted to apply accelerated aging to the 20Ni catalyst with high temperature to simulate long term operation at a lower temperature as used in intermediate temperature SOFCs. Sintering of CeO_2 increases particle size, reducing surface area and active sites for the reaction and is one source of loss of reforming potential. Coarsening of ceria particles is a thermally activated process that depends on diffusion. Combining an Arrhenius equation for coarsening with equations for the effect of sintering time and temperature on particle size gives equation 4.1 which relates time intervals Δt_1 and Δt_2, temperatures T_1 and T_2, activation energy for the sintering process Q, and the ideal gas constant R [77].

$$\ln\left(\frac{\Delta t_1}{\Delta t_2}\right) = \frac{Q}{R}\left(\frac{1}{T_2} - \frac{1}{T_1}\right) \tag{4.1}$$

For equation 4.1, the activation energy for ceria sintering Q, is required. This value is dependent on sintering behavior for a specific material which depends on particle size and shape. For CeO_2 nanoparticles with an average size of around 15nm, Q has been approximated as 325kJ/mol [78]. This activation energy has also been reported as 370kJ/mol for larger nanoparticles [79]. The activation energy of our material most likely falls somewhere in between these values based

on the CeO_2 particle size estimate of 98nm from XRD, but the lower value of 325kJ/mol was chosen to give a more conservative estimate of aging time. Using equation 4.1, we can define a temperature T_2 and a time Δt_2 for accelerated aging of the sample at the operating temperature 600°C (T_1). We chose to age the material at T_2 = 700°C for 13 hours which is equivalent to running the catalyst at 600°C for 1300 hours based on equation 4.1. The material was aged at 700°C after activation at 800°C with results in Figure 4.6. It is observed that at 800°C the CH_4 conversion has reached 99% with CO selectivity of 97%. After ramping the temperature down to 700°C, the CH_4 conversion stabilized to 92% with a CO selectivity that was also 92%. The entire reaction including activation lasted 16 hours, and the temperature held at 700°C for 13 hours. No decrease in performance was seen during this time.

Next, the 10NiGd sample was tested with results presented in Figure 4.7. Although this material had the same Ni content as 10Ni, it was more active. In this case, CH_4 conversion and CO_2 production begin at 280°C. Oxygen conversion reaches 99% at 650°C. A rapid increase in CO production is seen at 760°C, followed by a slight drop. Eventually CO selectivity reaches 91% and CH_4 conversion reaches 83% at 900°C. For this catalyst, there is a 100°C delay between O_2 conversion reaching its maximum value and activation of POM. This would indicate that the catalyst is a very strong oxidation catalyst, with all of the oxygen available being converted to CO_2 through complete combustion at a much lower temperature than the 10Ni and 20Ni samples. This also suggests that the Ni

in the sample does not reduce to NiO immediately when the environment in the reactor becomes reducing.

For the 10NiGd catalyst the temperature was also ramped down after activation, revealing poor behavior that is slightly worse than during the ramp up. The 10NiGd catalyst seems to show a behavior intermediate between the 10Ni and 20Ni samples. To explore the effect of Gd in the sample and determine whether it enhances the reaction, a 10Gd sample was tested for POM. The sample showed enhancement of catalytic performance as compared to pure CeO_2. Figure 4.8 shows the results including a temperature ramp up and down where CH_4 conversion reached 50% at 900°C with a selectivity to CO of 70% and a general behavior very similar to CeO_2. It is not clear, however, whether this improvement is due to composition or a particle size/surface area effect. It was determined from XRD in section 3.2 that the particle size of 10Gd is smaller than that of CeO_2 which could mean that the greater amount of surface area in the 10Gd sample allows for more conversion of CH_4. One study has shown that the presence of Gd in CeO_2 enhances activity for steam reforming of ethane [80]. In this case 15% Gd was the optimum composition that exhibited a greater activity than pure CeO_2. However, in this work it was also demonstrated with XRD that crystallite size decreased with increasing Gd content. The 15% Gd catalyst had the smallest crystallite size and highest surface area. Our results are similar with 10Gd exhibiting a higher activity for POM but also having a smaller average crystallite size. In the case of the 10NiGd sample, the enhancement in performance over 10Ni could be due to Gd presence, or a smaller crystallite size. In this sample the

higher activity could also be due to the absence of Ni doping. Gd doping into CeO_2 may leave no room for Ni compared to 10Ni. The reasons for the difference between 10Ni and 10NiGd cannot be determined from the catalytic data alone.

When testing the doped catalysts it was unclear whether they should be pre-reduced before POM as a supported metal catalyst would be (Appendix A). Therefore for each catalyst one run was performed with the material reduced within the reactor at 400°C for 3 hours in a gas environment of 5% Ar/H_2, and one was performed without reduction. Pre-reduction did not make an impact in either of the 10 at.% Ni samples as evidenced by Figure 4.9. This figure shows two separate runs for 10NiGd, one with reduction and one without. It is seen that the runs are nearly identical, including the drop in CH_4 conversion and CO selectivity that occurs after activation. This drop was seen in 3 different runs of the sample consistently (Figures 4.7 and 4.9). We believe this is a result of strong interaction between Ni metal and CeO_2 and the effects of sintering of CeO_2 at 700°C. The drop could be caused by a sudden loss of surface area as CeO_2 sintering occurs. It is also interesting to note that the 10NiGd sample shows behavior that is very similar to the Ni/CeO_2 supported metal catalyst (Appendix A). Both samples reach 100% oxygen conversion well before CO production begins. They both also contain the drop in CH_4 conversion and CO selectivity after the initial activation. Pre-reduction was also performed on the 20Ni sample. The effect of the reduction was to lower the activation temperature to 700°C. After this point, the behavior followed the pathway of the non-reduced sample (Figure 4.5) identically.

4.3 Steam Reforming

The steam reforming reaction combines H_2O and CH_4 to produce H_2, CO, and CO_2 as discussed in section 1.1.4. We chose to use the stoichiometric steam to methane ratio of 1 to 1 given by equation 1.2 rather than use excess steam. Steam reforming tests were performed in the ISRI RIG 150 reactor modified to include a saturator and condenser as described in section 2.1.4. To incorporate steam into the gas mixture in the appropriate ratio, the saturator was heated to a temperature of 50°C with a heating jacket based on calculations from equation 2.3. 100 mg of catalyst powder was used for testing in a gas atmosphere of CH_4:H_2O:He = 8:8:50 while ramping the temperature to 900°C. Conversions and selectivities were calculated from the output of the gas chromatograph as described in section 2.1.3. Similar to POM, CH_4 conversion is the most important factor in determining catalyst performance. For steam reforming, however, there are several possible reactions that all produce hydrogen as described in section 1.1.4. The carbon in CH_4 will either be converted to CO or CO_2, both of which are concurrent with H_2 production.

4.3.1 Initial Experiments

Calculations of thermodynamic equilibrium for the steam reforming reaction can also be performed [81]. Results are displayed in terms of molar fraction of each gas present versus temperature. It is observed that the reforming potential is greater at lower temperatures for SR due to the absence of the complete combustion reaction present in POM.

To observe the gas phase reaction with no catalyst, the steam reforming reaction was first run on the empty reactor tube. The CH_4 conversion with no catalyst began at 700°C and reached only 4% at 900°C, so no graph is shown. With the small amount of CH_4 converted, both CO and CO_2 were formed. Plain ceria results are shown in Figure 4.10. Plain CeO_2 also shows poor behavior but is more effective than no catalyst. CO_2 production begins at 410°C and increases slowly until 900°C while CO production does not begin until 860°C. The maximum value of CH_4 conversion, obtained at 900°C, was 13%. At this point, selectivity to CO_2 was 34% and selectivity to CO was 66%. Plain CeO_2 functions worse during the SR reaction than it does for POM. It does however appear to also favor the production of CO_2 rather than CO.

4.3.2 Doped Materials

Because Ni is the active catalyst for both the POM and SR reactions, we expected that catalytic activity in SR would be similar to results shown for POM. Because 10Ni and 10NiGd were poor catalysts, only 20 Ni was tested. The 20Ni sample showed good catalytic performance during steam reforming as indicated by Figure 4.11. CO_2 formation occurred at 420°C which also means hydrogen production began. CO production began at 600°C. At 660°C there is was a sudden, rapid increase in the production of CO. At this point a large increase in the production of CO_2 was also seen, even though the selectivity to CO was higher. As temperature was increased beyond 660°C, CO production and selectivity increased while CO_2 formation decreased. CH_4 conversion increased

with temperature to a maximum value of 98% where CO selectivity was also 98% and CO_2 selectivity was 2%. A ramp down to 600°C was also performed in steam reforming, shown in Figure 4.9. Similarly to POM, the ramp down showed higher values of conversion and selectivity at lower temperatures. The activated catalyst showed behavior similar to the thermodynamic limit of the reaction [81] due to the presence of active Ni metal.

4.4 Summary

A summary of catalytic results for POM in terms of CH_4 conversion and CO selectivity is given by Table 4.1. In this table the CH_4 conversion and CO selectivity for each sample, as well as the thermodynamic limit, at 600°C,700°C,800°C, and 900°C are displayed. In this table the performance of each catalyst can be compared to the thermodynamic limit. For the ramp up, the performance of all catalysts is poor until activation after 700°C. 20Ni is the best catalyst and reaches the thermodynamic potential for the reaction while 10NiGd has the second best performance, followed by 10Ni, 10Gd, and finally CeO_2. For the ramp down, all catalysts followed their original, poor activation pathway except for 20Ni which followed the thermodynamic limit of the reaction closely. Overall, catalytic data for pure ceria revealed a poor performance for POM, but enhancement of the complete oxidation reaction. 10Gd, as compared to CeO_2, exhibited higher performance. 10Ni exhibited poor performance at lower temperatures, but activated at higher temperatures and achieved higher values of CH_4 conversion and CO selectivity than CeO_2 and 10Gd. 10NiGd showed

enhanced performance as compared to 10Ni at all temperatures. Finally, 20Ni exhibited the best performance.

The first point of interest in catalytic results is that 10Gd had enhanced performance as compared to pure CeO_2. However, the particle sizes of the two materials were 58nm and 98nm respectively and the higher CH_4 conversion reached by 10Gd could be the effect of a higher surface area. The catalytic results for 10Ni showed a performance worse than a Ni/CeO_2 catalyst with a lower Ni content of 7 at.%. The performance of 10Ni was also worse than 10NiGd which contained the same amount of Ni. In this case, the particle sizes of the two materials as measured by XRD were 27 nm for 10Ni and 22nm for 10NiGd. Therefore, it is unlikely that the performance difference is the result of a surface area difference. Although the original particle sizes for the two samples are similar, it is possible that the presence of dopants leads to different sintering behaviors during high temperature exposure in the reactor. When examining 10Ni and 10NiGd with TEM, it will be important to look for structural differences between the two that could cause this difference in performance. The 20Ni sample was the only material tested that was a strong reforming catalyst for POM. From XRD we know that this sample contains a separate NiO phase that is most likely the active phase. Accelerating aging of 20Ni showed stability during POM for 13 hours at 700°C, which is equivalent to 1300 hours at 600°C in terms of sintering of ceria.

Steam reforming of methane over pure ceria and 20Ni was also performed. It was shown that pure ceria performed much worse during steam

reforming than during POM. 20Ni, however, exhibited high activity for SR, similar to results for POM.

Table 4.1: Summary of catalytic performance for all samples tested with POM in terms of CH_4 conversion and CO selectivity.

	Temperature (°C)	Sample	CeO_2	10Gd	10Ni	20Ni	10NiGd	Thermodynamics
Ramp up	600	CH_4 Conv.	5.4	8.6	4.6	10.3	21.3	56.4
		CO Sel.	0.0	0.0	0.0	0.0	0.0	59.3
	700	CH_4 Conv.	21.4	22.0	17.5	21.6	24.2	77.9
		CO Sel.	0.0	3.9	0.0	0.0	0.0	86.1
	800	CH_4 Conv.	25.1	25.8	25.6	97.6	66.1	91.4
		CO Sel.	4.3	8.1	0.0	96.1	79.7	96.4
	900	CH_4 Conv.	32.1	50.7	68.8	98.8	83.2	96.9
		CO Sel.	32.9	69.8	81.9	96.9	91.9	99.0
Ramp down	800	CH_4 Conv.	25.0	24.7	23.7	96.2	29.5	91.4
		CO Sel.	3.1	4.7	4.6	94.5	20.3	96.4
	700	CH_4 Conv.	21.1	22.7	8.5	87.2	24.2	77.9
		CO Sel.	0.0	1.5	0.0	87.2	0.1	86.1
	600	CH_4 Conv.	7.2	10.8	3.6	53.8	18.4	56.4
		CO Sel.	0.0	0.0	0.0	58.1	0.0	59.3

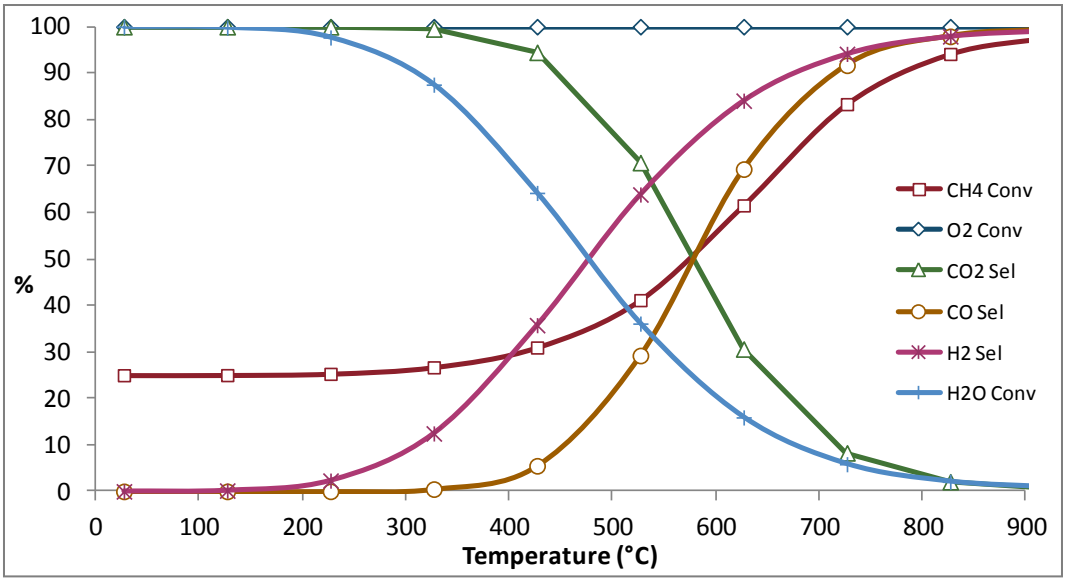

Figure 4.1: Thermodynamic data for the partial oxidation of methane reaction.

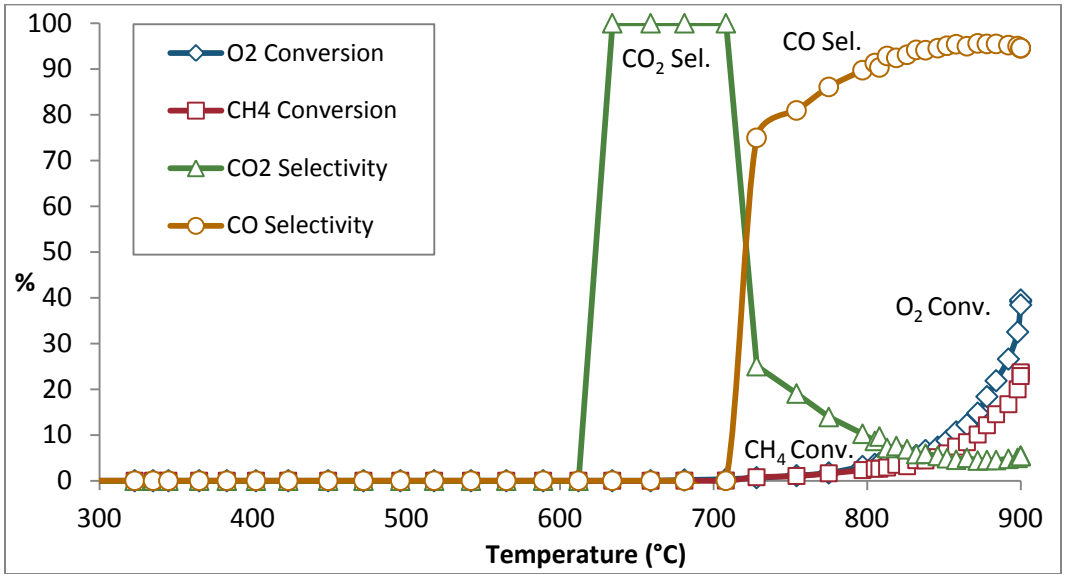

Figure 4.2: Plot of percent conversion of O_2 and CH_4, and selectivity for CO_2 and CO vs. temperature during POM reaction for no catalyst (empty reactor tube). Legend shows colors and symbols that will be used for these four parameters consistently.

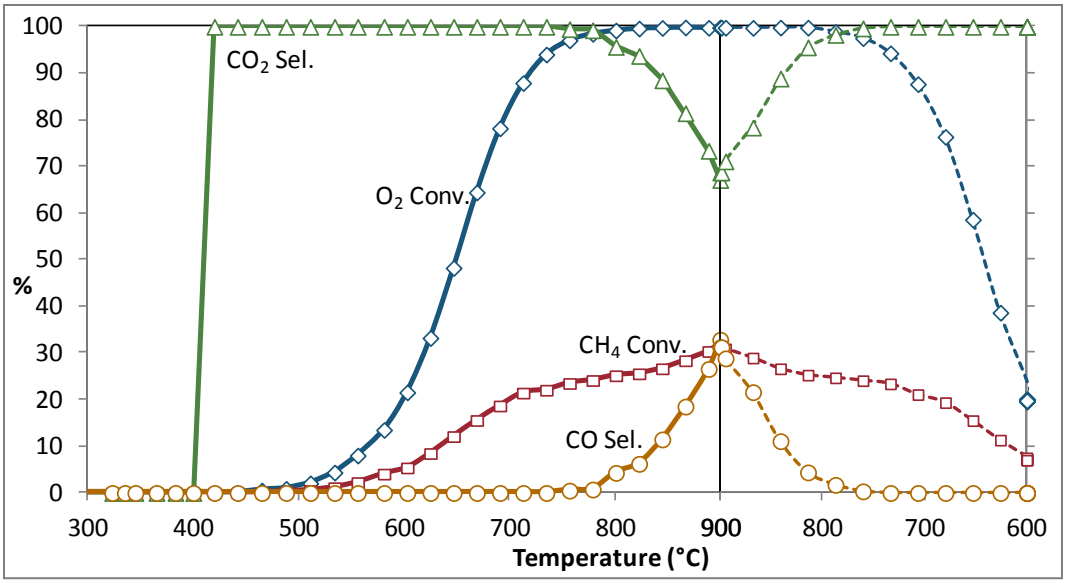

Figure 4.3: Plot of percent conversions and selectivities vs. temperature during POM reaction for plain ceria. Temperature ramp up is shown in solid line while ramp down is shown in dashed line.

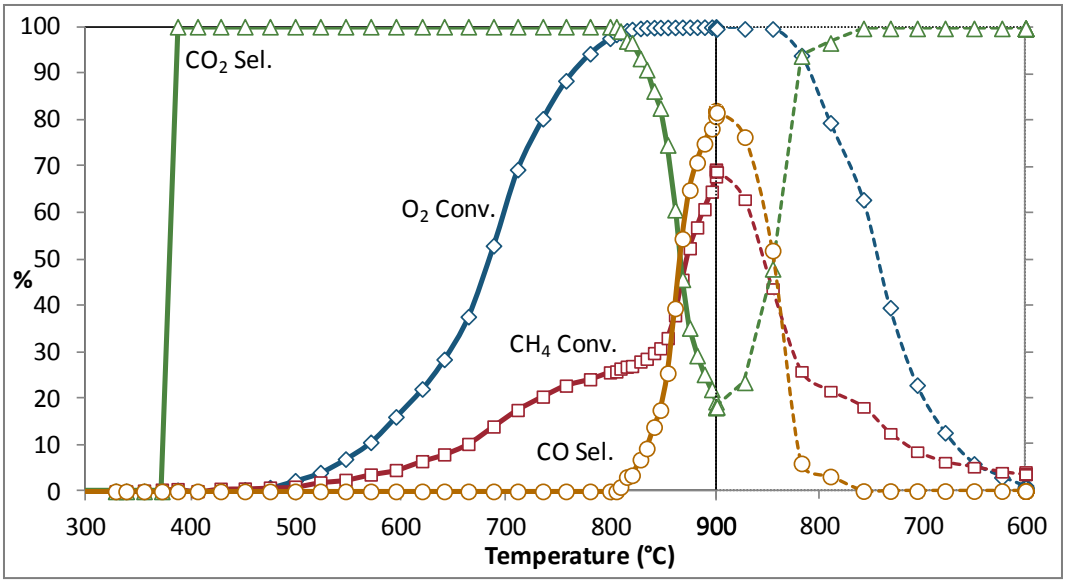

Figure 4.4: Plot of percent conversions and selectivities vs. temperature during POM reaction for 10Ni. Temperature ramp up (solid line) and ramp down (dashed line) are shown.

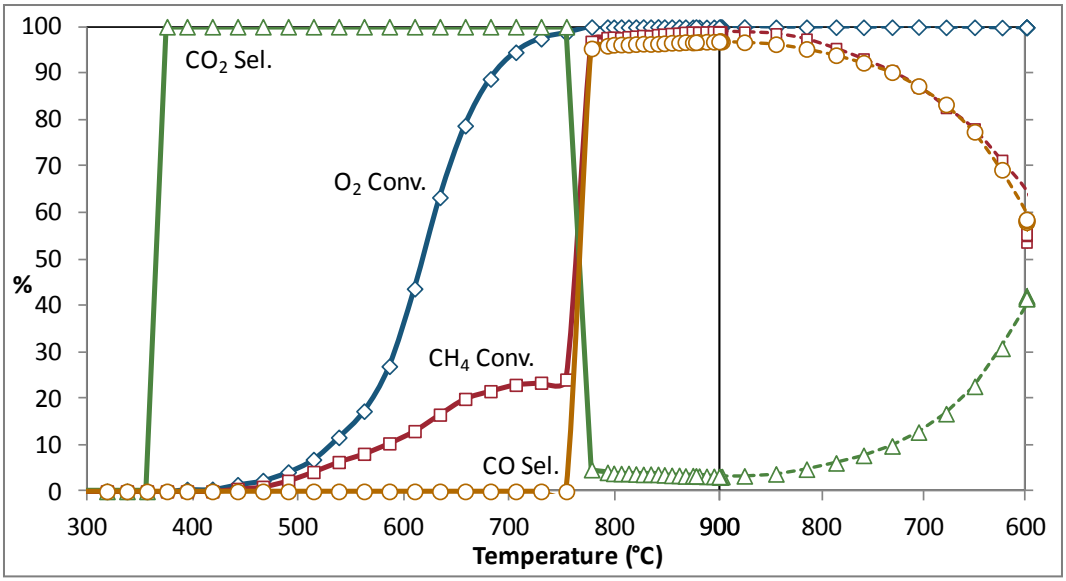

Figure 4.5: Plot of percent conversions and selectivities vs. temperature during POM reaction for 20Ni. Temperature ramp up (solid line) and ramp down (dashed line) are shown.

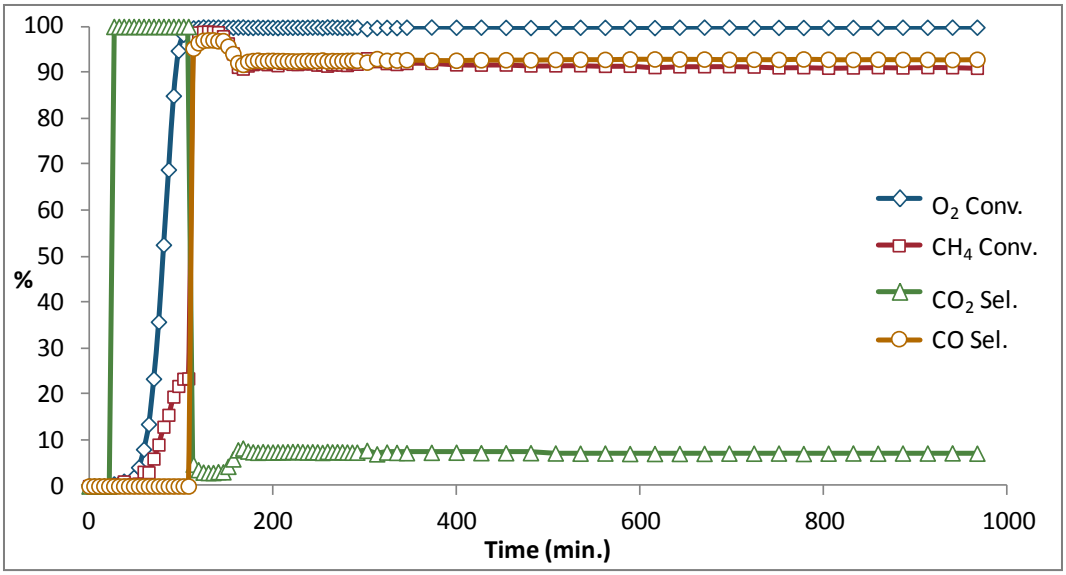

Figure 4.6: Catalyst aging graph showing percent conversions and selectivities vs. time during POM reaction for 20Ni.

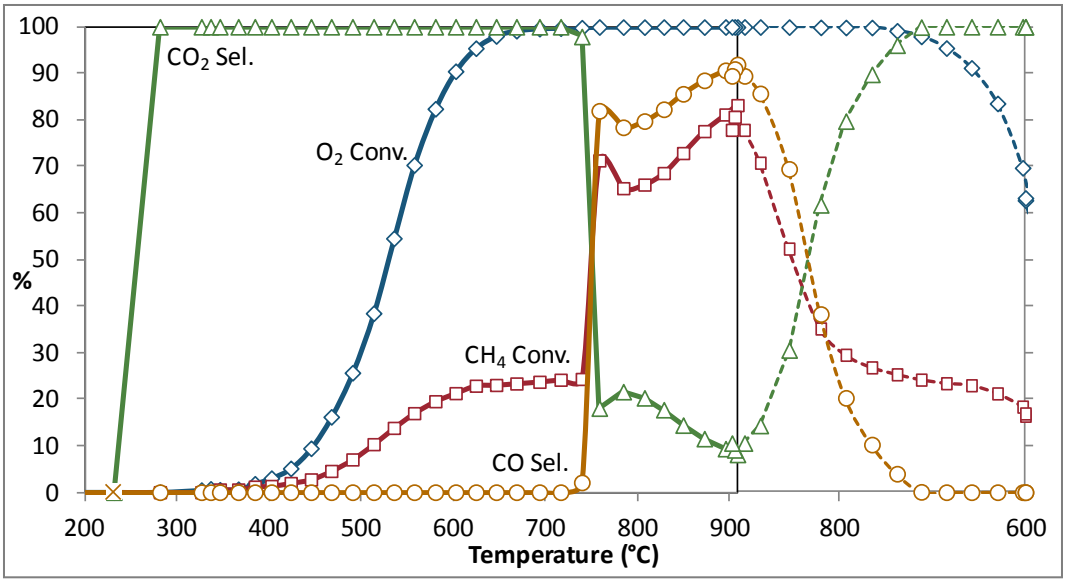

Figure 4.7: Plot of percent conversions and selectivities vs. temperature during POM reaction for 10NiGd showing temperature ramp up (solid line) and ramp down (dashed line).

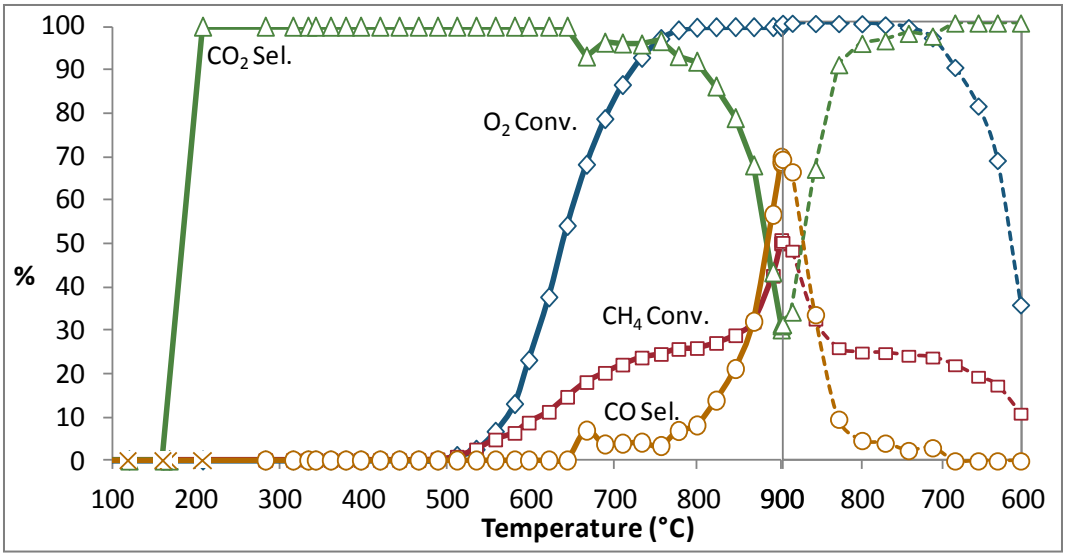

Figure 4.8: Plot of percent conversions and selectivities vs. temperature during POM reaction for 10Gd showing temperature ramp up (solid line) and ramp down (dashed line).

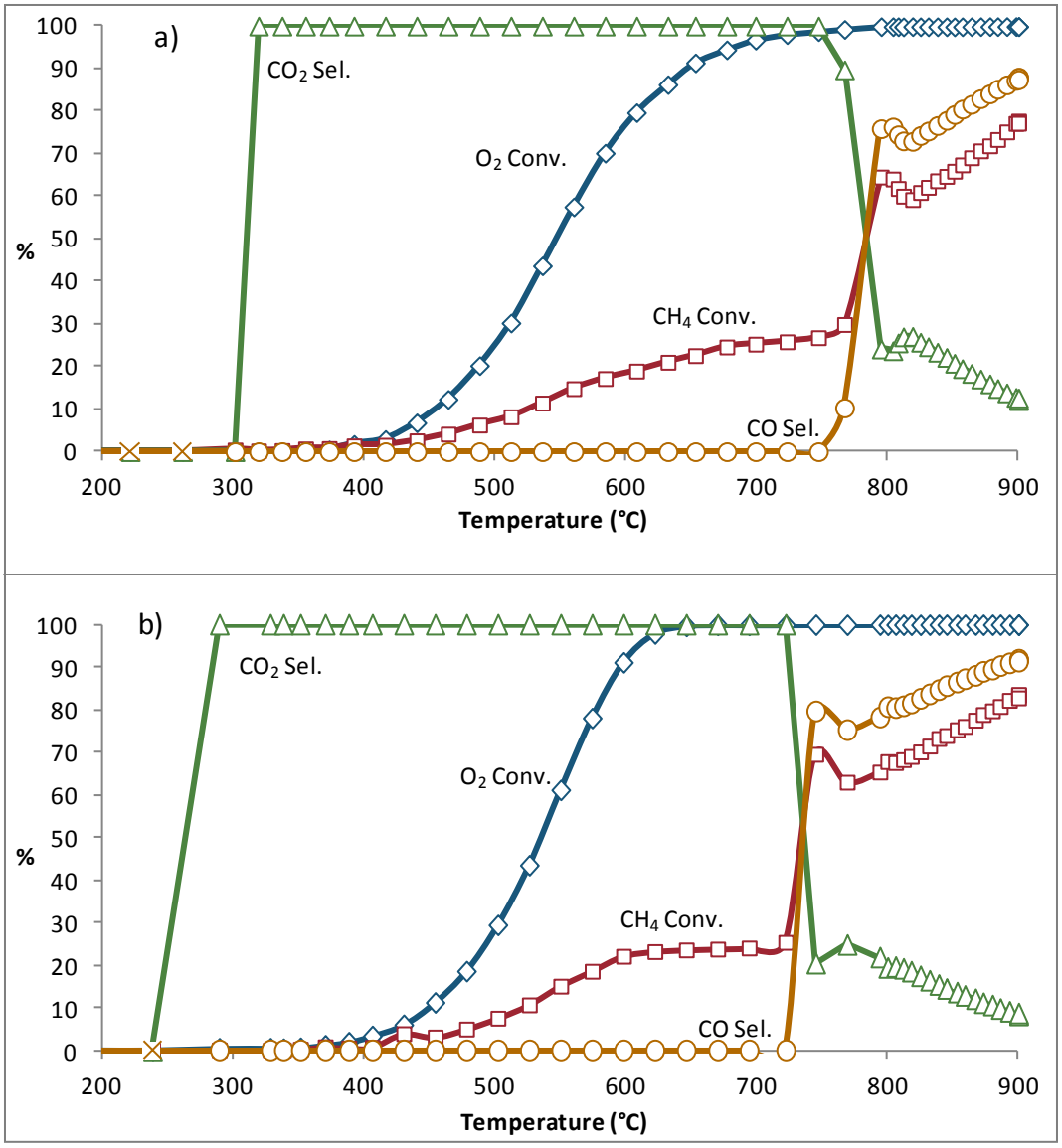

Figure 4.9: Results for 10NiGd during POM for a) reduced sample vs. b) not reduced sample.

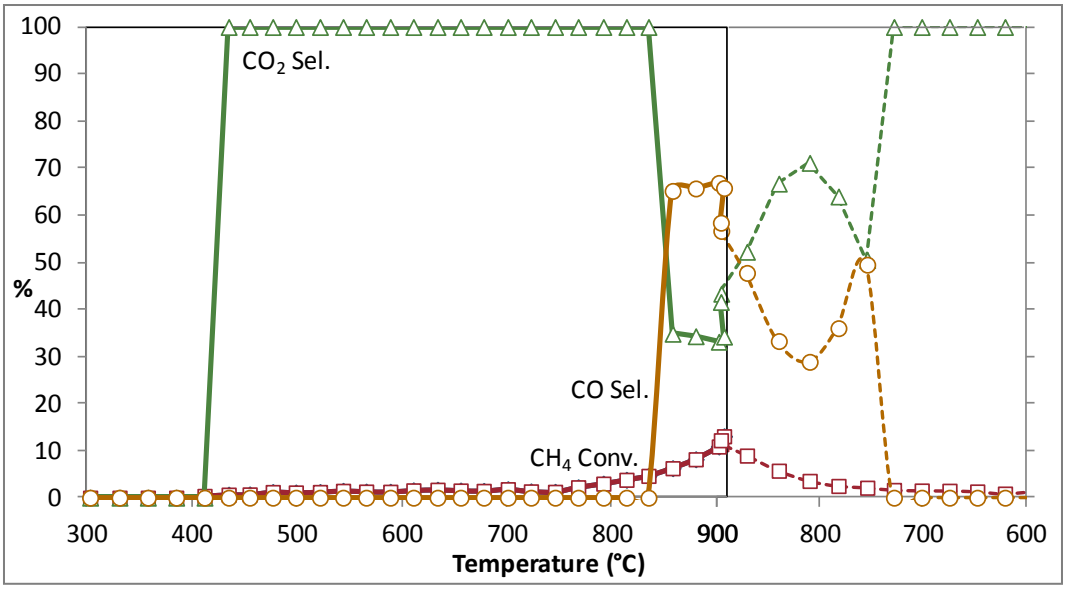

Figure 4.10: Plot of CH_4 percent conversion and CO_2 and CO selectivities vs. temperature during SR reaction for pure CeO_2. Temperature ramp up is indicated by a solid line and ramp down by a dashed line.

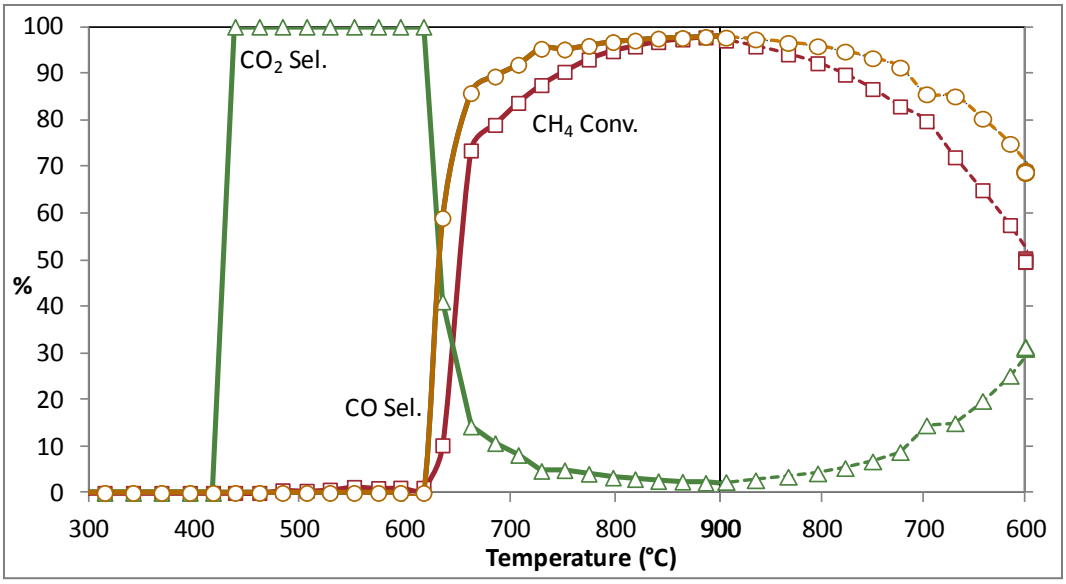

Figure 4.11: Plot of CH_4 percent conversion and CO_2 and CO selectivities vs. temperature during SR reaction for 20Ni. Temperature ramp up (solid line) and ramp down (dashed line) are shown.

Chapter 5

NANOCHARACTERIZATION

5.1 Introduction

XRD results in chapter 3 and catalyst performance data from chapter 4 gave some insight into the properties of the spray dried Ni/CeO_2 materials. However, conclusions about Ni doping in CeO_2 and the relationship between structure and catalytic performance are also needed. Transmission electron microscopy offers many techniques that can be useful for analyzing nanocatalyst materials. Low magnification TEM images can be used to examine the overall structure of nanopowders and to obtain the particle size distribution. High resolution electron microscopy (HREM) is useful to examine the morphology of nanoparticles including crystallinity, surfaces, and defects. Spectroscopy including EDX and EELS can determine composition of materials on the nanoscale and provide elemental quantification. In the case of EELS, information on oxidation states of materials can also be obtained. *In-situ* environmental TEM is also a valuable tool that can be used to observe catalysts directly in gas environments found in the reactor. In this chapter all of these techniques are employed in attempt to understand the interaction between Ni, Gd, and CeO_2, and how the structure of the catalysts affects their fuel reforming potential.

5.1.1 TEM Image Analysis Process

Identification of material crystal structure can be gained from HREM through measurement of lattice spacings in an image. Interference between

diffracted beams and the primary beam results in a phase contrast image where periodicity of a crystal is represented by an interference pattern in the form of lattice fringes. The Fourier transform can be used to express a signal such as the phase contrast image intensity as a sum of different frequencies present. The fast Fourier transform (FFT) algorithm can be used to transform any spatial frequency in the image to a set of spots in reciprocal space from which the distance from the center to the spot corresponds to the inverse of the spacing between lattice fringes. For this work HREM image analysis was performed using FFTs in Gatan Digital Micrograph.

5.1.2 EELS Overlap Correction

For analysis of electron energy loss spectra the Ce M_{45}, Ni L_{23}, and Gd M_{45} signals were used. When quantifying elements present in a sample we must account for any overlap in the signals from these edges. First, overlap of the Ni L and Ce M edges which occur at 855eV and 883eV respectively must be corrected. Since the Ni L edge occurs directly before the Ce M edge, the Ce integrated intensity over a certain energy range will contain a Ni contribution which must be removed. To do this, a standard NiO spectrum was used to calculate a correction factor α_{NiCe}. Figure 5.1a shows this spectrum and the integrated intensities under the Ni L edge used to calculate α_{NiCe}. Equation 5.1 shows the calculation of α_{NiCe} where I_{Ni} is the integrated intensity of the Ni L_{23} peaks over a 30 eV window, and I_{Ni_Ce} is the integrated intensity of the Ni L_{23} signal under the ceria energy window of 50eV. The ceria signals measured for unknown samples containing Ni and Ce

can then be adjusted using this correction factor and the measured Ni signal as shown in equation 5.2. For all analysis an energy window of 100eV before the Ni signal was used as the background for subtraction.

$$\alpha_{NiCe} = \frac{I_{Ni\_Ce}}{I_{Ni}} = 1.81 \tag{5.1}$$

$$I_{Ce}\, corrected = I_{Ce} - \alpha_{NiCe} * I_{Ni} \tag{5.2}$$

For Gd containing samples, overlap of the Gd M_{45} signal with the Ce M_3 edge also occurs at 1185 eV. To correct this we followed a similar process where a CeO_2 spectrum was used to compare the intensity of the Ce M_{45} peaks to the intensity of the Ce M_3 peak integrated over the Gd energy window of 60 eV. Figure 5.1b shows the standard CeO_2 spectrum, the energy windows used for measurements, and the integrated intensities. A second correction factor α_{CeGd} was calculated as shown in equation 5.3 where I_{Ce} is the integrated intensity of the Ce M_{45} peaks over an energy window of 50 eV and I_{Ce_Gd} is the integrated intensity of the Ce M_3 peak over an energy window of 60 eV. The Gd signal can then be corrected as shown in equation 5.4.

$$\alpha_{CeGd} = \frac{I_{Ce\_Gd}}{I_{Ce}} = 0.08 \tag{5.3}$$

$$I_{Gd}\, corrected = I_{Gd} - \alpha_{CeGd} * I_{Ce} \tag{5.4}$$

Figure 5.1c shows an EELS spectrum for 10NiGd which contains Ce, Ni, and Gd. The standard energy windows used for quantification are shown along with the colored regions of integrated edge intensities after background subtraction. Both of the corrections described above in equations 5.2 and 5.4 can be used to correct first the Ce intensity, and second the Gd intensity.

5.1.3 EDX Quantification Procedure

In order to determine Ni content in doped samples, spatially resolved EDX was employed. Due to the poor catalytic behavior of the 10Ni and 10NiGd samples it was necessary to ensure that Ni was present in the samples in the amount desired. To quantify EDX results for the doped materials a standard sample was needed to use for quantification with the k-factor method described in section 2.2.4. The standard sample used was composed of nitrate precursors dissolved in ethanol. The first sample was a 50% Ni 50% Ce standard. It was made using the same calculations as for synthesis with spray drying where a molar ratio of Ni/Ce was used to determine the needed amount of nitrate salts. The two precursors were then dissolved in ethanol and sonicated for 30 minutes to ensure a uniform solution. The solution was suspended onto a holey carbon TEM grid and EDX was performed over a number of sample regions. Integrated intensities of the Ce L and Ni K peaks were found after background subtraction and then the known composition of 50/50 was used to calculate a k-factor for the specific microscope and detector conditions. Figure 5.2 shows a plot of intensity ratios for Ce/Ni versus the number of spectra, revealing very little spread in the data. In this case, the k-factor for Ce/Ni was 2.33±0.03, determined from 18 different spectra. A similar procedure was followed for a standard sample of Ce/Gd. The k-factor in this case was 0.092±0.02. Using these standards and peak intensities the composition for unknown samples of Ni/Ce/Gd can be calculated.

5.2 Microscopy of Starting Materials

5.2.1 Imaging and EDX Analysis

Imaging and EDX analysis was performed on all spray dried samples using the JEOL 2010F microscope. The structure of pure spray dried CeO_2 was examined first. It was useful to look at the structure of pure ceria to establish a reference and recognize differences in the doped Ni materials. Figure 5.3 shows a low magnification image of a CeO_2 cluster and a high resolution image of a particle. The overall structure is faceted and crystalline with lattice spacings matching the CeO_2 fluorite crystal structure (CeO_2 111 = 3.12Å, 200 = 2.71 Å, 220 =1.91 Å from JCPDS 00-004-0593). The most common nanoparticle surfaces observed were the CeO_2 (111) and (200) facets. The structure of Ni/CeO_2 supported metal catalysts can also be examined to determine differences as compared to spray dried samples. These results show CeO_2 particles with similar appearance to pure ceria, and small Ni particles dispersed over the surface. Results are detailed in Appendix A.

After examining reference CeO_2 samples, the structure and composition of Ni doped samples were explored. Imaging and EDX were performed over clusters and nanoparticles of 10Ni, 20Ni, and 10NiGd. Analysis was first performed on the 10Ni sample to examine its microstructure and determine if there was a distinguishable Ni presence. Images revealed that the material contained nanoparticles with an appearance similar to pure CeO_2 with no obvious, separate Ni phase. EDX analysis was performed to determine the location of Ni in samples. Images were taken of clusters and particles in the sample, and EDX

spectra were collected over these areas. The quantification procedure described in section 5.1.3 was then performed to determine Ni content. Figure 5.4 shows results for a 10Ni cluster and for two particles within the cluster. Quantification determined that cluster shown in Figure 5.4a contained 11.0 at.% Ni in total. The particle in Figure 5.4b had little to no Ni present with a result of 2.0 at.% Ni, and the particle in Figure 5.4c had a higher Ni content of 4.3 at.% Ni. The particle containing less Ni appeared more faceted and crystalline while the 4.3 at.% particle was defective and rounded. Both particles contained lattice fringes matching the CeO_2 structure. Overall, EDX over multiple clusters in the 10Ni sample showed a presence of between 6.3 at.% and 15.3 at.% Ni. The average composition obtained for 6 clusters was 9.5 ± 3.4 at.% Ni so it can determined that the correct amount of Ni is present in the sample.

Imaging and EDX analysis was also performed on the 20Ni sample. Similar to 10Ni, TEM imaging of the sample did not reveal any obvious Ni presence, and the sample appeared similar to CeO_2. Figure 5.5 shows one cluster from this sample and the EDX spectrum for the cluster revealing 26.6 at.% Ni. Composition for 20Ni varied from 12.9 at.% to 36.0 at.% Ni and the average composition was 22.7 ± 9.8 at.% Ni for 6 clusters. For the 20Ni sample there was definite heterogeneity in Ni content between clusters, but on average the correct amount of Ni was present in the sample. This heterogeneity is most likely caused by the segregated NiO phase present in the 20Ni sample. Due to the small regions sampled when analyzing clusters with EDX, some regions may have more of these NiO particles than others.

Finally, the 10NiGd sample was imaged and analyzed with EDX. Results for one cluster of the 10NiGd sample are shown in Figure 5.6. The region contained 10.3 at.% Ni and 12.9 at.% Gd. Gd content varied from 10.0 at.% to 13.6 at.% while Ni content varied from 7.0 at.% to 12.0 at.%. For 6 clusters the average composition was 9.6 ± 1.7 at.% Ni and 12.0 ± 1.2 at.% Gd. For the 10NiGd sample both Ni and Gd were present in the desired amount. In this case, the heterogeneity of Ni between clusters was less extreme than for 10Ni or 20Ni. To further examine Ni heterogeneity in the doped Ni samples, 10Gd was analyzed with EDX. For 6 clusters, the average composition was 11.4 ± 1.4 at.% Ni, a result with similar standard deviation to those for 10NiGd.

Using the low magnification images obtained for all three samples, average particle size in each sample can be determined and compared to results from XRD. These values can also be compared to particle size in each sample after the catalytic reaction to determine the extent of sintering after high temperature exposure. For each sample the sizes of around 100 particles were measured to determine an average. Particle size results were 20 nm, 25nm, and 19nm for 10Ni, 20Ni, and 10NiGd respectively. These values were similar, but consistently smaller than results for crystallite size from XRD in Table 3.2 which were 26 nm, 35 nm, and 22 nm, respectively.

Overall, EDX results for 10Ni, 20Ni, and 10NiGd demonstrated that, on average, Ni and Gd were contained in the samples in the desired amounts. Low magnification and HREM imaging of the samples did not reveal an obvious Ni phase as apparent in supported metal catalysts. EDX performed over particles of

the 10Ni sample showed that Ni was present in particles, but other techniques were needed to localize the Ni and determine if Ni doping occurred.

5.2.2 STEM EELS Results

After determining that Ni content in the samples was correct, attempts were made to more precisely locate Ni. STEM EELS line scans were performed using the JEOL 2010F microscope to determine the general behavior of Ni. Energy loss spectra were corrected using the procedure described in section 5.1.2. For the 10Ni sample, Ni rich domains were located in several areas while in other regions no Ni was present. Figure 5.7 shows a STEM ADF image and a line scan profile where energy loss spectra were collected along the line. The Ce and Ni signals in the spectra were analyzed and a plot of signal intensity versus line position was obtained. From Figure 5.7 it is observed that the line profile of the Ni does not follow that of Ce, but rather a small enhancement in the Ni is seen in a specific spot over the CeO_2 particle. This indicates that Ni content in the 10Ni sample is heterogeneous and Ni is not evenly dispersed through the CeO_2 particles as expected for a solid solution. For this sample, 12 line scans were performed. Out of 12 line scans, 7 showed Ni localized in domains similar to that shown in Figure 5.7. 4 out of 12 line scans showed no nickel signal anywhere along the line. Only 1 case out of 12 showed what appeared to be a surface coating of Ni on CeO_2.

EELS line scans were also performed on the 10NiGd sample. Figure 5.8 shows a line scan profile over a STEM ADF image, and the corresponding line

profiles for Ni, Gd, and Ce signal intensities versus position. For 10NiGd, Gd presence in samples was consistent with the CeO_2 signal while Ni appeared to be heterogeneous. It was seen that Gd followed roughly the same pathway as Ce, indicating Gd doping. Ni, however, was not distributed in the same manner as Ce or Gd. Again it was seen that there were localized areas where the Ni content was higher. In this case there was a low Ni content across the entire particle but the profile did not match that of Ce and Gd. HREM images from the 10NiGd sample, as shown in Figure 5.9, show that the structure of many particles was similar to that of pure CeO_2 with corresponding lattice fringes. EELS over this region revealed the presence of Ce and Gd with a low Ni signal.

For the 20Ni sample, EELS revealed similar heterogeneity in Ni content. Results were similar to the 10Ni samples where some particles appeared to be pure CeO_2 with little to no Ni presence, while some had localized Ni domains. In this sample it was also found that there was a separate NiO phase present in the form of nanoparticles. Figure 5.10 reveals a sample area with a CeO_2 crystalline particle next to a large NiO particle as revealed by EELS. These results are consistent with XRD results for the 20Ni sample where a distinguishable, crystalline NiO phase is detected.

Finally, EELS elemental mapping was performed using the JEOL ARM 200F on the 10Ni sample to further identify Ni location in low content areas. Energy loss spectra were again corrected using the procedure described in section 5.1.2. Similar Ni distribution results to those found with line scans were witnessed. Some regions exhibited Ni spread over sample in many small domains.

Other areas showed larger, more particle-like regions of Ni. Figure 5.11 shows a STEM ADF image of 10Ni and the region mapped by EELS. Analysis of spectra over this region gave the colored map shown in the Figure 5.11 where the Ce EELS signal is colored in blue and the Ni signal is colored in red. One energy loss spectrum over a region containing both Ce and Ni is also shown. From this map it was witnessed that Ni was not uniformly distributed in CeO_2 as in a solid solution, but was scattered into small Ni domains. These results could point to Ni in a phase separate from CeO_2 in the form of small particles, or, interaction between Ni and CeO_2 in specific locations through doping or the formation of a new phase.

5.3 Microscopy of Spent Catalysts

To explore how the catalytic reactions affect materials they can be examined with TEM after the reaction has been performed. Pure CeO_2 was first examined to view how its structure changed with the partial oxidation and steam reforming reactions. This analysis can help identify in spent Ni doped materials which structural changes are dependent on Ni and those which are from properties of CeO_2. Figure 5.12 shows a cluster and particle of CeO_2 after the POM reaction. Several structural changes have occurred. From 5.12a it is seen that the material appears less crystalline and faceted. The HREM image of Figure 5.12b shows that the particle has rounded with the formation of steps on the surface. Similar results were seen in ceria examined after SR.

The 10Ni, 20Ni, and 10NiGd catalysts were also analyzed after the POM and SR reactions. HREM images for all samples revealed an unstable image contrast. No segregated Ni was located in the 10Ni sample or the 10NiGd sample. Figure 5.13a shows a low magnification image of the 10Ni sample showing that the material is rounded, sintered, and contains a mottled contrast. The grains of the 20Ni sample had a similar appearance as 10Ni, shown in Figure 5.13b. HREM imaging of the spent 20Ni catalyst shows that there is also a Ni phase on the surface of CeO_2 particles. Figure 5.14a shows the material after POM and Figure 5.14b shows the material after SR where crystalline Ni and NiO regions, determined by lattice spacing measurements, are observed on the surface attached to CeO_2. These particles are the active phase that led to the good performance of 20Ni as a catalyst.

Particle size analysis can also be performed on all samples after the reaction to determine the degree of sintering. Analysis of particles in low magnification images for each sample revealed particle sizes of 51 nm, 48 nm, and 37nm for the 10Ni, 20Ni, and 10NiGd samples respectively. Original particle sizes determined with TEM were 20 nm for 10Ni, 25nm for 20Ni, and 19nm for 10NiGd. From these results it appears that 10NiGd has coarsened less than 10Ni and 20Ni, which is consistent with XRD results for 10Gd which showed that Gd inhibited particle sintering. It is important for catalysis that samples maintain a smaller particle size and thus greater surface area for the reaction to occur. Sintering behavior is also important for synthesis of the anode material and coarsening behavior during SOFC operation. In this case after exposure to 900°C

the samples have sintered and roughly doubled their particle size. This increase in particle size did not cause any drop in the catalytic activity of the samples.

To further understand Ni content in the spent catalysts, STEM EELS elemental mapping was performed over particles after the POM reaction. For the 10Ni sample results are shown in Figure 5.15 where an EELS map over a STEM ADF image with Ce signal in blue and Ni signal in red, and one spectrum from the map, are shown. Similar to what was observed for EELS mapping of 10Ni before the reaction, localized regions of Ni were seen. Results before and after do not reveal any significant changes in sample structure.

For 10NiGd after the POM reaction, EELS mapping results are shown in Figures 5.16 and 5.17. It is noticed that there are also Ni rich regions in this sample. The maps of Figures 5.16 and 5.17 show Ce signal in blue, Gd signal in green, and Ni signal in red. In both cases Gd and Ce are mixed fairly consistently throughout samples, indicating Gd doping. In Figure 5.16 Ni is contained in what appears to be large NiO particle. In Figure 5.17, Ce and Gd are present in all areas containing Ni. The amount of Ni present is large, as indicated by the EELS spectrum shown. The maps give detailed spatial information about the location of Ni and confirm that the majority is not present in a solid solution. When coupled with the catalytic data, the most likely conclusion for the 10Ni and 10NiGd samples after the reaction is that most of the Ni has agglomerated and is spread over the surface of the Ni. This is because catalytic performance of 10Ni and 10NiGd was enhanced as compared to pure CeO_2 and 10Gd, meaning some Ni must be present on the surface.

EELS analysis for all Ni doped samples revealed the presence of small Ni domains. It is useful to examine the potential detectability of Ni with EELS. To determine the detectability limit, EELS and EDX spectra were simultaneously collected from the same sample region of 10Ni with STEM. The EDX results were quantified and then the Ni signal of the corresponding EELS spectrum was examined. It was found that that the energy loss spectrum of Figure 5.18a corresponds to 15.3 at.% Ni as confirmed by the quantification of the corresponding EDX spectrum in Figure 5.18b. The Ni peak of Figure 5.18a is very small so it is reasonable to assume that we could not detect low amounts of Ni dispersed in the samples with EELS. Analysis of the Ni signal as compared to the background fluctuations reveals that the signal is roughly 4 times larger than background noise. Therefore we could potentially detect a nickel signal that was 1/4 as large as the 15.3 at.% Ni signal. From this, an estimate of the lowest amount of Ni we can detect with EELS is 3.5 at.% Ni. The EELS results presented for all samples contained significantly larger EELS Ni peaks than those obtained for 15.3 at.% Ni, so most of the Ni in the samples appears to be concentrated in Ni rich domains. Due to diminished performance as compared to supported metal catalysts, and the detection limits of EELS, it is still possible that a very small amount of Ni has contributed to doping.

5.4 *In-situ* ETEM

In-situ electron microscopy can give valuable insight into a material's structure under gas atmospheres and high temperatures found in the reactor. In

order to further examine the Ni content and doping in the samples, *in-situ* TEM was performed in the Tecnai F-20 ETEM for the POM reaction to simulate the reactor environment and directly observe structural changes. The experiment was performed on the 20Ni sample to investigate both the segregated NiO phase and the possible presence of Ni doping in CeO_2 particles.

First, the sample was heated to and held at 150°C with no gas exposure to remove any contamination, and analyzed to determine the structure of the starting material. 0.75 Torr of CH_4+0.5O_2 was then introduced and the temperature was ramped to 600°C. This was performed to simulate the reactor conditions during the catalyst activation where both CH_4 and O_2 are present during ramp up until O_2 is fully consumed. The sample was held at 600°C for 1 hour in CH_4 and O_2 to stabilize and was then examined. In the reactor, after the O_2 is consumed, the gas environment is primarily CH_4 until the catalyst activates and produces CO. To determine the effect of a reducing CH_4 environment on the 20Ni sample, at 600°C, the gas was switched from CH_4+0.5O_2 to an environment of pure CH_4. The CH_4+0.5O_2 gas was pumped out of the microscope while the temperature remained at 600°C. CH_4 alone was then introduced. At this point, some residual O_2 could still be present from the previous experiment. This residual O_2 content, however, also exists in the reactor as O_2 conversion is never 100%. Therefore the CH_4+0.5 O_2 mixture was pumped out until the relative pressure of O_2 to CH_4 was the same as that in the RIG 150 reactor. For 1 Torr of CH_4 this value was $7x10^{-4}$ Torr based on O_2 content in the 20Ni reactor run. Once this value was reached, CH_4 was pumped into the system until 1 Torr was reached. The system was

allowed to stabilize for 1 hour, was examined, and was then held again for 4 more hours. After further examination the temperature was then increased to 700°C. After 1 hour at 700°C, the sample was imaged and electron energy loss spectra were collected. The temperature was maintained at 700°C for 3 more hours and periodically examined. The temperature was next ramped to 800°C and held for 30 minutes before analysis. Finally, the temperature was decreased down to 500°C and the sample was immediately analyzed.

Imaging of the sample at 150°C revealed the presence of NiO grains and CeO_2 grains, similar to images from *ex-situ* TEM as shown in Figure 5.10. No structural changes in the sample were witnessed at 600°C in CH_4+0.5O_2. When the gas atmosphere was switched to CH_4 at 600°C, however, the structure of the segregated NiO phase became porous and defective. The NiO was also unstable, moving and growing tube-like structures of NiO when exposed to the electron beam. Figure 5.19 shows one example of this where a large NiO particle grows several smaller NiO particles with the same orientation 5.19a-c show the evolution of these small NiO particles with time. Although the sample was held at 600°C in CH_4 for 5 hours, reduction of NiO to Ni did not occur. All data captured at this temperature, images and spectra from approximately 10 different regions, confirm that NiO is not reduced. Once the temperature was increased to 700°C in CH_4, reduction of NiO to Ni occurred. This is a result very different from prior work on Ni/SiO_2 where reduction of NiO to Ni occurred at 500°C in CH_4 [75].Clearly, strong interaction between the NiO and CeO_2 particles has inhibited reduction of NiO. Once the temperature was increased to 700°C, all regions once

associated with NiO became rounded Ni particles. Strong interaction between this Ni phase and CeO_2 occurred. Two instances of "decoration" of Ni by ceria are shown in Figure 5.20. After observing the behavior of the separate NiO phase in the 20Ni sample, we wanted to determine Ni presence in CeO_2 grains and whether Ni doping into CeO_2 had occurred. The goal was to reduce the CeO_2 to Ce_2O_3, inducing a structure change that would expel Ni from the lattice. The temperature was therefore increased to 800°C in CH_4. However, this temperature could not be maintained due to hot stage instabilities and only a few images were acquired, with one shown in Figure 5.21. At 800°C the sample has undergone considerable sintering. The structure of the material consists of large grains of ceria with Ni particles appearing on the surface. More instances of "decoration" of Ni by CeO_2 are seen and several large Ni particles, one reaching around 50 nm, can be seen over the CeO_2. The temperature was finally ramped down to 500°C. Curiously, the structure of the sample changed significantly. First, the ceria was reduced as determined by EELS over 8 different sample regions examined at 500°C. The M_4 and M_5 lines in EELS correspond to transitions from the $3d^{3/2}$ and $3d^{5/2}$ states to empty states in the 4f band. Figure 5.22 shows a spectrum collected at 500°C where the Ce M_{45} line intensity has reversed. This shows that the ceria has reduced because the intensity of the M_4 and M_5 peaks depends on the occupancy of the 4f band, which changes from 0 to 1 as Ce changes oxidation state from +4 to +3 [82,83]. EELS performed periodically during the experiment demonstrated that the CeO_2 was not reduced at any temperature other than 500°C. However the temperature may not have been held long enough at 800°C to observe the effects.

Reduction was most likely initiated at 800°C and maintained during ramp down to 500°C. The second observation at 500°C is that Ni particles are no longer observed and rather NiO has formed. The structure that the NiO has taken on is different than the starting NiO structure or that at 600°C. The most interesting 500°C result is detailed by Figure 5.23. In two sample regions it is seen that tiny particles have appeared on the surface of a larger CeO_2 particle. Figure 5.23b shows a particle with unidentified lattice spacings that are larger than CeO_2 fringes. This difference could be from structure change due to reduction of CeO_2 or the formation of O_2 vacancies. EELS over this region shows that CeO_2 is reduced. It also shows that Ni is present, leading us to believe that the small particles observed are Ni. The second area of Figure 5.23a shows spacings matching the 111 of CeO_2 as well as the small particles. It is possible that a small amount of Ni doping occurs in some CeO_2 particles and upon reduction, the Ni has come out of the lattice in these areas.

Figure 5.24 shows the progression of one sample region throughout the experiment with all of the changes in gas environment and temperature. Figure 5.24a shows the initial material at 150°C with no gas present. The lack of change in the material in CH_4 and O_2 is seen in Figure 5.24b. Figure 5.24 also shows the change from distinct NiO particles to porous NiO after both 2.5 hr (5.24c) and 5 hr (5.24d). At 700°C the transformation from NiO to Ni is seen and round Ni particles are observed (5.24e). Sintering and rounding of CeO_2 grains are also seen at this temperature. Finally, Figure 5.24f shows the large changes that have occurred after increasing the temperature to 800°C and ramping back down to

500°C. Figure 5.25 shows high resolution images from the same sample area as Figure 5.24. NiO and CeO_2 lattice fringes are witnessed in the original material at 150°C. NiO becomes porous and defective at 600°C but still exhibits crystallinity as shown by lattice fringe measurements. At 700°C, Ni particles are formed, confirmed by EELS and lattice spacing measurements.

5.5 Discussion

EDX quantification of 10Ni, 20Ni, and 10NiGd revealed the composition of the materials to be as expected on average. However, Ni distribution was highly heterogeneous. STEM EELS line scans and mapping revealed Ni to be contained in some CeO_2 particles in the form of small domains. The most probable conclusion from these results was that Ni is distributed throughout all samples in small NiO particles. The majority of Ni appears to be distributed in these domains and it is apparent that little to no solid solution exists in the materials. In the 20Ni sample it was shown that there is also a separate NiO phase present with a particle size similar to the size of CeO_2. From the *in-situ* experiment on 20Ni it was observed that reduction of NiO to Ni did not occur until 700°C. It was also observed that sintering initiated at 700°C in CH_4. Reduction of CeO_2 was not witnessed until the temperature had been increased to 800°C in CH_4 and then decreased back down to 500°C. The only evidence for Ni doping was the observation of Ni particles released from the CeO_2 particles in two different regions after being exposed to the reducing CH_4 environment and 800°C temperature.

Results have most importantly located the presence of Ni in samples and examined the interaction between Ni and CeO_2. Stabilization of NiO by CeO_2 appears to occur, raising the reduction temperature of NiO to 700°C for large particles. Due to the small size of Ni regions in 10Ni and 10NiGd it is possible that in these cases not all of the NiO reduces to Ni metal during catalytic reactions, even at high temperature, due to SMSI. The other possible conclusion is that a small amount of doping has occurred which has eliminated some of the active Ni on the surface. From the evidence presented with TEM it appears that the first case is more likely, although it is still possible that a small amount of Ni doping has occurred which could also contribute to the stabilization of NiO. Examination of 10Ni and 10NiGd revealed that they have roughly the same amount of Ni present, and the same particle size. Therefore, differences in their catalytic performance are not due to surface area effects or differences in Ni content. It is more likely that the interaction between Ce and Gd in 10NiGd has lessened the potential interaction between Ni and Ce. It is still unclear whether this interaction is the result of doping.

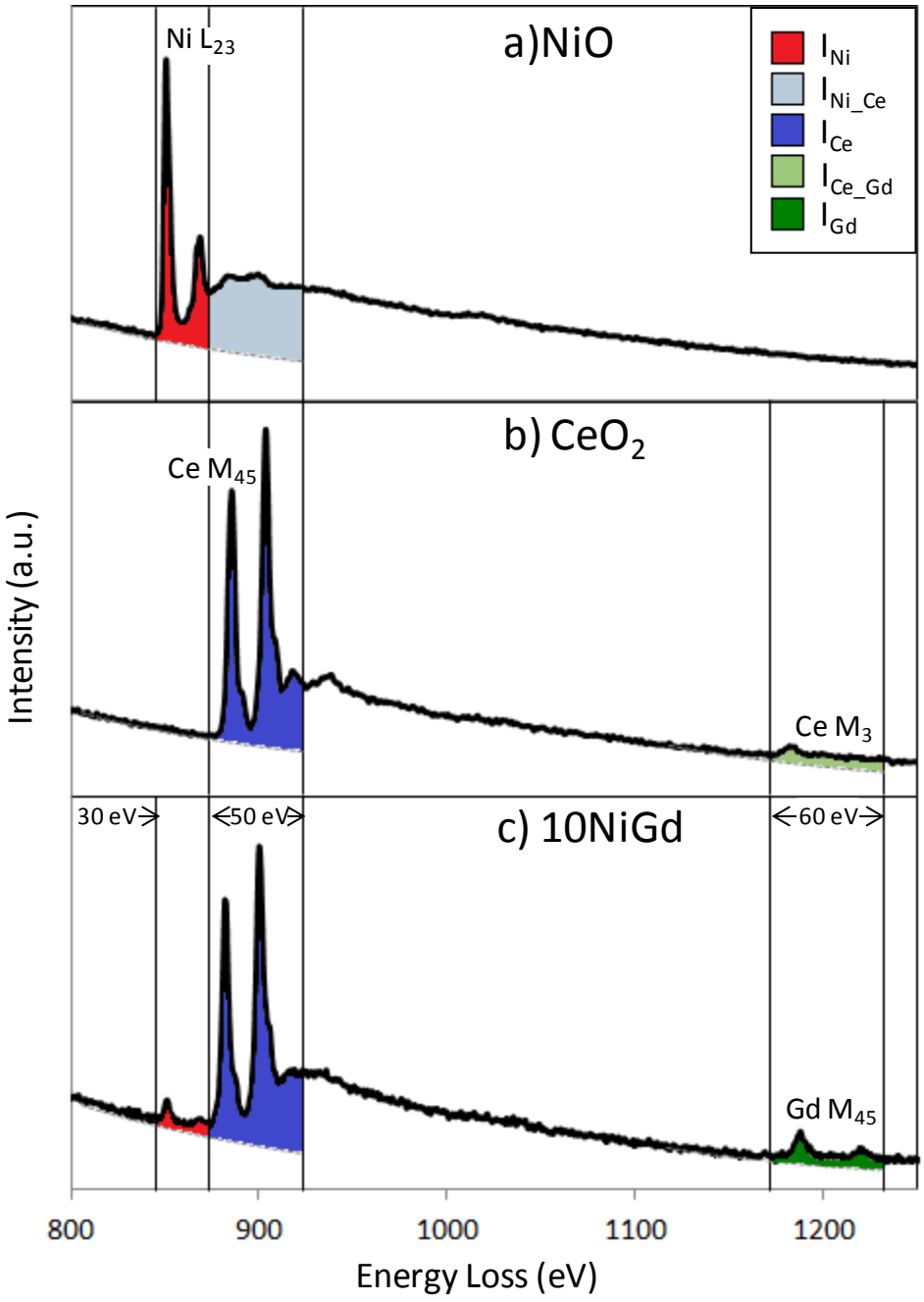

Figure 5.1: Electron energy loss spectra from a) NiO, b) CeO_2, and c) 10NiGd, showing the energy windows used for EELS quantification of Ce, Ni, and Gd as well as the integrated intensities used to determine correction factors for signal overlap.

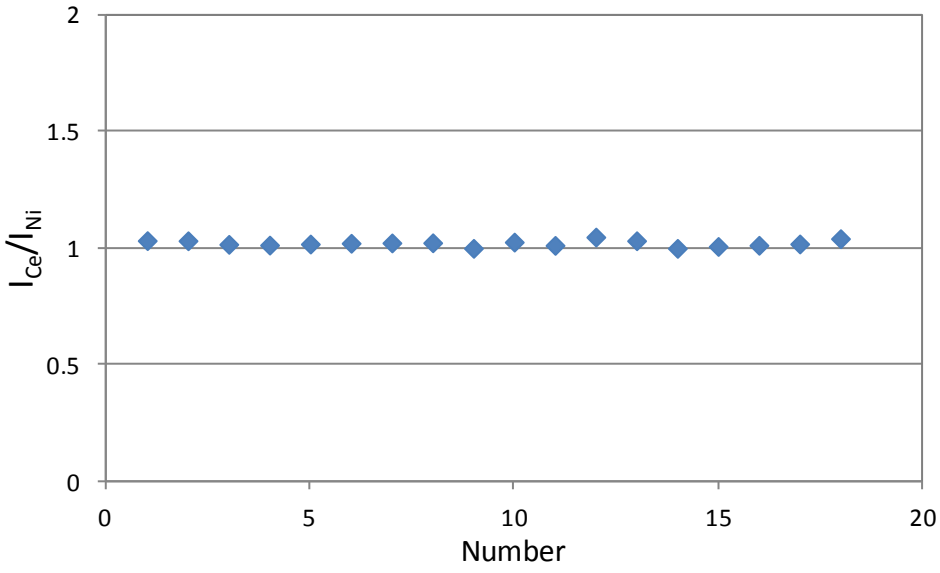

Figure 5.2: Plot of EDX quantification data showing intensity ratio I_{Ce}/I_{Ni} versus number of spectra.

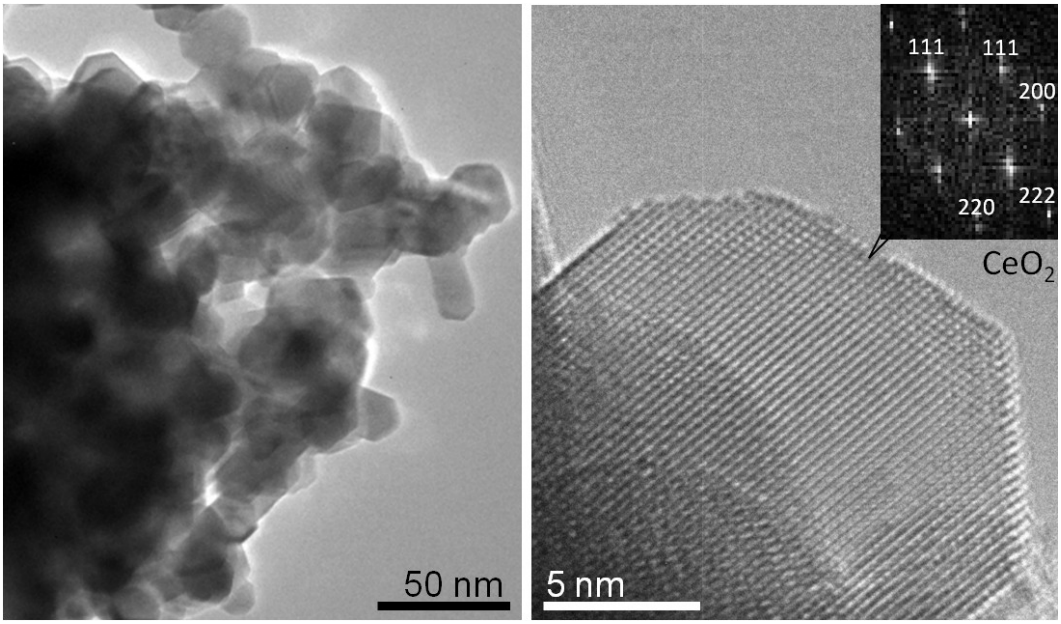

Figure 5.3: TEM micrograph of a cluster of pure CeO_2, and HREM image of a pure CeO_2 particle.

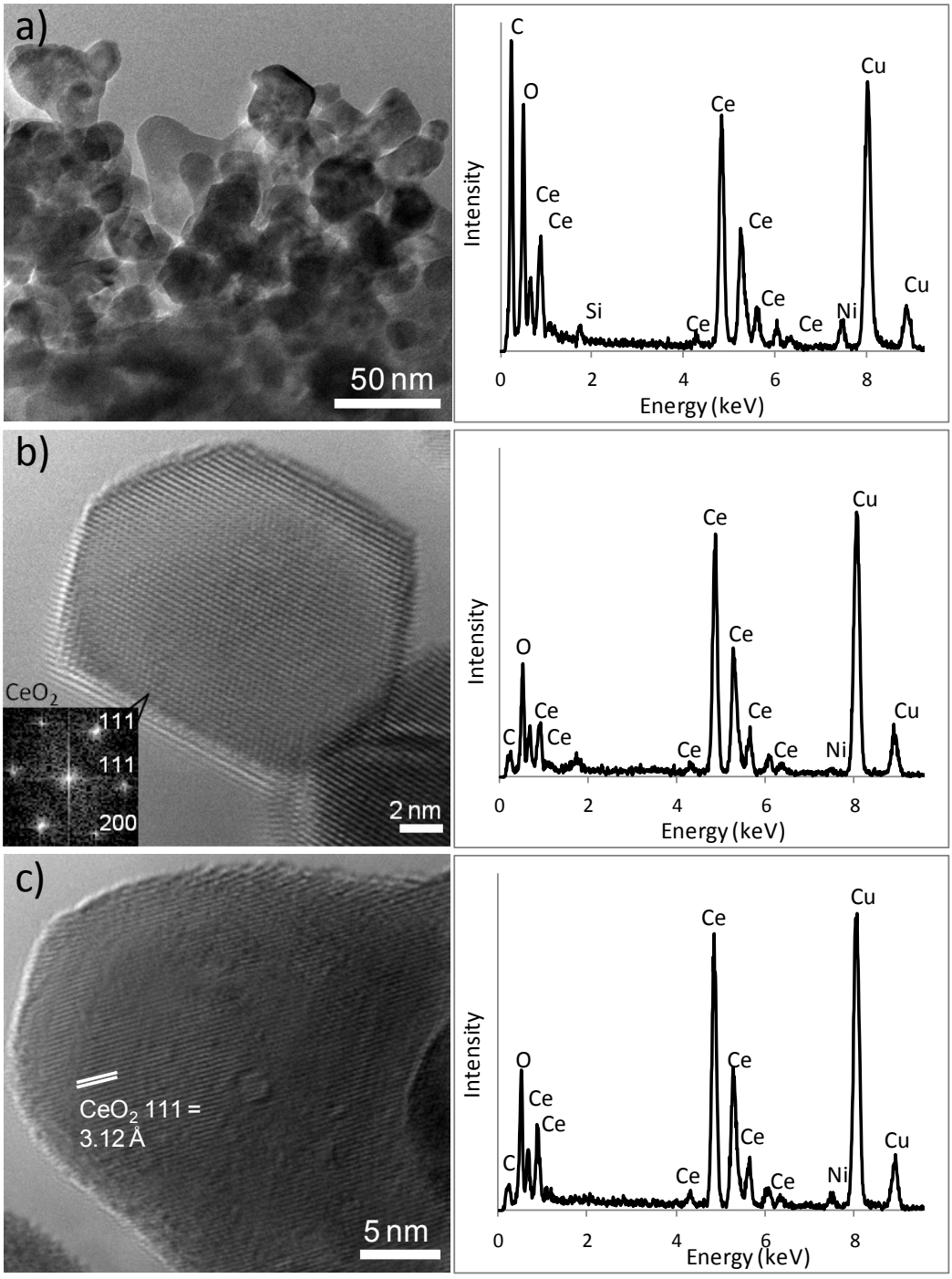

Figure 5.4: TEM images and quantified EDX spectra from spray dried 10Ni a) A cluster of nanoparticles containing 11.0 at.% Ni b) an individual nanoparticle revealing 2.0% Ni and c) a particle containing 4.3 at.% Ni.

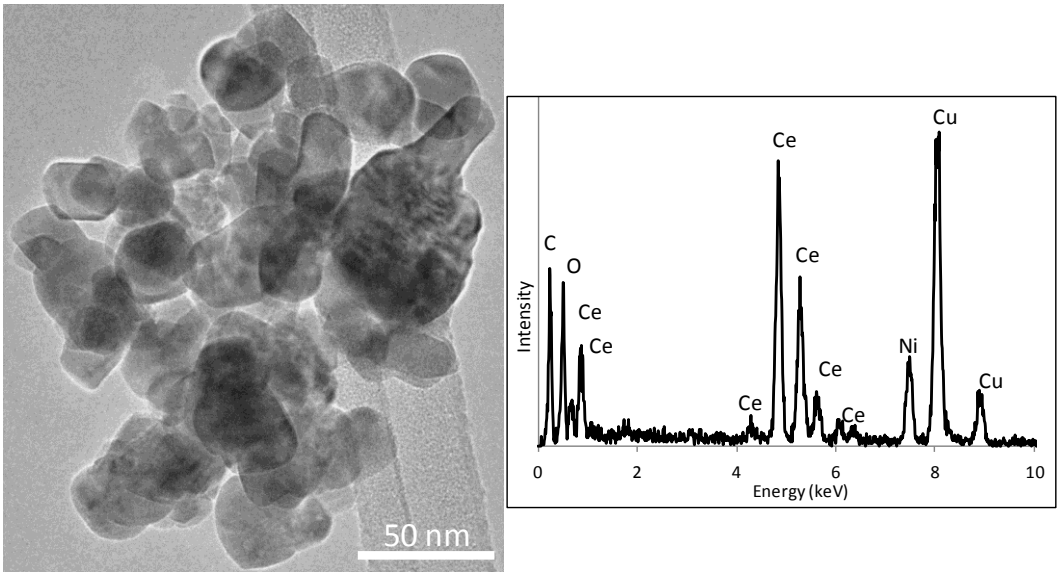

Figure 5.5: TEM image and EDX spectrum from a cluster of spray dried 20Ni containing 26.6 at.% Ni.

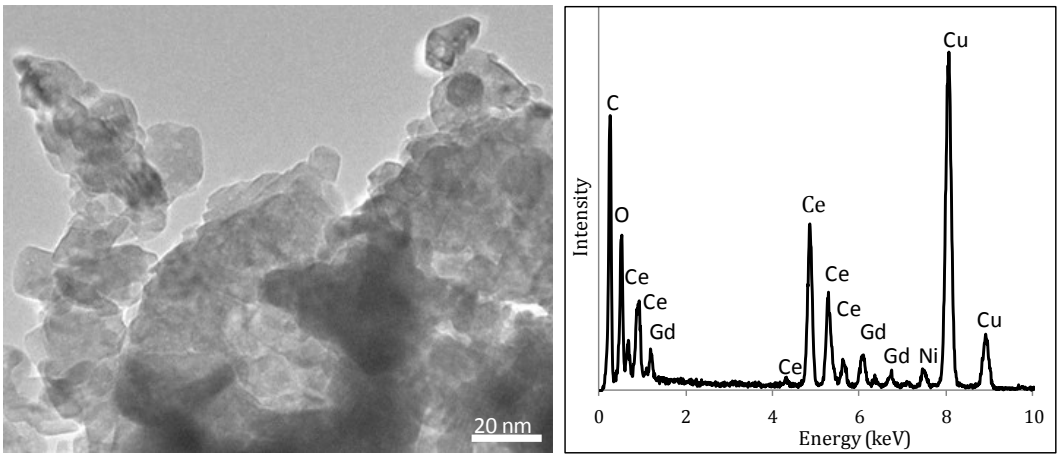

Figure 5.6: TEM image and EDX spectrum from a cluster of 10NiGd containing 10.3 at.% Ni and 12.9 at.% Gd.

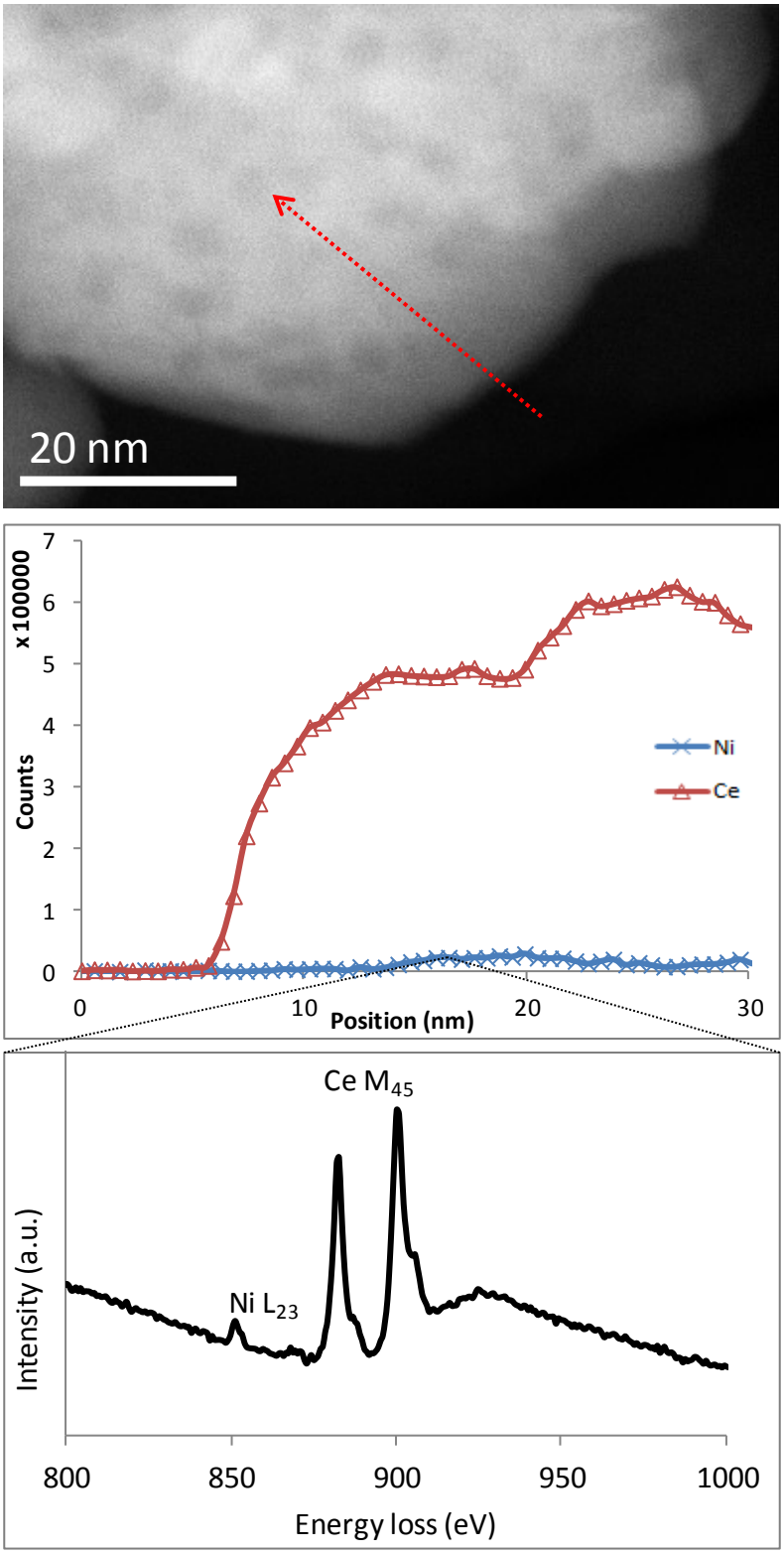

Figure 5.7: STEM ADF image of 10Ni sample, EELS line scan profile over the region showing Ni and Ce EELS signals as a function of position, and one energy loss spectrum.

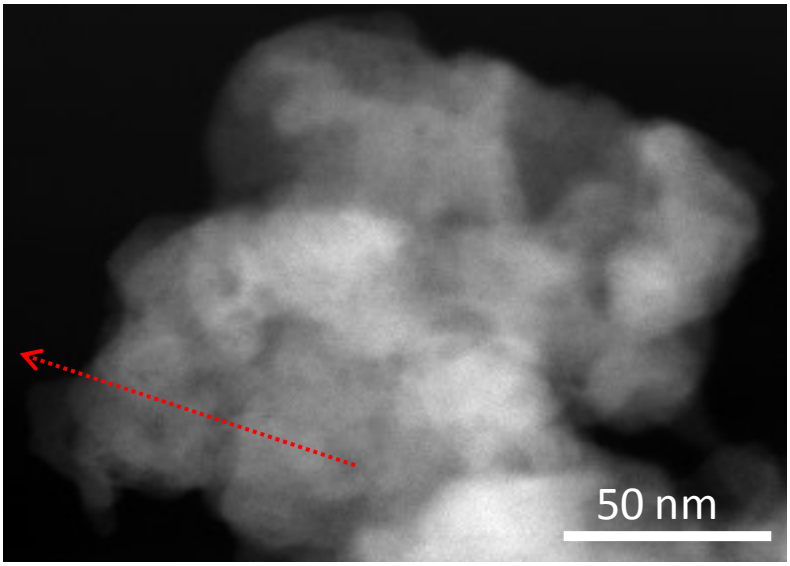
50 nm

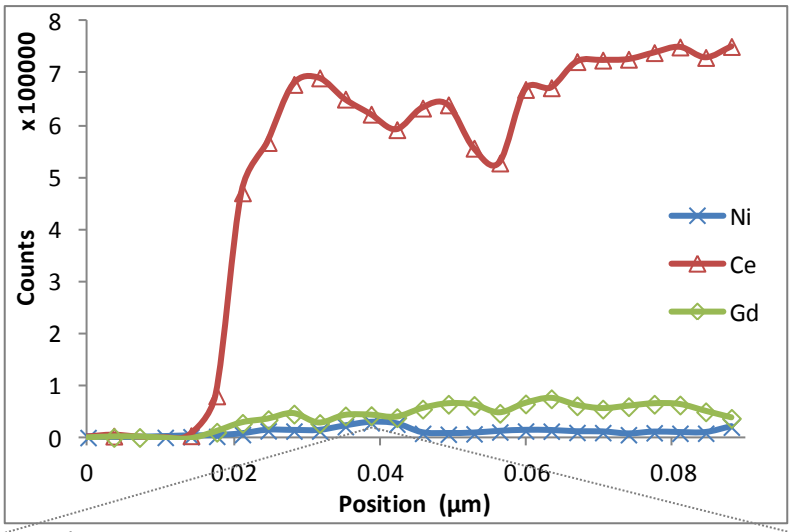
x 100000
Counts
8
7
6
5
4
3
2
1
0
0
0.02
0.04
0.06
0.08
Position (µm)
Ni
Ce
Gd

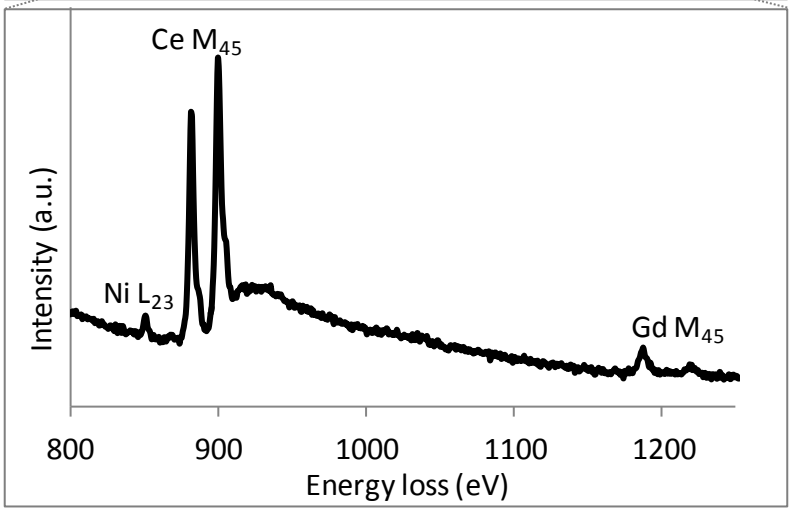
Ce M45
Ni L23
Gd M45
Intensity (a.u.)
800
900
1000
1100
1200
Energy loss (eV)

Figure 5.8: STEM ADF image of 10NiGd sample and EELS line scan profile over the region showing Ni, Ce, and Gd EELS signals vs. position and one energy loss spectrum.

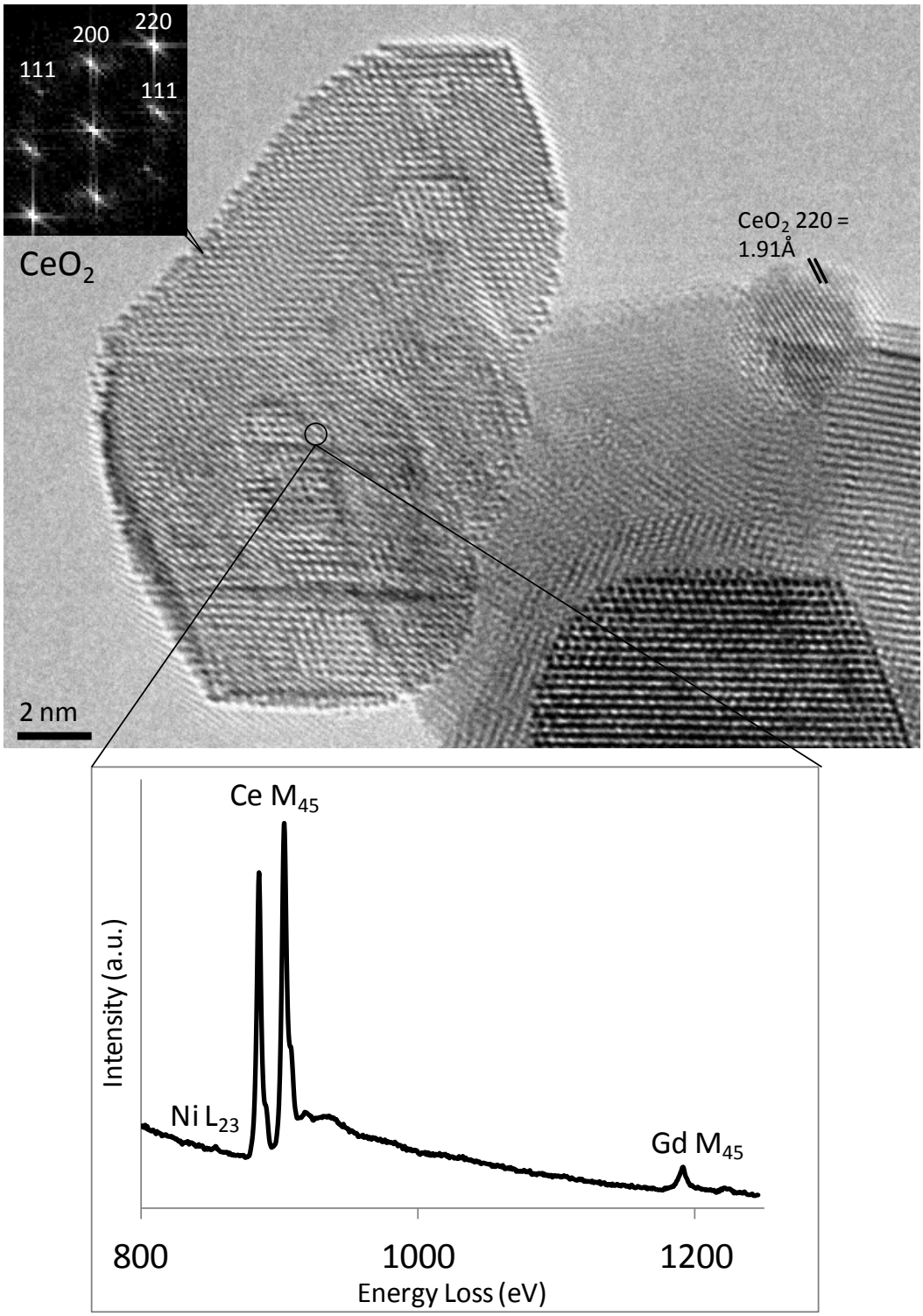

Figure 5.9: HREM image of 10NiGd with CeO_2 lattice fringes and energy loss spectrum over the region.

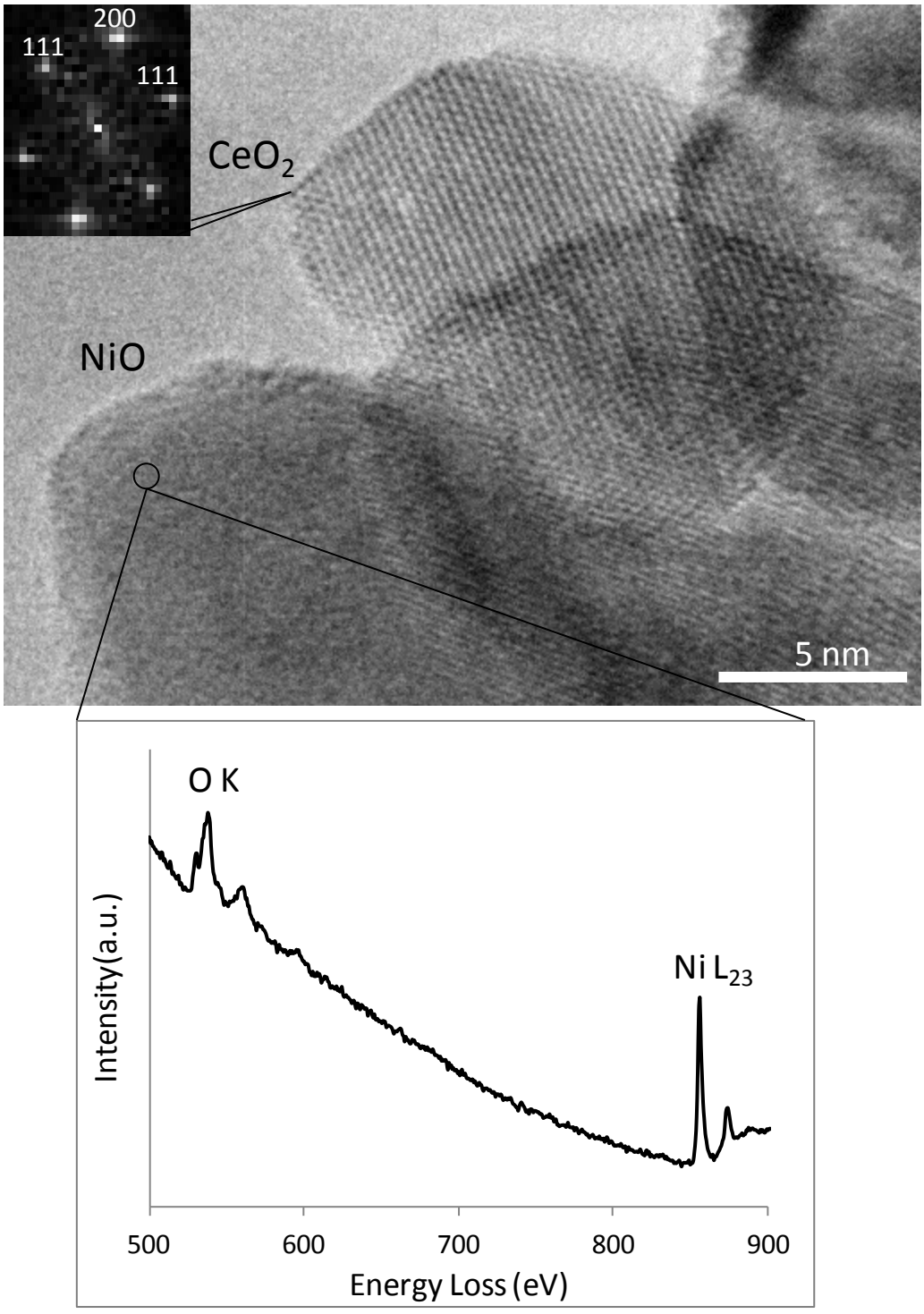

Figure 5.10: HREM image of 20Ni with CeO_2 crystalline particle next to a large NiO particle as revealed by EELS.

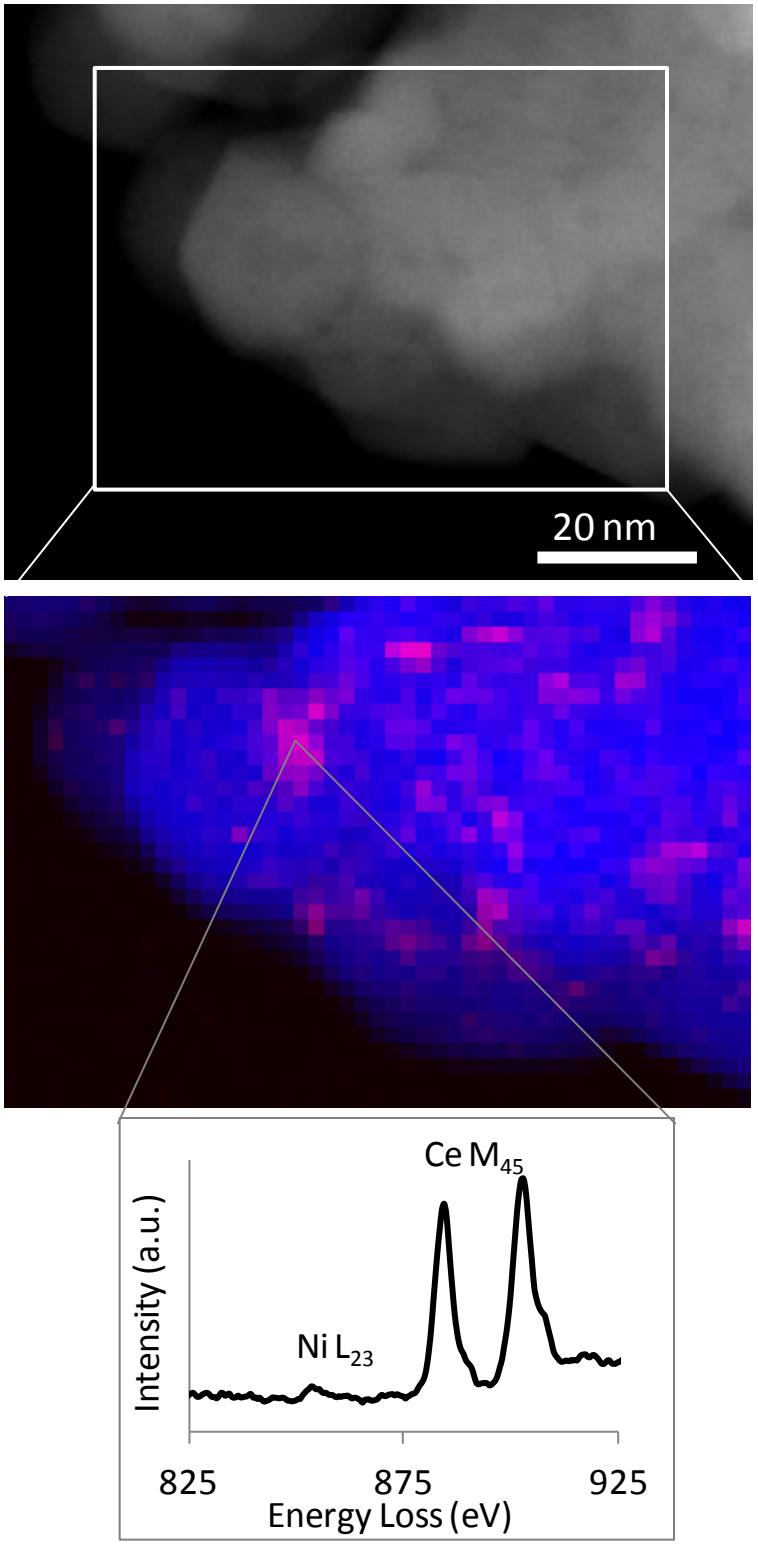

Figure 5.11: STEM ADF image of 10Ni showing area mapped by EELS in box, a colored EELS elemental map with Ce signal shown in blue and Ni signal shown in red, and one energy loss spectrum from the map.

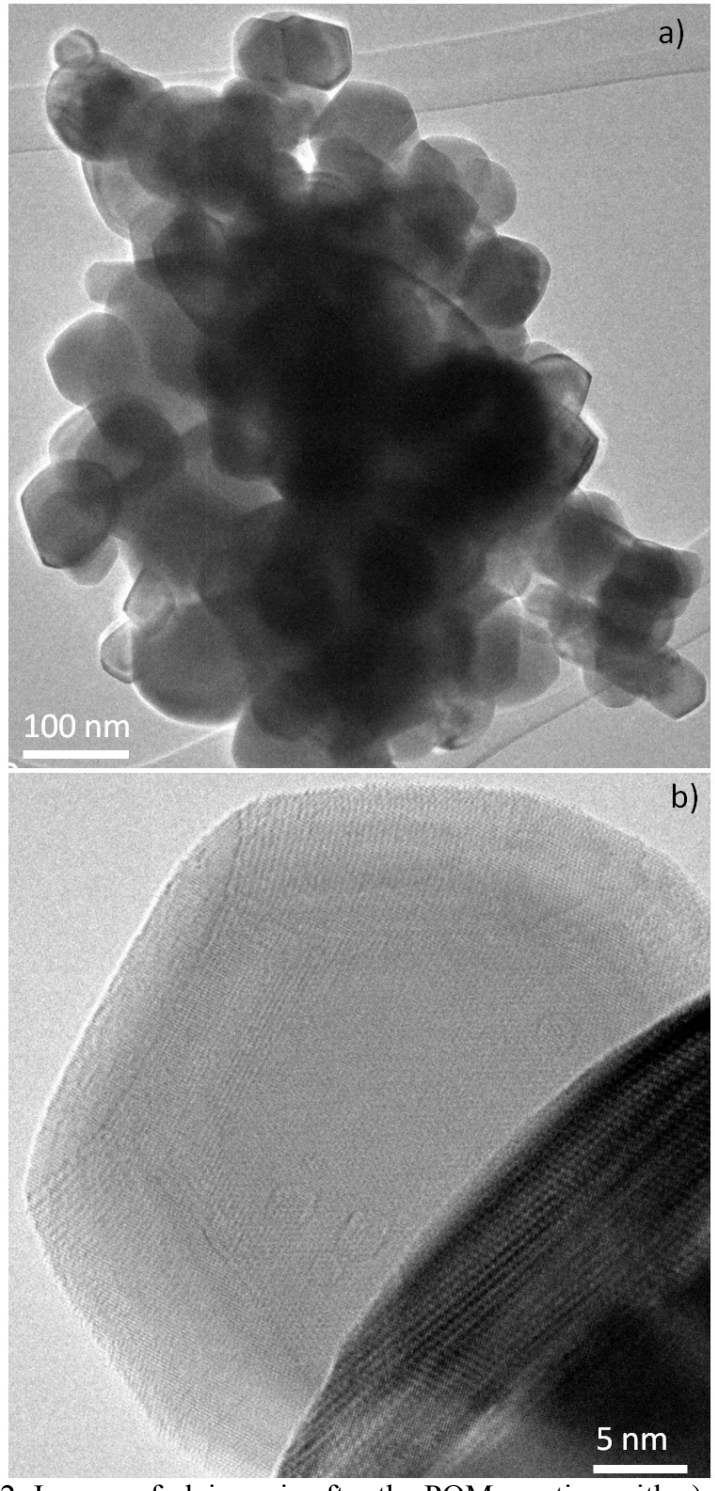

Figure 5.12: Images of plain ceria after the POM reaction with a) cluster of nanoparticles and b) HREM image of one CeO_2 particle.

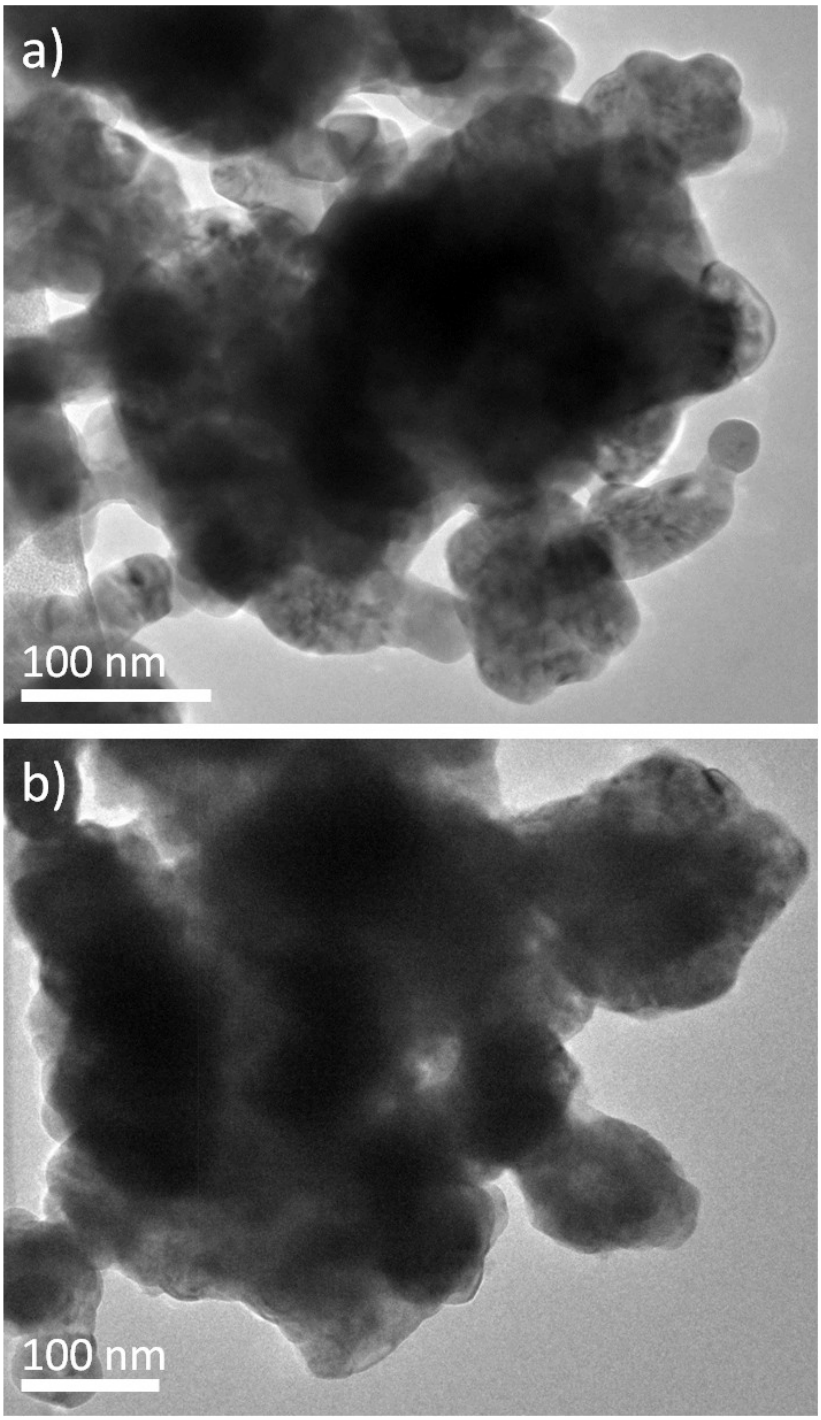

Figure 5.13: TEM images of Ni doped samples after the POM reaction with a) and b) 20Ni.

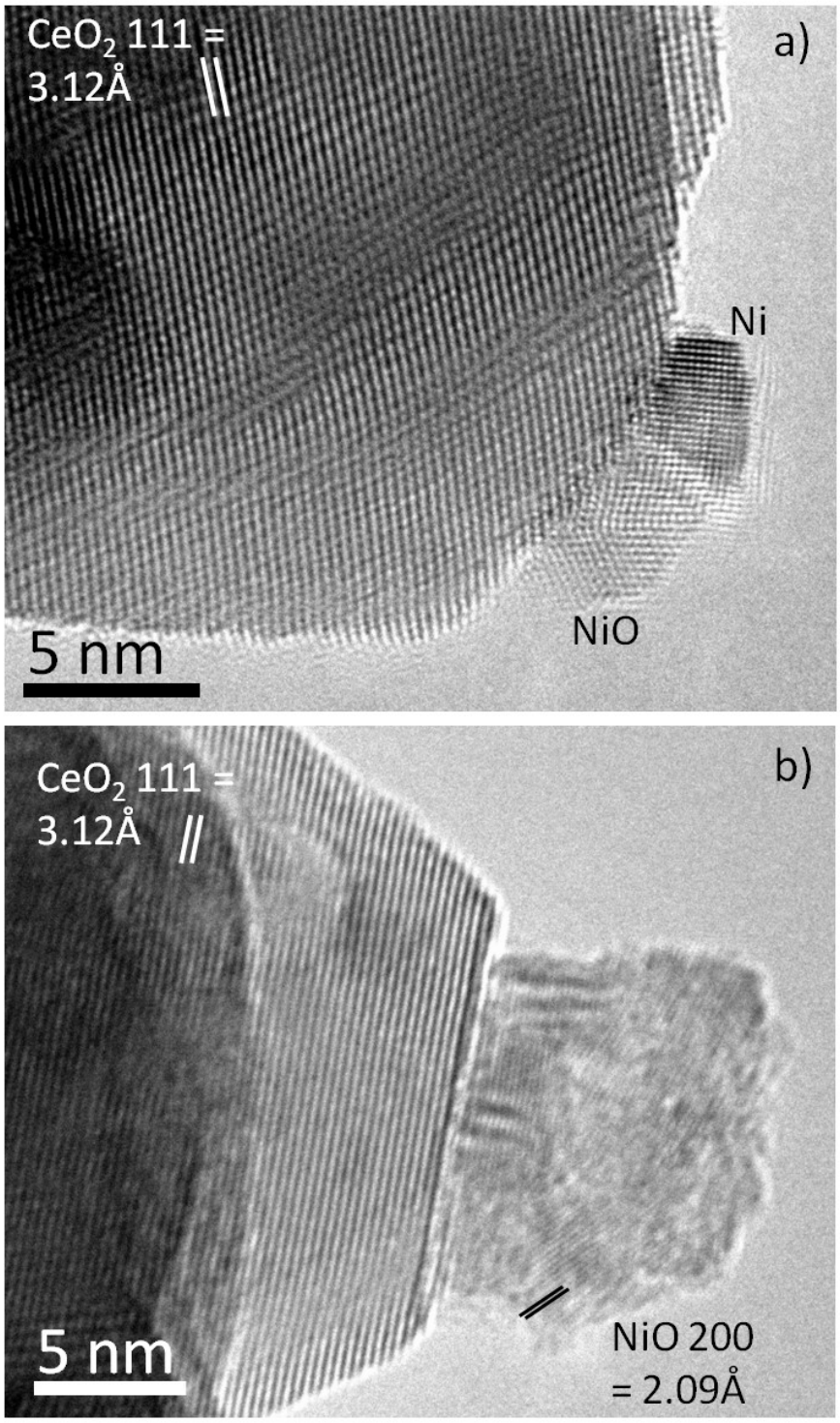

Figure 5.14: HREM images of 20Ni after catalytic reactions with a) 20Ni after POM, and b) 20Ni after SR.

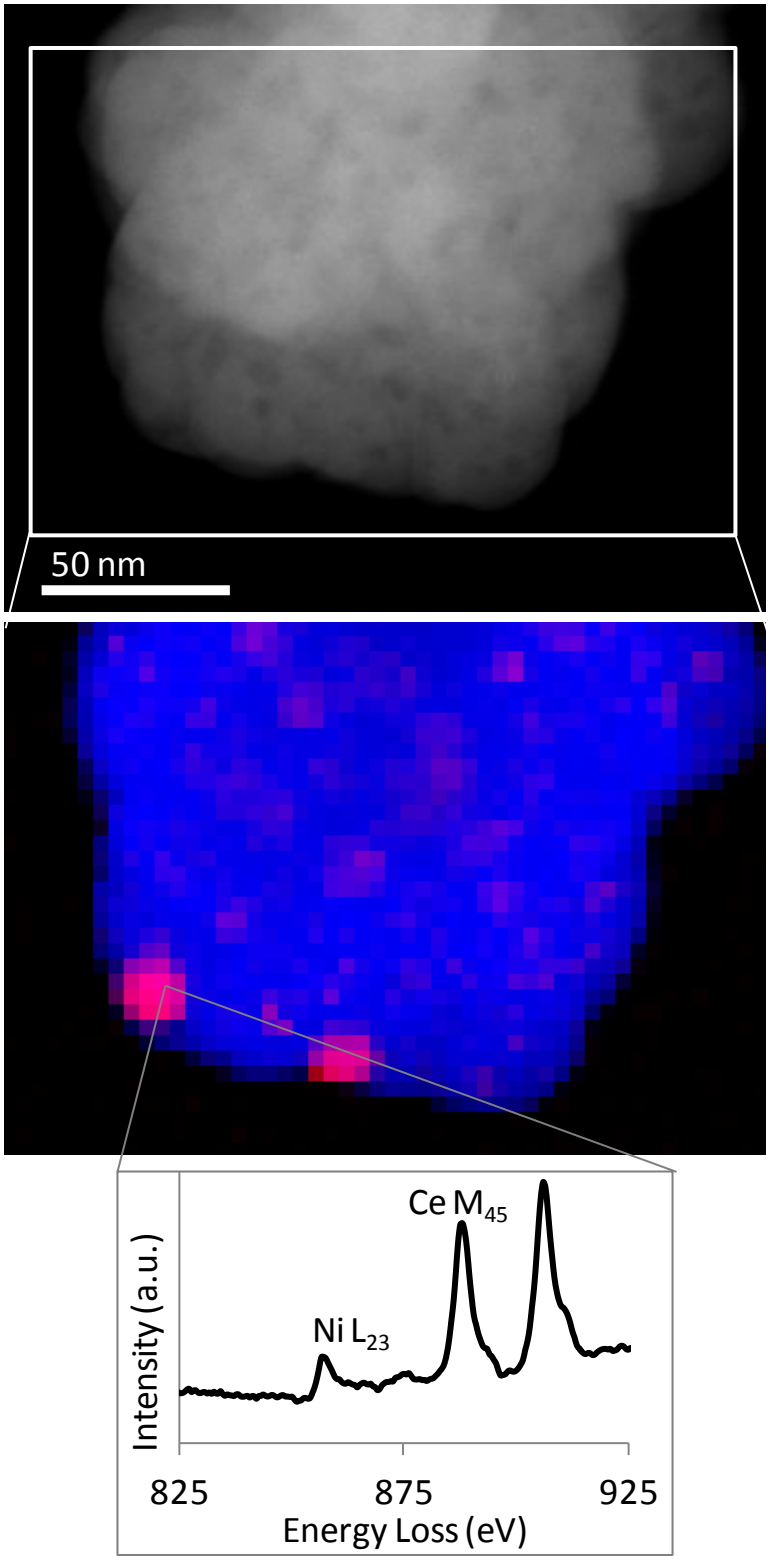

Figure 5.15: STEM ADF image of 10Ni after POM reaction showing area mapped by EELS in box, a colored EELS elemental map with Ce signal shown in blue and Ni signal shown in red, and one energy loss spectrum from the map.

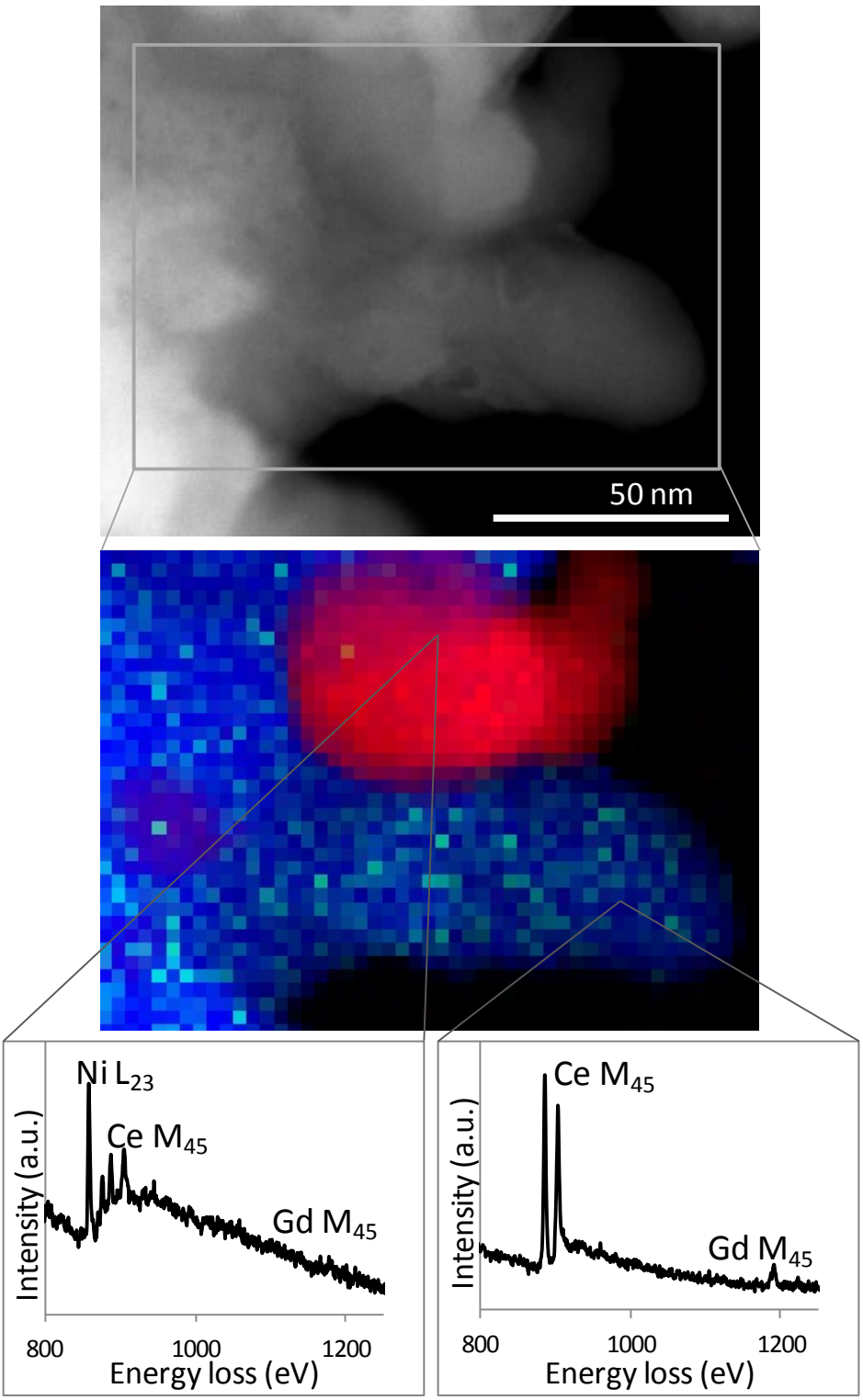

Figure 5.16: STEM ADF image of 10NiGd after POM reaction showing area mapped by EELS in box, a colored EELS elemental map with Ce signal shown in blue, Gd signal shown in green, and Ni signal shown in red, and two energy loss spectra from the map.

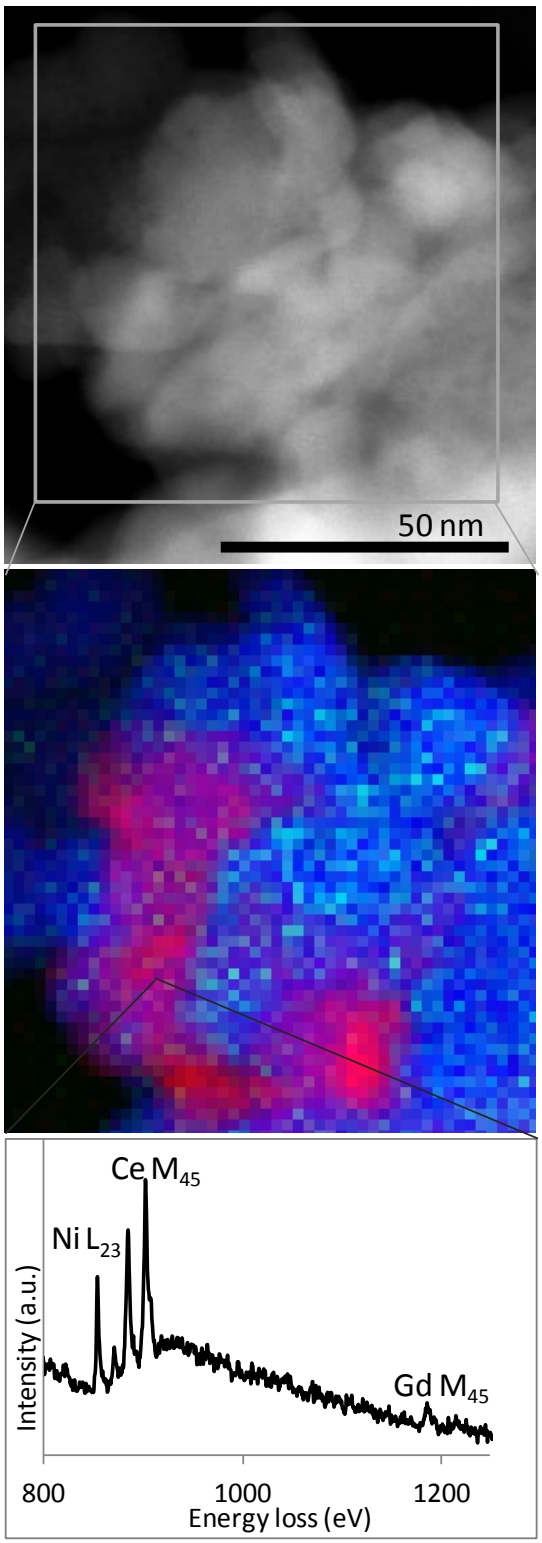

Figure 5.17: STEM ADF image of 10NiGd after POM reaction showing area mapped by EELS in box, a colored EELS elemental map with Ce signal shown in blue, Gd signal shown in green, and Ni signal shown in red, and one energy loss spectrum from the map.

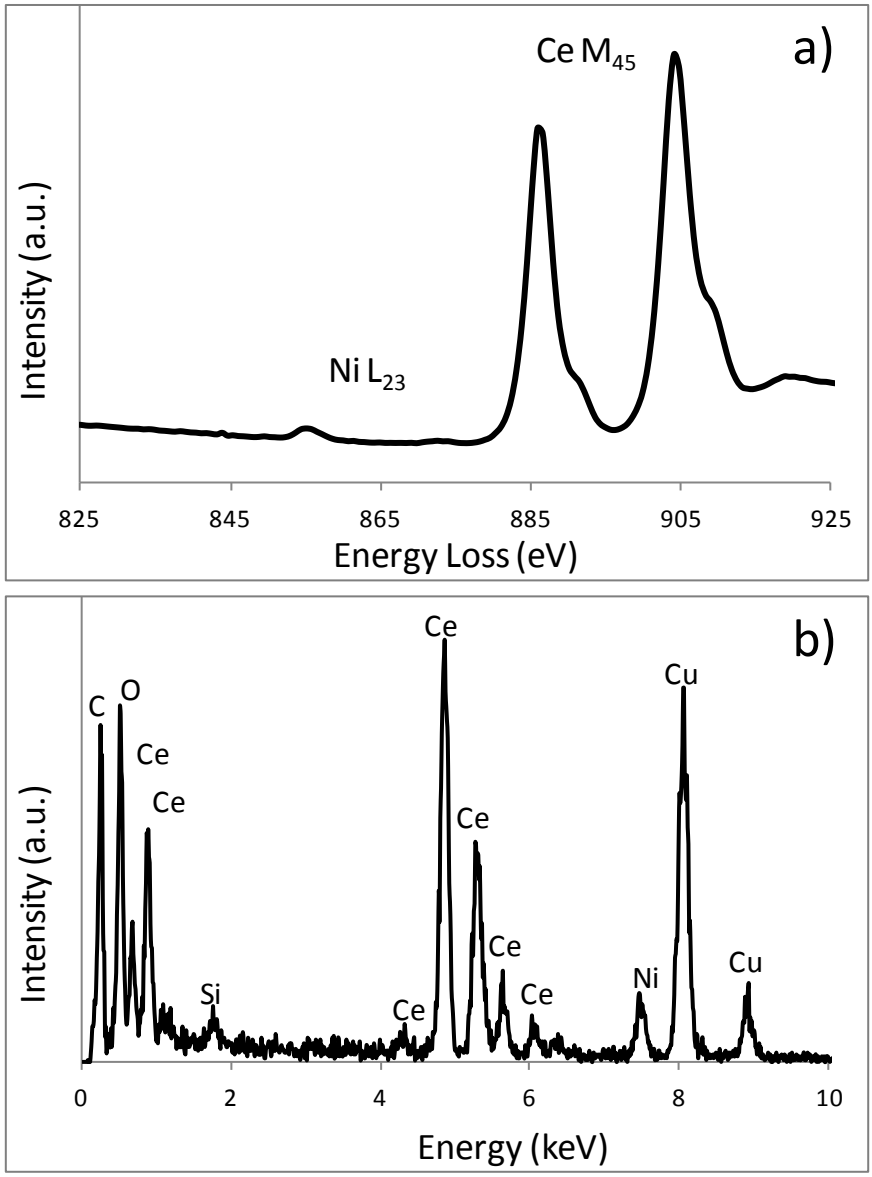

Figure 5.18: Spectra from 10Ni sample cluster containing 15.3 at.% Ni with a) EELS spectrum over the cluster and b) EDX spectrum over the same region used for quantification.

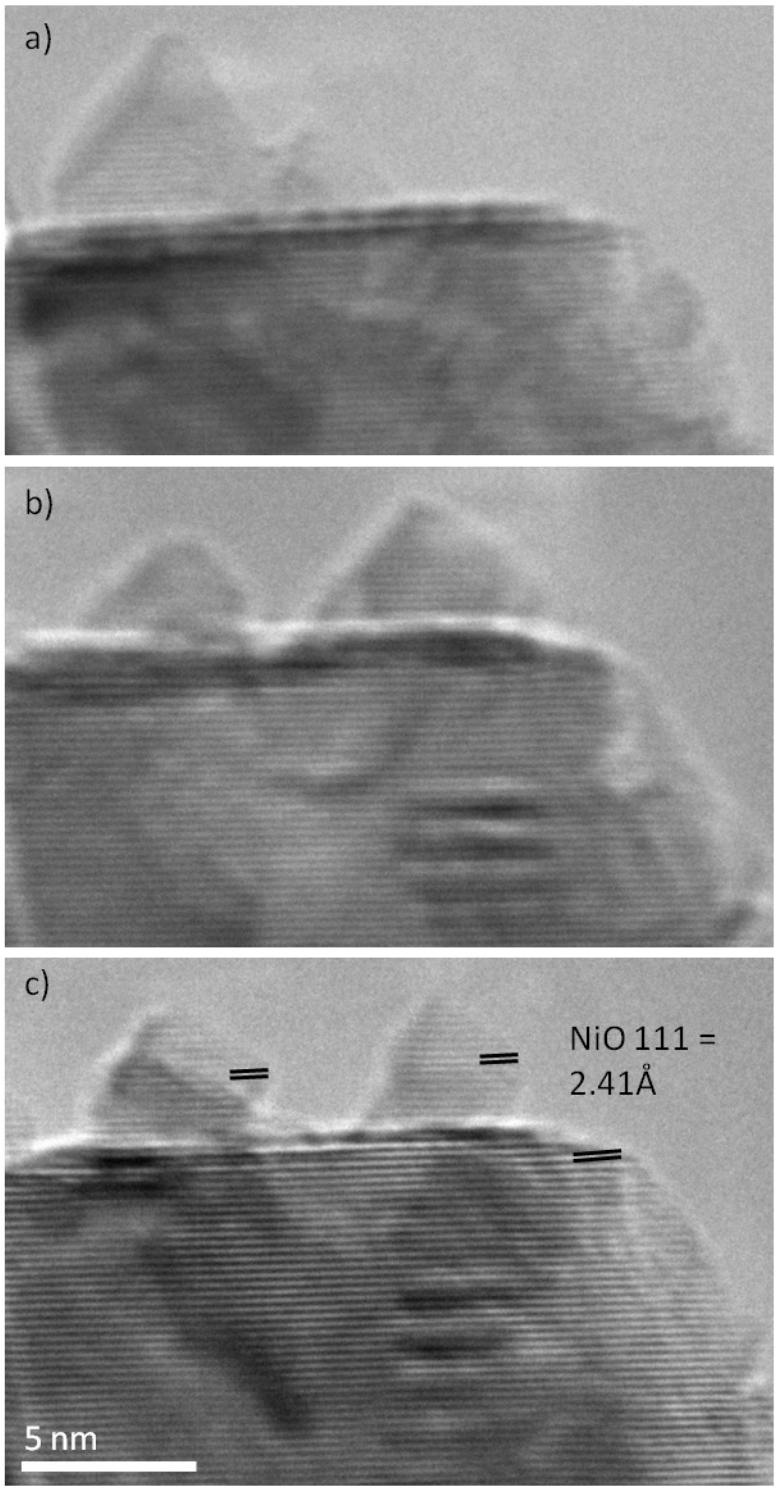

Figure 5.19: In-situ HREM images from 20Ni sample in 1 Torr CH_4 at 600°C. a) b) and c) show the region over time with a NiO particle growing NiO particles in the same orientation, as confirmed by lattice spacing measurements in c).

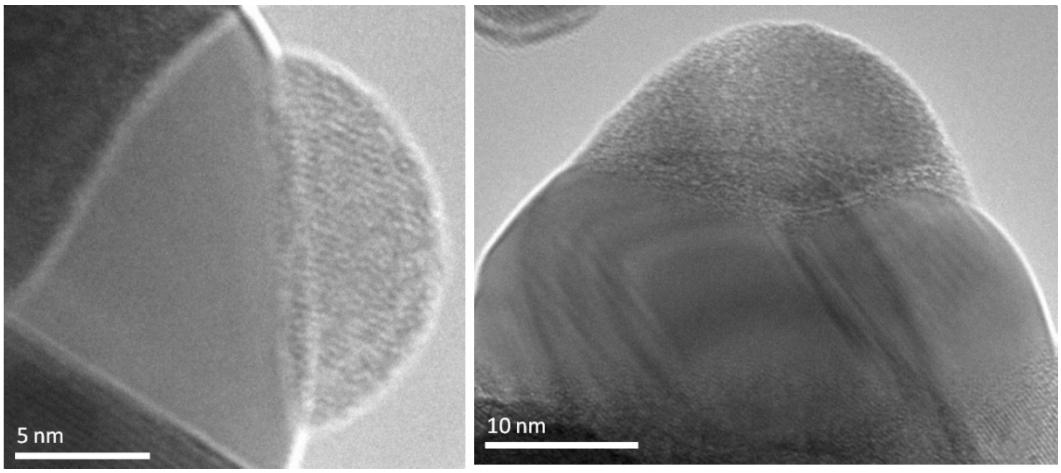

Figure 5.20: Decoration of Ni particles by ceria at 700°C in CH_4.

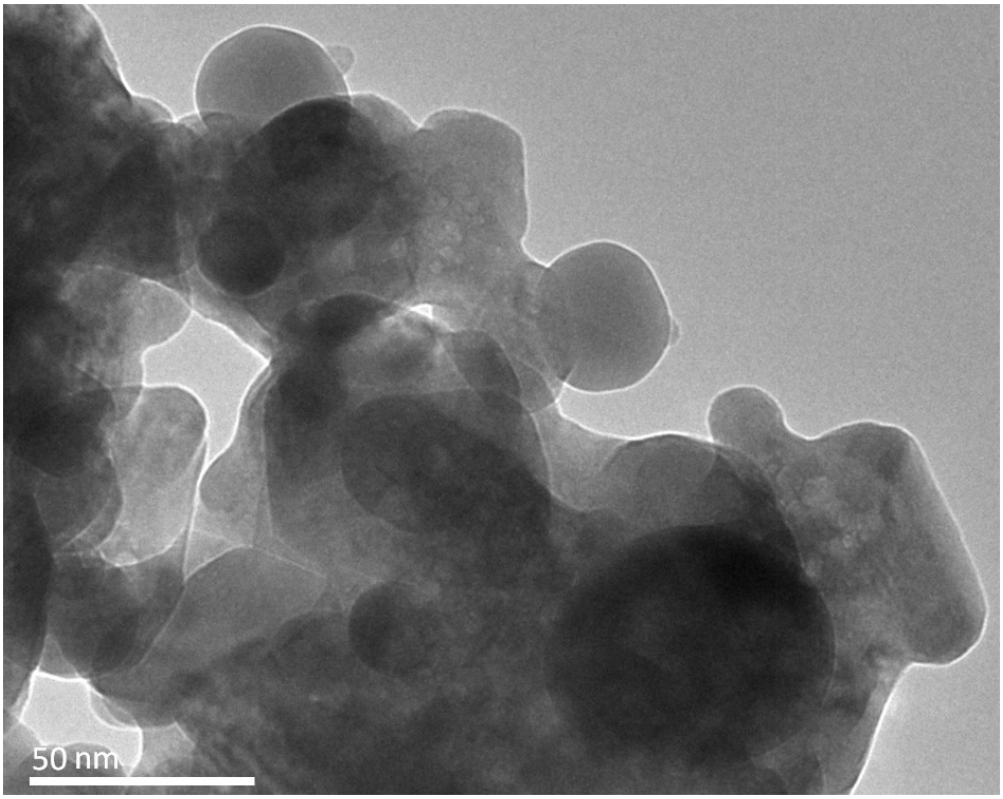

Figure 5.21: Cluster image of 20Ni at 800°C in 1 Torr CH_4 showing the degree of sintering of ceria and the formation of large Ni particles.

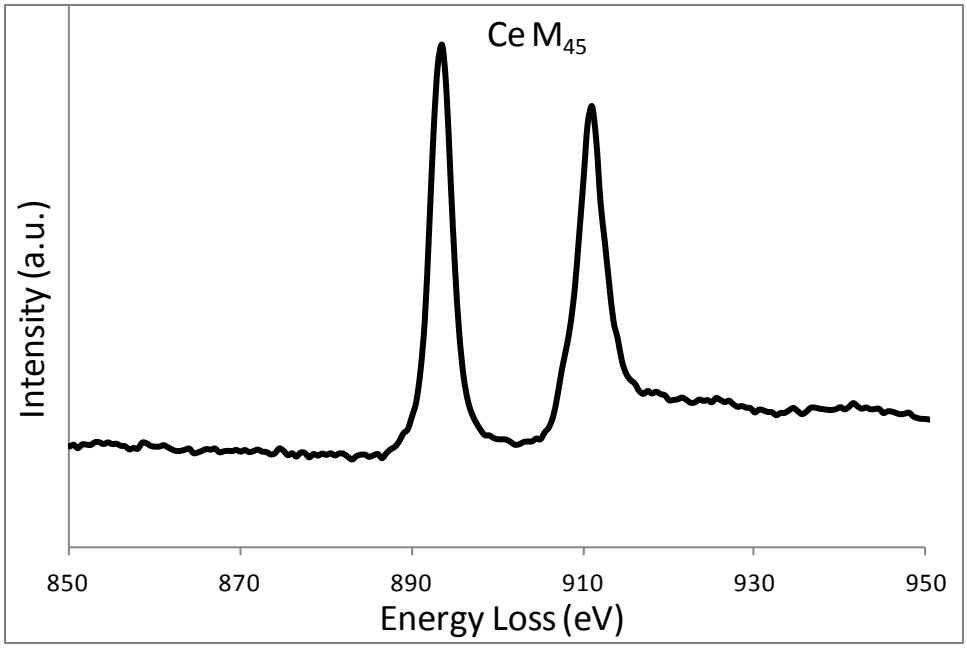

Figure 5.22: EELS spectrum from ceria particles in 1 Torr CH_4 after the temperature was increased to 800°C and then ramped down to 500°C. Reversal of the M_5 and M_4 line intensities reveal CeO_2 has been reduced.

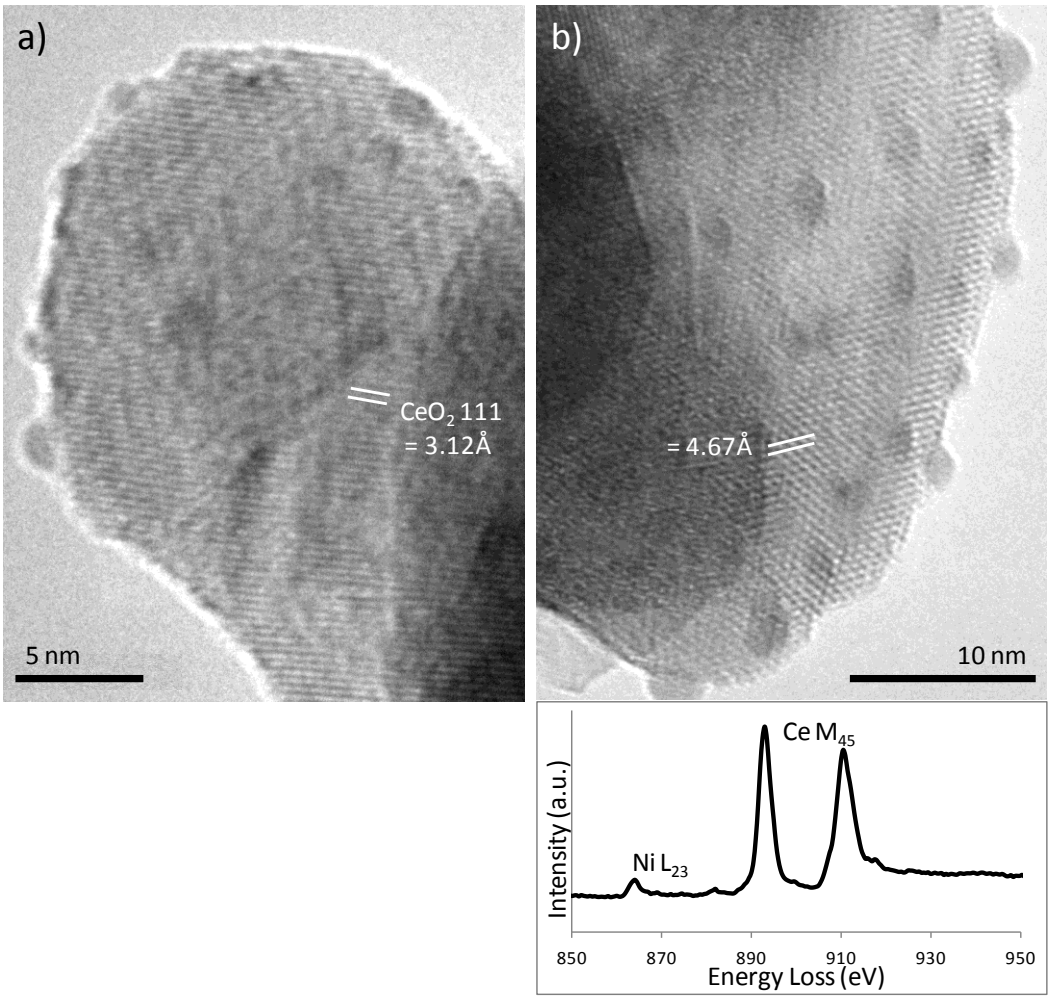

Figure 5.23: HREM images of 20Ni particles at 500°C in 1 Torr CH_4 with a) A particle showing lattice fringes matching the CeO_2 111 and b) A particle with unidentified lattice fringes and corresponding EELS spectrum revealing reduction of CeO_2 and the presence of Ni.

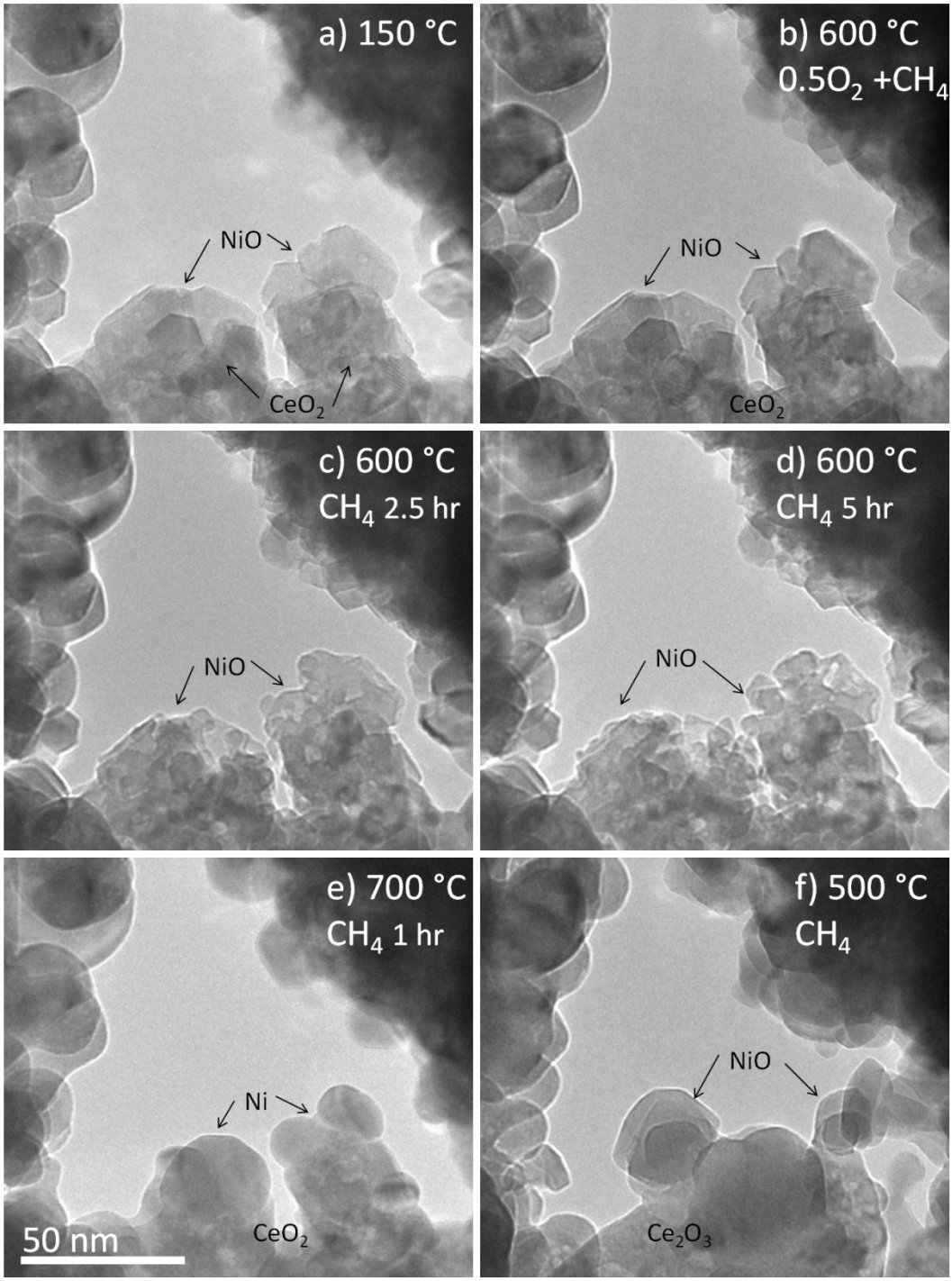

Figure 5.24: Progression of *in-situ* experiment for one region of 20Ni with a) cluster area at 150°C in no gas atmosphere b) The same area after an increase in temperature to 600°C in a gas environment of 0.75 Torr CH_4+0.5O_2 c) 600°C in 1 Torr CH_4 after 2.5 hours d) 600°C in 1 Torr CH_4 after 5 hours e) 700°C in 1 Torr CH_4 after 1 hour f) 500°C in 1 Torr CH_4 after first being increased to 800°C.

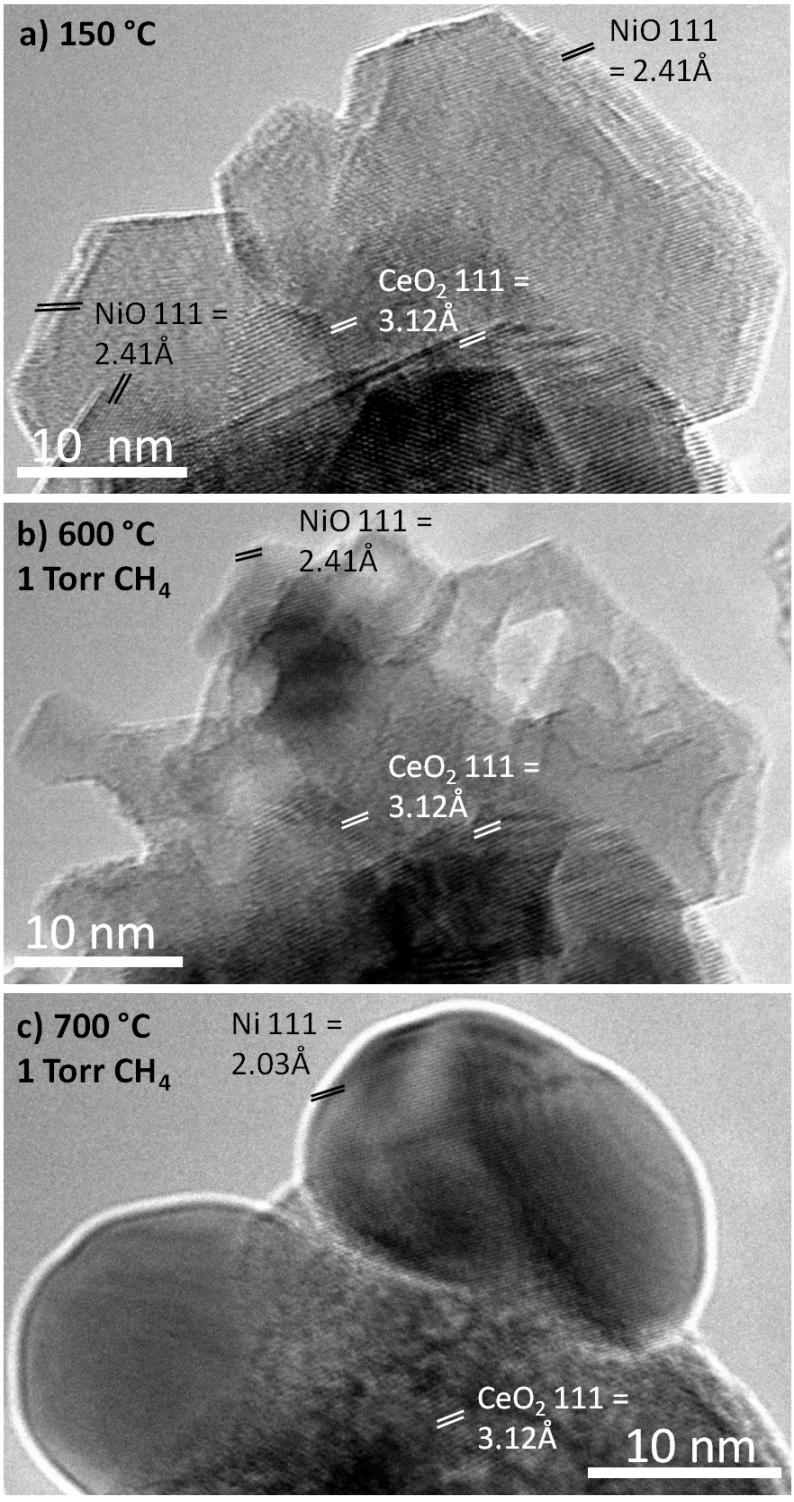

Figure 5.25: High resolution of sample area of Figure 5.24 with a) Initial region at 150°C revealing particles containing NiO and CeO_2 lattice fringes b) Sample region at 600°C in CH4 showing NiO has become disordered and unstable c) Sample region at 700°C in CH_4 showing Ni fringes indicating NiO has changed phase

Chapter 6

CONCLUSIONS

6.1 Summary of Results

In this work catalysts for fuel reforming in the solid oxide fuel cell anode were explored. Two reforming reactions, partial oxidation and steam reforming, were chosen and tested with methane. Catalysts were composed of ceria and nickel which are expected to have a strong interaction, potentially in the form of Ni doping in CeO_2. A spray drying technique was used to synthesize nanopowders of ceria containing nickel and gadolinium with compositions of CeO_2, $Gd_{0.1}Ce_{0.9}O_{2-y}$ (10Gd), $Ni_{0.1}Ce_{0.9}O_{2-y}$ (10Ni), $Ni_{0.2}Ce_{0.8}O_{2-y}$ (20Ni), and $Ni_{0.1}Gd_{0.1}Ce_{0.8}O_{2-y}$ (10NiGd). Ni doped compositions of 10Ni, 20Ni, and 10NiGd were synthesized to explore catalytic behavior and structure, and CeO_2 and 10Gd were prepared as reference materials. Samples were analyzed with XRD, catalytic testing, low magnification TEM imaging, HREM, EDX, EELS, and *in-situ* ETEM to determine structure and its relation it to fuel reforming potential in the SOFC anode.

Section 2 of chapter 3 presented XRD results for spray dried samples. Diffraction patterns for all materials contained peaks associated with CeO_2. From the peaks shifts observed in these reflections, lattice parameters of CeO_2, 10Ni, and 20Ni were found to be nearly identical. 10Gd and 10NiGd on the other hand were both found to have an increased lattice parameter as compared to pure CeO_2 and this was attributed to Gd doping in the samples. 20Ni was shown to have a

separate, crystalline NiO phase present in addition to CeO_2. From XRD results alone it was not clear whether doping of Ni into CeO_2 had occurred.

In chapter 4, materials were tested catalytically with partial oxidation and steam reforming of methane. For POM, catalytic performance for samples, listed from best to worst was 20Ni>10NiGd>10Ni>10Gd>CeO_2. 20Ni was found to be very active due to the presence of the separate NiO phase detected by XRD. The Gd containing samples showed enhancement in activity as compared to pure CeO_2 and 10Ni. For 10Gd this is likely a particle size effect due to the larger size of CeO_2. For 10NiGd, the particle size was equivalent to that of 10Ni. It was therefore assumed that a structural difference occurred in 10NiGd with the addition of Gd that allowed for more active Ni to be present on the CeO_2 surface. Overall the catalytic testing illustrated that the behavior of low Ni content samples was different than that of 20Ni, and that an understanding of Ni and Gd interaction with ceria was needed.

In chapter 5, transmission electron microscopy techniques were used to examine catalyst materials. Low magnification imaging and HREM were used to determine structure, and EELS and EDX were used to analyze composition. Quantification of EDX results over nanoparticle clusters in each sample determined that the compositions were as expected, on average. Images of Ni containing samples did not reveal any obvious differences as compared to pure CeO_2. After confirming Ni content in samples with EDX, STEM ADF imaging and EELS were used to locate Ni in samples. Results showed distinct heterogeneity of Ni in 10Ni and 10NiGd with small Ni domains observed over

CeO_2 particles. In 10NiGd, the Gd composition was uniform in CeO_2 grains, indicating Gd doping had occurred. In 20Ni, in addition to small Ni domains, a separate NiO phase was observed in the form of large particles, a result consistent with XRD analysis and catalytic testing.

EELS analysis before and after the POM reaction for 10Ni and 10NiGd did not reveal any obvious structural changes; Ni was still found to be heterogeneous and randomly distributed. TEM imaging before and after the POM reaction for 10Ni, 20Ni, and 10NiGd showed that the materials had sintered, with particles sizes doubling from their original values. Catalyst performance was still stable, with 20Ni showing no decrease in activity after accelerated aging with POM.

Finally, *in-situ* environmental TEM was performed on the 20Ni sample. This experiment was performed to directly examine the structure and behavior of the material under reactor conditions. The experiment was first motivated by exploring the interactions between Ni and CeO_2 during exposure to gas environments and high temperatures, and second by the desire to determine Ni location. An experiment was designed based on conditions in the catalytic reactor at different temperatures. 20Ni was examined with imaging and EELS at 150°C in vacuum, 600°C in CH_4 +0.5O_2, and in CH_4 at 600°C, 700°C, 800°C, and after a ramp down to 500°C. The main results of this experiment were first that at 600°C in CH_4, a porous, unstable NiO phase was observed. NiO present in the sample did not reduce to Ni metal until 700°C in CH_4. This behavior is different than behavior of Ni on an inert SiO_2 support, meaning that CeO_2 has stabilized NiO.

The *in-situ* experiment gave immediate evidence for the presence of the large, distinct, crystalline NiO phase. Attempts were also made to determine the presence of Ni doped into CeO_2 by reducing the +4 Ce in CeO_2 to the +3 oxidation state and inducing a structure change. The temperature was increased to 800°C but was only held for a short period of time and then ramped down to 500°C. The ceria in the sample at 500°C was found to be reduced based on EELS. It was also found that Ni had converted back to NiO in most regions. In two regions, small Ni particles, confirmed by EELS, were observed coming out of the ceria lattice.

6.2 Discussion

From all experiments it is concluded that 20Ni has a fundamentally different structure than 10Ni and 10NiGd. The presence of large particles of NiO in this sample allow it to be a good reforming catalyst that follows the thermodynamic potential during a temperature ramp down. From *in-situ* work it was found that these large particles do not reduce until a high temperature of 700°C. This effect appears to be due to the stabilization of NiO by ceria. In order for this to occur, it is speculated that the CeO_2 structure stabilizes NiO by giving up oxygen. However, at 700°C, the effect of the reducing CH_4 atmosphere overbears the rate at which CeO_2 can release oxygen, and Ni metal forms. This can be related to experiments in the catalytic reactor where the POM activation temperature for 20Ni will depend both on the temperature and whether the environment is oxidizing or reducing. For this sample the environment in the

reactor does not become reducing until 780°C, at which point the temperature is high enough for NiO to reduce to Ni, and activation occurs.

TEM and XRD results for 10Ni and 10NiGd suggest that they do not contain large NiO particles, and instead have small NiO domains spread over the ceria surface. It is therefore believed that there are 2 different types of Ni present in samples. In 20Ni there are large, segregated NiO particles that are catalytically active in addition to small NiO domains scattered over the ceria. Evidence suggests that 10Ni and 10NiGd only contain the second type of Ni. It is believed that these small NiO domains will not reduce to Ni metal until very high temperatures due to their size. The effect of stabilization by ceria will be more pronounced because there is a larger source of oxygen given by ceria to smaller Ni domains. The effect of this on catalytic performance will be to increase the activation temperature for POM as observed for both 10Ni and 10NiGd. In 20Ni, Ni particles are large enough to overcome effects of ceria, and the material performs similar to the thermodynamics limits on the ramp down. 10Ni and 10NiGd however, do not perform well on the ramp down. The performance during ramp down in both cases is worse than the ramp up. The source of this is most likely that the small Ni domains present immediately re-oxidize to NiO with a decrease in temperature.

The most promising evidence for Ni doping in CeO_2 is the *in-situ* observation of Ni particles being released from reduced ceria particles. However, this result was only seen in two locations and is not enough to confirm the existence of a solid solution. For 20Ni, 10Ni, and 10NiGd, Ni in the samples was

found to be present in the form of large NiO particles, or small Ni domains over CeO_2. Based on this any Ni doping in samples must be very small, and the extent of solubility must be much lower than 10 at.% Ni. EELS and XRD peak shift results for 10NiGd on the other hand indicate that Gd does dope into CeO_2 using the same spray drying synthesis procedure. Overall, we can conclude that the majority of Ni forms two types of NiO phases, a segregated NiO particle phase in 20Ni, and small NiO domains highly dispersed over ceria in 20Ni, 10Ni, and 10NiGd.

6.3 Future Work

Results presented in this work detail preliminary analysis on the structure and reforming potential of spray dried Ni/Ce/Gd catalysts. Methane was used for catalytic testing since it is the simplest hydrocarbon. However, higher fuels, especially those found in natural gas, should be tested to better determine direct reforming potential of the anode material.

The lower Ni content samples of 10Ni and 10NiGd are of interest for fundamental understanding of Ni/CeO_2 interaction and for determining if Ni doping in ceria is possible. These materials, however, have too little Ni present to perform well as catalysts for fuel cell anodes. Higher Ni content samples are of more interest for a solid oxide fuel cell anode. Based on results of this work, both of these areas should be explored further.

More experiments are needed on 10Ni and 10NiGd to conclusively determine if Ni doping occurs. *In-situ* experiments on these two samples would be highly useful to determine Ni inclusion in CeO_2. More work is also necessary to determine the effect of Gd in Ni/CeO_2 catalysts. Catalytic experiments should be run for pure CeO_2 and 10Gd that are confirmed to have the same particle size. Then, a better understanding of the role of Gd in 10NiGd can be gained.

Synthesis and characterization of higher Ni content samples is necessary to relate catalytic performance to use in the fuel cell anode, and to determine potential deactivation from higher Ni content. Results from 20Ni in this work show that when the spray drying method is used on cerium and nickel nitrates simultaneously, both CeO_2 and NiO particles are formed. Therefore it is also recommended that SOFC anodes are synthesized from this spray dried material directly to simplify processing.

REFERENCES

[1] U.S. Energy Information Administration (EIA). (2011). International Energy Outlook 2011. Retrieved from http://www.eia.doe.gov/oiaf/ieo/highlights.html

[2] Chorkendorff, I., Niemantsverdriet, J.W. (2003). *Concepts of Modern Catalysis and Kinetics*. Weinham: Wiley.

[3] Gogotsi, Y. (2006). *Nanomaterials Handbook*. Boca Raton: CRC Press.

[4] Song, C. (2002). Fuel processing for low-temperature and high-temperature fuel cells. Challenges, and opportunities for sustainable development in the 21st century. *Catalysis Today* **77**, 17–49.

[5] Singhal, S.C., Kendall, K. (2003). *High temperature solid oxide fuel cells: fundamentals, design, and applications*. Oxford: Elsevier.

[6] Singh, P., Minh, N. Q. (2004). Solid Oxide Fuel Cells: Technology Status. *International Journal of Applied Ceramic Technology* **1,** 5-15.

[7] Brett, D. J. L., Atkinson, A., Brandon, N. P., Skinner, S. J. (2008). Intermediate temperature solid oxide fuel cells. *Chemical Society reviews* **37**, 1568–78.

[8] McIntosh, S., Gorte, R.J. (2004). Direct hydrocarbon solid oxide fuel cells. *Chemical reviews* **104**, 4845-65.

[9] Atkinson, A., Barnett, S., Gorte, R.J., Irvine, J.T.S., McEvoy, A.J., Mogensen, M., Singhal, S.C., Vohs, J. (2004). Advanced anodes for high-temperature fuel cells. *Nature materials* **3**, 17–27.

[10] Offer, G. J., Mermelstein, J., Brightman, E., Brandon, N. P. 92009). Thermodynamics and Kinetics of the Interaction of Carbon and Sulfur with Solid Oxide fuel Cell Anodes. *Journal of the American Ceramic Society* **92**, 763–780.

[11] Van Beurden, P. (2004). *On the catalytic aspects of steam-methane reforming; A literature survey*. Energy Research Centre of the Netherlands (ECN), Technical Report I-04-003.

[12] Rostrup-Nielsen, J. (1993). Production of synthesis gas. *Catalysis today* **18**, 305–324.

[13] Edwards, J. (1995). The chemistry of methane reforming with carbon dioxide and its current and potential applications. *Fuel Processing Technology* **42**, 269–289.

[14] York, A., Xiao, T., Green, M. L. H. (2003). Brief overview of the partial oxidation of methane to synthesis gas. *Topics in catalysis* **22**, 345–358.

[15] Cimenti, M., Hill, J. M. (2009). Direct Utilization of Liquid Fuels in SOFC for Portable Applications: Challenges for the Selection of Alternative Anodes. *Energies* **2**, 377–410.

[16] Ahmed, S., Krumpelt, M. (2001). Hydrogen from hydrocarbon fuels for fuel cells. *International Journal of Hydrogen Energy* **26**, 291–301.

[17] Hagh, B. F. (2004). Stoichiometric analysis of autothermal fuel processing. *Journal of Power Sources* **130**(1-2), 85–94.

[18] Liu, D., Kaun, T.D., Liao, H.K., Ahmed, S. (2004). Characterization of kilowatt-scale autothermal reformer for production of hydrogen from heavy hydrocarbons. *International Journal of Hydrogen Energy* **29**, 1035–1046.

[19] Laosiripojana, N., Assabumrungrat, S. (2006). Hydrogen production from steam and autothermal reforming of LPG over high surface area ceria. *Journal of Power Sources* **158**, 1348–1357.

[20] Rostrup-Nielsen, J.R., Christensen, T.S., Dybkjaer, I. (1998). Steam reforming of liquid hydrocarbons. *Studies in Surface Science and Catalysis* **113**, 81–95.

[21] Staniforth, J., Ormerod, R. (2003). Running solid oxide fuel cells on biogas. *Ionics* **9** 336–341.

[22] Kang, I., Bae, J., Bae, G. (2006). Performance comparison of autothermal reforming for liquid hydrocarbons, gasoline and diesel for fuel cell applications. *Journal of Power Sources* **163**, 538–546.

[23] Trimm, D. (1999). Catalysts for the control of coking during steam reforming. *Catalysis Today* **49**, 3–10.

[24] Bell, A.T. (2003). The impact of nanoscience on heterogeneous catalysis. *Science* **299**, 1688-91.

[25] Tsang, S. C., Claridge, J. B., Green, M. L. H. (1995). Recent advances in the conversion of methane to synthesis gas. *Catalysis Today* **23**, 3–15.

[26] Basu, R. N. (2007). Materials for Solid Oxide Fuel Cells In *Recent Trend in Fuel Cell Science and Technology* **286.** India: Anamaya Publishers.

[27] Kilner, J.A., R. J. Brook. (1982). A Study of Oxygen Ion Conductivity in Doped Non-Stoichiometric Oxides. Solid State Ionics **6**, 237-252.

[28] Trovarelli, A. (2002). *Catalysis by ceria and related materials*. London: Imperial College Press.

[29] DeCaluwe, S.C., Sukeshini, A.M., Jackson, G.S. (2009). *ECS Transactions***16**(51), 235-251.

[30] Mogensen, M. (1994). Physical Properties of Mixed Conductor Solid Oxide Fuel Cell Anodes of Doped CeO_2. *Journal of the Electrochemical Society* **141**, 2122.

[31] Otsuka, K. (1998). Direct Partial Oxidation of Methane to Synthesis Gas by Cerium Oxide. *Journal of Catalysis* **175**, 152–160.

[32] Marina, O.A., Mogensen, M. (1999). High-temperature conversion of methane on a composite gadolinia-doped ceria–gold electrode. *Applied Catalysis A: General* **189**, 117–126.

[33] Zhou, Y., Perket, J.M., Crooks, A.B., Zhou,Z. (2010) *Effect of Ceria Support on the Structure of Ni Nanoparticles*. Physical Chemistry Letters **9,** 1447

[34] Beckers, J., Rothenberg, G. (2010). Sustainable selective oxidations using ceria-based materials. *Green Chemistry* **12**, 939.

[35] Gonzalez-DelaCruz, V., Holgado, J., Pereniguez, R., Caballero, A. (2008). Morphology changes induced by strong metal–support interaction on a Ni–ceria catalytic system. Journal of Catalysis **257**, 307–314.

[36] Huang, T.J., Wang, C.H. Methane decomposition and self de-coking over gadolinia-doped ceria-supported Ni catalysts. *Chemical Engineering Journal* **132**, 97–103.

[37] Barrio, L., Kubacka, A., Zhou, G., Estrella, M., Martínez-Arias, A., Hanson, J.C., Fernández-García, M., Rodriguez, J.A. (2010). Unusual Physical and Chemical Properties of Ni in $Ce_{1-x}Ni_xO_{2-y}$ Oxides: Structural Characterization and Catalytic Activity for the Water Gas Shift Reaction. *The Journal of Physical Chemistry C* **114**, 12689–12697.

[38] Pino, L., Vita, A., Cipitì, F., Laganà, M. & Recupero, V. (2007) Catalytic Performance of $Ce_{1-x}Ni_xO_2$ Catalysts for Propane Oxidative Steam Reforming. *Catalysis Letters* **122**, 121-130.

[39] Ponchel, A., D'Huysser, A., Lamonier, C. (2000). $CeNi_xO_y$ and $CeAl_zNi_xO_y$ solids studied by electron microscopy, XRD, XPS and depth sputtering techniques. *Physical Chemistry Chemical Physics* **2***,* 303-312

[40] 1. Shan, W., Fleys, M., Lapicque, F., Swierczynski, D., Kiennemann, A., Simon, Y., Marquaire, P.M.(2006). Syngas production from partial oxidation of methane over $Ce_{1-X}Ni_XO_Y$ catalysts prepared by complexation–combustion method. *Applied Catalysis A: General* **311**, 24–33.

[41] Zhou, G., Barrio, L., Agnoli, S., Senanayak, S.D., Evans, J., Kubacka, A., Estrella, M., Hanson, J.C., Martínez-Arias, A., Fernández-García, M., Rodriguez, J.A. (2010). High activity of $Ce_{1-x}Ni_xO_{2-y}$ for H_2 production through ethanol steam reforming: tuning catalytic performance through metal-oxide interactions. *Angewandte Chemie* **49**, 9680-4.

[42] Lamonier, C., Ponchel, a., D'Huysser, A., Jalowiecki-Duhamel, L. (1999). Studies of the cerium-metal–oxygen–hydrogen system (metal=Cu, Ni). *Catalysis Today* **50**, 247–259.

[43] Wrobel, G., Sohier, M., D'Huysser, A. (1993). Hydrogenation catalysts based on nickel and rare earth oxides: Part II: XRD, electron microscopy and XPS studies of the cerium-nickel-oxygen-hydrogen system. *Applied Catalysis A: General* **101**, 73–93.

[44] Pound, B. (1992). The characterization of doped CeO2 electrodes in solid oxide fuel cells. *Solid State Ionics* **52**, 183–188.

[45] Ranlov, J., Poulsen, F. W., Mogensen, M. (1993). Comment on "The characterization of doped CeO2 electrodes in solid oxide fuel cells" by B.G. Pound. *Solid State Ionics* **61**, 277–279.

[46] Pound, B. (1993). Response to Comment by J. Ranlov, F.W. Poulson and M. Mogensen on "The characterization of doped CeO2 electrodes in solid oxide fuel cells." *Solid state ionics* **61**, 281–284.

[47] Solak, N., Zinkevich, M., Aldinger, F. (2006). Reactivity in LaGaO3/Ni and CeO2/Ni Systems. *Fuel Cells* **6**, 87–92.

[48] Datta, P., Majewski, P., Aldinger, F. (2008). Synthesis and reactivity study of gadolinia doped ceria–nickel: A potential anode material for solid oxide fuel cell. *Journal of Alloys and Compounds* **455**, 454–460.

[49] Tianshu, Z., Hing, P., Huang, H., Kilner, J. (2002). Ionic conductivity in the CeO2–Gd2O3 system ($0.05 \leq Gd/Ce \leq 0.4$) prepared by oxalate coprecipitation. *Solid State Ionics* **148**, 567-573.

[50] Sharma, V., Eberhardt, K.M., Sharma, R., Adams, J.B., Crozier, P. A. (2010). A spray drying system for synthesis of rare-earth doped cerium oxide nanoparticles. *Chemical Physics Letters* **495**, 280-286.

[51] Wikipedia Commons. (2007). *Fluorite-unit-cell-3D-ionic*. Retrieved September 12, 2012 from: http://en.wikipedia.org/wiki/File:Fluorite-unit-cell-3D-ionic.png.

[52] McNair, H.M., Miller, J.M. (2011). *Basic Gas Chromatography*. New York: John Wiley & Sons.

[53] Poole, C. (2012). *Gas Chromatography*. Oxford: Elsevier.

[54] Reid, R.C., Prausnitz, J.M., Sherwood, T.K. (1977). *The Properties of Gases and Liquids*. New York: McGraw-Hill.

[55] Warren, B.E. (1990). *X-Ray Diffraction.* New York: Dover.

[56] Williams, D.B., Carter, C.B. (2009). *Transmission Electron Microscopy: A Textbook for Materials Science*. New York: Springer.

[57] Garratt-Reed, A.J., Bell, D.C. (2003). Energy *Dispersive X-ray Analysis in the Electron Microscope*. Oxford: BIOS Scientific Publishers Ltd.

[58] Rong, Y. (2012). *Characterization of Microstructures by Analytical Electron Microscopy (AEM)*. Berlin: Springer.

[59] Egerton, R.F. (2011). *Electron Energy-Loss Spectroscopy in the Electron Microscope.* New York: Springer.

[60] Egerton, R.F. (2009). Electron Energy-Loss Spectroscopy in the TEM. *Reports on Progress in Physics* **72**,016502.

[61] Smith, D.J. (2008). Development of Aberration-Corrected Electron Microscopy. *Microscopy and Microanalysis* **14**, 2-15.

[62] Sharma, R. (2005). An environmental transmission electron microscope for in-situ synthesis and characterization of nanomaterials. *Journal of Materials Research* **20(7)**, 1695-1707.

[63] Banhart, F. (2008). *In-Situ Electron Microscopy at High Resolution*, Singapore: World Scientific Publishing.

[64] Wikipedia Commons. (2011). *Bragg's Law*. Retrieved August 13, 2012 from: http://en.wikipedia.org/wiki/File:Braggs_Law.svg.

[65] Wikipedia Commons. (2009). *Scheme TEM*. Retrieved August 13, 2012 from: http://en.wikipedia.org/wiki/File:Scheme_TEM_en.svg

[66] Midtiby, H. Wikipedia Commons. (2008). *Characteristic Radiation*. Retrieved August 13, 2012 from: http://en.wikipedia.org/wiki/File:CharacteristicRadiation.svg.

[67] Wikipedia Commons. (2009). *EELS Idealised*. Retrieved August 13, 2012 from: http://en.wikipedia.org/wiki/File:EELS_Idealised.svg

[68] Mujumdar, A.S. (2007). *Handbook of Industrial Drying*. Boca Raton: CRC Press.

[69] Yuvaraj, S., Fan-Yuan, L., Tsong-Huei, C., Chuin-Tih, Y. (2003). Thermal Decomposition of Metal Nitrates in Air and Hydrogen Environments. *Journal of Physical Chemistry B* **107 (4)**, 1044-1047

[70] Mogensen, M., Lybye, D., Bonanos, N., Hendriksen, P., Poulsen, F. (2004). Factors controlling the oxide ion conductivity of fluorite and perovskite structured oxides. *Solid State Ionics* **174**, 279-286.

[71] Shannon, R. (1976). Revised effective ionic radii and systematic studies of interatomic distances in halides and chalcogenides. *Acta Crystallographica* **A32**, 751

[72] He, B.B. (2009). *Two-dimensional X-Ray Diffraction*. Hoboken: John Wiley & Sons.

[73] Williamson, G.K., Hall, W.H. (1953). X-ray line broadening from filed aluminium and wolfram, *Acta Metallurgica* **1**, 22-31.

[74] Chenna, S., Banerjee, R., Crozier, P. A. (2011). Atomic-Scale Observation of the Ni Activation Process for Partial Oxidation of Methane Using In Situ Environmental TEM. *ChemCatChem* **3**, 1051–1059.

[75] Chenna, S., Crozier, P.A. (2012) In situ environmental transmission electron microscopy to determine transformation pathways in supported Ni nanoparticles. *Micron* (in press) **43**(11), 1188–1194.

[76] Istadi, I. (2012). Thermodynamic analysis of synthesis gas and higher hydrocarbons productions from methane, in Indarto, A. & Palguandi, J. (Eds.), *Syngas: Production, Applications, and Environmental Impact.* Hauppauge: Nova Science Pub Inc.

[77] Koch, C.C. (2006). *Nanostructured Materials: Processing, Properties and Applications*. Norwich: William Andrew publishing.

[78] Florio, D. Z., Esposito, V., Traversa, E., Muccillo, R., Fonseca, F. C. (2009). Master sintering curve for Gd-doped CeO2 solid electrolytes. *Journal of Thermal Analysis and Calorimetry* **97**(1), 143–147.

[79] Kinemuchi, Y., Watari, K. (2008). Dilatometer analysis of sintering behavior of nano-CeO2 particles. *Journal of the European Ceramic Society* **28**(10), 2019–2024.

[80]Veranitisagul, C., Koonsaeng, N., Laosiripojana, N., Laobuthee, A. (2012). Preparation of gadolinia doped ceria via metal complex decomposition method: Its application as catalyst for the steam reforming of ethane. *Journal of Industrial and Engineering Chemistry* **18**, 898–903.

[81] Rollier, J., Petitpas, G., Gonzalez-Aguilar, J., Darmon, A., Fulcheri, L., Metkemeijer, R. (2008). Thermodynamics and Kinetics Analysis of Gasoline Reforming Assisted by Arc Discharge. *Energy & Fuels* **22**, 1888–1893

[82] Manoubi, T., Colliex, C., Rez, P. (1990). Quantitative electron energy loss spectroscopy on M45edges in rare earth oxides. *Journal of Electron Spectroscopy and Related Phenomena* **50**(1),1-18.

[83] Sharma, R., Crozier, P.A., Kang, Z. C., Eyring, L. (2004). Observation of Dynamic nanostructural and nanochemical changes in ceria-based catalysts during in-situ reduction. *Philosophical Magazine* **84**(25-26), 2731–2747.

APPENDIX A

DATA FOR SUPPORTED METAL CATALYSTS

Catalysts composed of Ni metal dispersed on oxide supports were prepared by incipient wetness impregnation. In this process, metal precursors are dissolved in solution. The concentration of this solution is dependent on the desired loading of metal. The solution is added to the dry substrate material with a volume equivalent to the pore volume of the material. The pore volume is a measure of the porosity of the substrate and is defined as the ratio of air volume to the total volume. The theory is that the volume of solution added to the substrate should be equivalent to its internal empty space so all pores become impregnated with solution. The precursor used was nickel nitrate hexahydrate ($Ni(NO_3)_2.6H_2O$) from Sigma Aldrich). Nickel nitrate was dissolved in ethanol to create a solution for a desired nickel loading of 2.5 wt%. This solution was added to dry ceria and silica (SiO_2) in a saturated alcohol environment to prevent drying and allow for even dispersion. The mixtures were ground with a mortar and pestle for 10 minutes and then dried at 120 °C for 2 hours. The samples were reduced within the reactor at 400°C for 3 hours in a gas environment of 5% Ar/H_2 to form Ni particles and the partial oxidation reaction was performed. Work on Ni/SiO_2 was performed by a previous group member to explore Ni behavior on inert SiO_2. Work on CeO_2 was done to compare to both Ni/SiO_2 and to the doped catalysts.

Results for Ni/SiO_2 are shown in Figure A.1. Below 300°C, no catalytic conversion takes place. Around 300°C there is an increase in O_2 and CH_4 conversion where CO_2 begins to form with 100% selectivity. A rapid increase in O_2 conversion is observed with increase in temperature. At 775°C a sharp increase in CH_4 conversion and CO selectivity is witnessed. At this point, methane conversion

is 97% with 94% selectivity to CO. At 900°C, CH_4 conversion reaches 99% with 98% selectivity to CO.

Results for Ni/CeO_2 are shown in Figure A.2. CO_2 formation occurs at around 300°C and O_2 and CH_4 conversion curves follow trends similar to those observed for Ni/SiO_2. The activation temperature for POM was 810°C with CH_4 conversion of 82% and 88% selectivity for CO. After activation, a sudden drop in the CH_4 conversion and CO formation, followed by another increase occurs. A second ramp-up of the same material reveals this drop behavior as well. At 900°C, the CH_4 conversion reaches 75% with 87% selectivity for CO. For this sample, the maximum CH_4 conversion occurs at the activation temperature rather than at 900°C.

The Ni content in the Ni/CeO_2 catalyst can be compared to that in the Ni doped ceria spray dried catalysts. 2.5 wt.% Ni is calculated based on the molecular weight of CeO_2. This value can be converted to at.% Ni based on the Ni/Ce atomic ratio. From this, the 2.5 wt.% Ni/CeO_2 catalyst is equivalent to 7 at.% Ni as compared to 10Ni and 20Ni.

Transmission electron microscopy data is also useful for Ni/CeO_2 for comparison with Ni doped materials. Figure A.3 shows a low magnification TEM image of Ni/CeO_2, and the corresponding HREM image. It is observed that small Ni particles are visible dispersed over the ceria support.

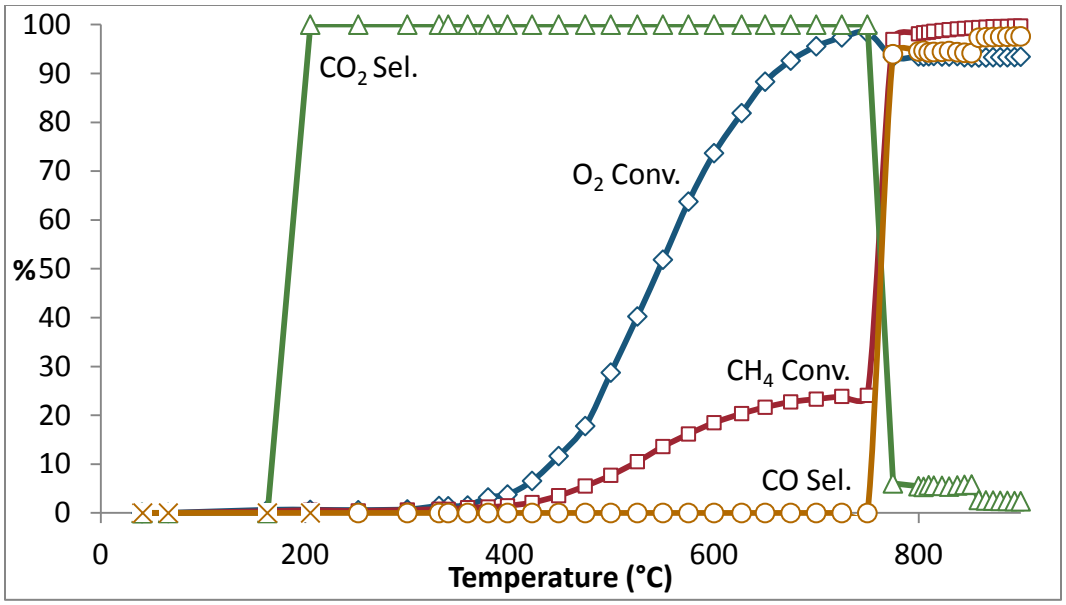

Figure A.1: Plot of percent conversion and selectivity vs. temperature during POM reaction for 2.5 wt.% Ni/SiO_2.

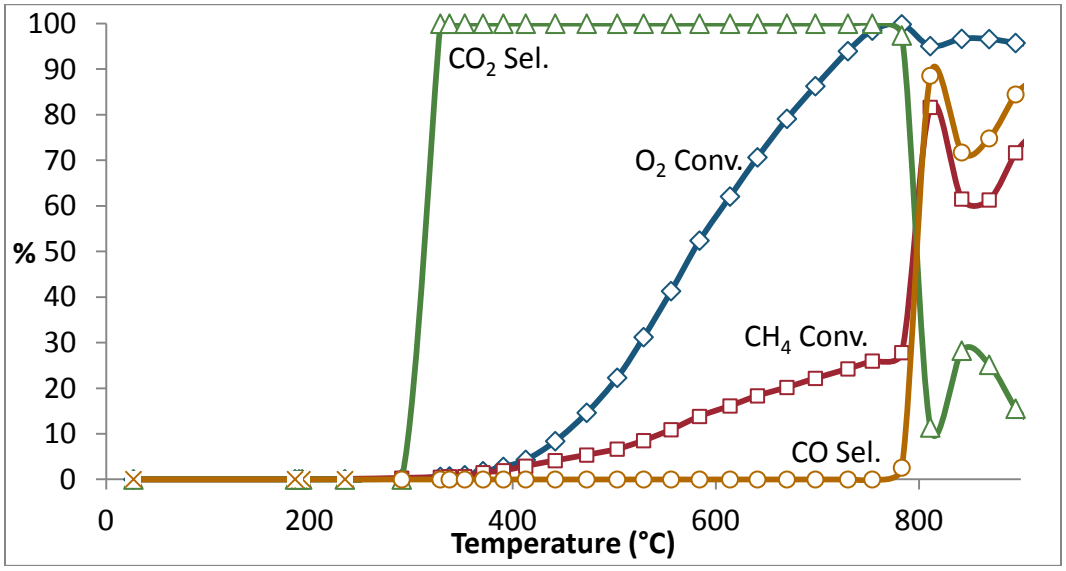

Figure A.2: Plot of percent conversion and selectivity vs. temperature during POM reaction for 2.5 wt.% (7 at.% Ni/Ce) Ni/CeO

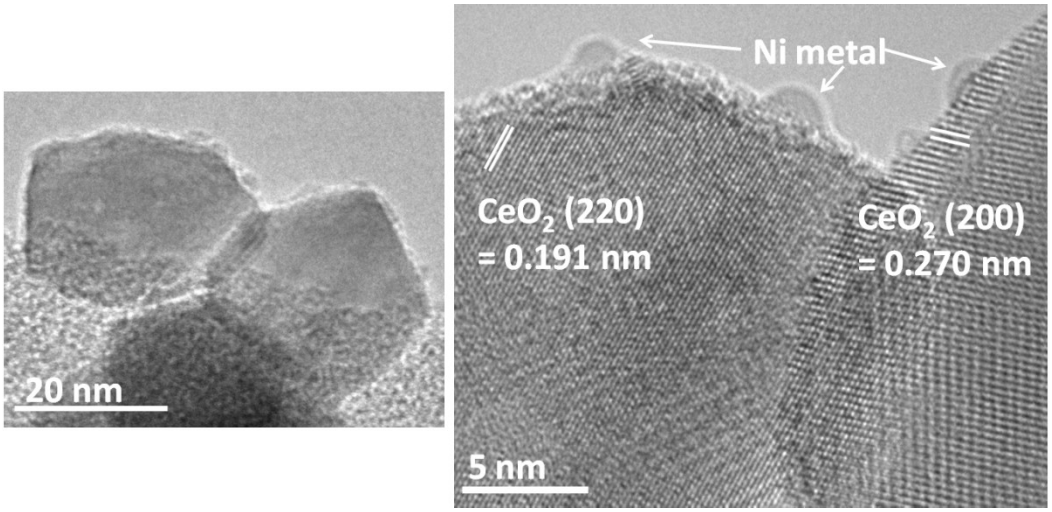

Figure A.3: Low magnification TEM micrograph of Ni/CeO_2 and corresponding HREM image revealing particles of CeO_2 as indicated by lattice fringes, and Ni particles on the surface of the support